NON-DESTRUCTIVE EVALUATION OF TWO-COMPONENT BACKFILL GROUTING BEHIND SEGMENTAL TUNNEL LININGS

by

Brett Kravitz

A thesis submitted to the Faculty and the Board of Trustees of the Colorado School of Mines in partial fulfillment of the requirements for the degree of Master of Science (Civil and Environmental Engineering).

Golden, Colorado

Date: _____

Signed: _____
Brett Kravitz

Signed: _____

Dr. Ahmedreza Hedayat
Thesis Advisor

Golden, Colorado

Date: _____

Signed: _____

Dr. Terri S. Hogue, PhD
Professor and Head
Department of Civil and Environmental Engineering

ABSTRACT

Non-destructive testing (NDT) techniques, such as Ground Penetrating Radar (GPR) and Impact Echo (IE), are being considered as potential methods for ensuring complete annular-grout backfill behind pre-cast segmental tunnel liners. Current methods for ensuring grout backfill involve drilled verification holes through waterproof tunnel liners. The Rondout Bypass Tunnel, in Newburgh, NY, where void formation behind the tunnel liner is possible due to high groundwater pressures, provided an example project to evaluate NDT capabilities. While the application of GPR for void detection in one component grouts behind tunnel liners has been well-documented, site specific calibration of the GPR equipment and study of the application to two-component grouts are necessary.

Laboratory testing of the two-component grout was conducted to obtain electromagnetic (EM) and elastic properties as they determine the efficacy of GPR and IE, respectively. Experiments were then conducted on actual tunnel segments to determine the most appropriate GPR antenna frequency that can penetrate through the steel-reinforced segments with the best resolution. Mock air and water voids were embedded within areas of complete grout behind the segment to demonstrate the GPR signatures. Steel reflectors buried within the grout provided indirect measurements of the electromagnetic (EM) properties of the two-component grout. All field results were compared against analytical evaluation and numerical models to validate void detection. Implementation of each technique on installed segments within the tunnel provided further evaluation using known backfill conditions at specific locations. The ability to conduct the testing during construction was shown as space is limited within the tunnel boring machine (TBM). The findings of this research allow for direct implementation of the GPR for detection of voids behind segmental tunnel liners with two-component grout backfill with the IE as a supplementary option for secondary evaluation.

TABLE OF CONTENTS

LIST OF FIGURES

LIST OF TABLES

ACKNOWLEDGMENTS

I would like to thank Reza Hedayat for selecting me to be the primary researcher for this work and for his support throughout the entire project. He was available anytime I needed help, including the grueling Colorado heat of the mock-liner testing and on the project site in New York. He also provided me with excellent guidance while allowing me the freedom to take the research where I saw fit. Additionally, thank you to Mike Mooney for his always insightful comments on the research findings.

Thank you to Kiewit for their support of this research. This work would not have been possible without the funding and resources they provided. In particular, thank you to Ian Danielson, Niels Kofoed, and everyone I had the privilege of working with while on the Rondout Project site.

Many questions would not have been answered without the many people willing to donate their time to help with my work. This includes Jurij Karlovsek and Thierry Bore from the University of Queensland who were always willing to provide insight they have learned from similar studies and John Bradford from the Colorado School of Mines who provided his geophysics expertise. Also, a big thanks to Manika Prasad and Brent Duncan for providing valuable resources to conduct experiments on the Colorado School of Mines campus.

Finally, thank you to my incredibly loving and supportive family members, including my parents Peter and Jennifer Kravitz, my sisters Dana and Rebecca Kravitz, and my grandparents Myrna and Steve Green and Eileen Kravitz. I would not be where I am today without them. My loving girlfriend Dani Plotkin, thank you. And of course, thank you to all my friends afar and my new friends and colleagues I've made while attending the Colorado School of Mines.

CHAPTER 1

INTRODUCTION

1.1 Problem Statement and Research Motivation

The Rondout Bypass Tunnel project is an effort to replace a 4 km (2.5 mile) portion of the existing 137 km (85 mile) long Delaware Aqueduct between Newburgh, NY, and Wappinger, NY. A 3-dimensional rendering of the project specifics is displayed in Figure 1.1. Unrepairable structural damage to the original deep-rock tunnel has induced constant leaks of up to 130 million liters (35 million gallons) of fresh water a day (New York City Department of Environmental Protection, 2017). This aqueduct transports approximately 1.9 billion liters (500 million gallons) of fresh water a day, or half of New York City's fresh water supply (de Blasio and Sapienza, 2016).

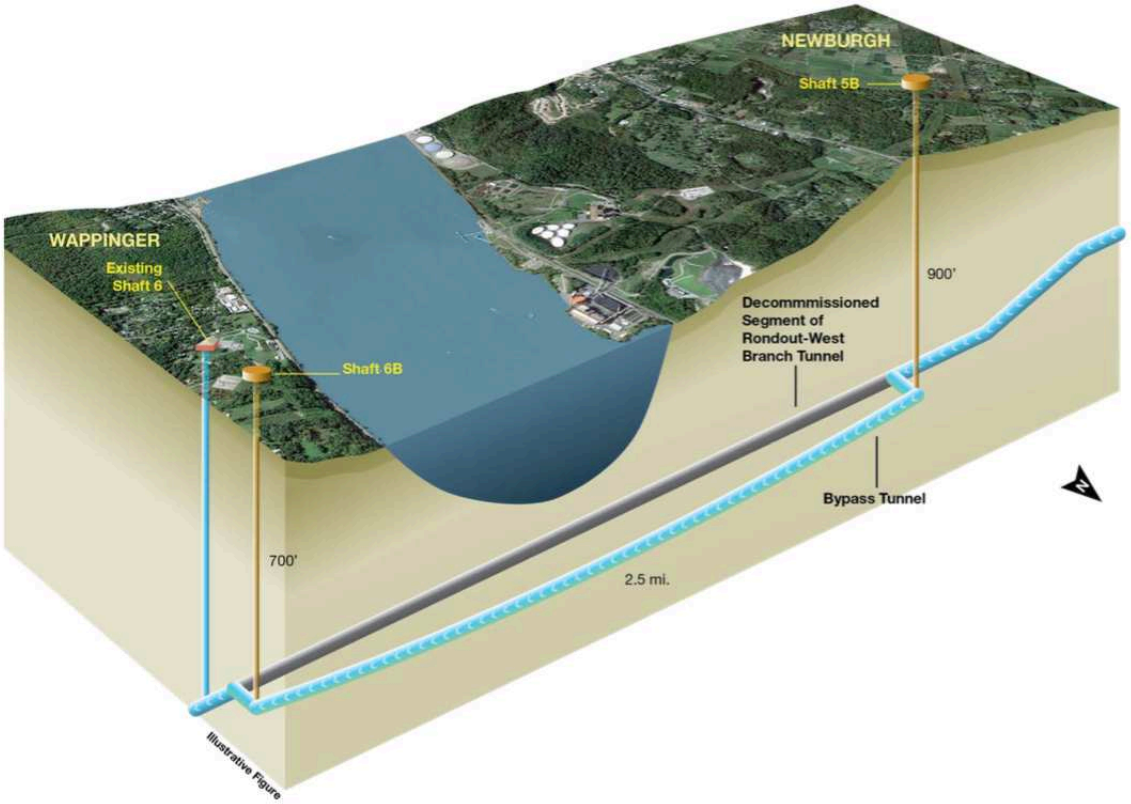

Figure 1.1 Rondout project overview (New York City Department of Environmental Protection, 2017)

Construction consists of two blasted shafts of 275 m (900 ft) and 200 m (650 ft) depths through shale on each side of the Hudson River with up to 267 m (875 ft) of water head possible along the alignment. A shielded-open face tunnel boring machine (TBM) was launched through the western shaft and advanced easterly underneath the Hudson River through shale in reaches 1 and 4 and fractured limestone/dolomite units in reaches 2 and 3. The existing Delaware Aqueduct, located adjacent to the Rondout Bypass Tunnel alignment, has the potential to induce water pressures greater than hydrostatic pressures from the Hudson River above. Geotechnical investigation reports produced for this project estimate water inflows as high as 4.9 m^3/min (1295 gpm).

The existence of poor rock mass with inter-connected fracture networks can potentially create conditions leading to washout of the injected annulus grout before it sets. This occurrence would lead to a large water filled void in place of the grout. A secondary effect of this type of void is for washout to continue as more grout is placed, leading to an insufficient grout volume and the potential for large voids to form at the crown. Another potential for void formation in the annulus space is for large rock-cut over break causing the grout to infill fractures within the rockmass and resulting in an insufficient grout volume. Figure 1.2 provides illustration of the tunnel geometry and void formation possibilities.

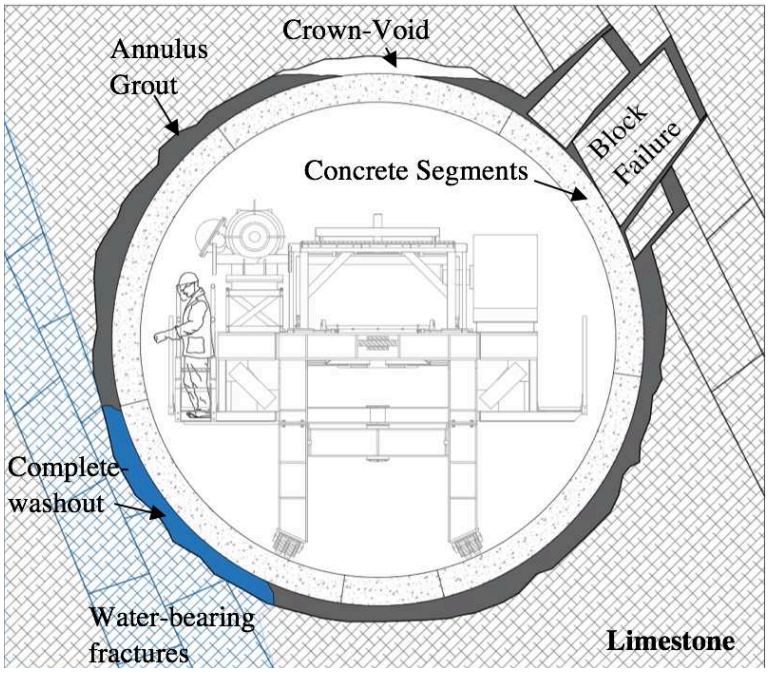

Figure 1.2 Depiction of potential grout washout conditions. TBM trailing gear shown inside the tunnel.

Other void possibilities, not demonstrated in Figure 1.2 may exist, such as the presence of seams within the grout or thin layers of grout at the segmental liner extrados or rock boundary. The potential for annulus grout washout leading to an insufficient grout volume creates the need for quality assurance on the injected annulus grout. Existing methods for quality assurance typically involve destructive methods, such as drilled holes or cores through the tunnel liner. This research work involves identification of areas with grout washout during construction by use of non-destructive testing (NDT) methods. Two NDT methods, ground penetrating radar (GPR) and impact echo (IE), were experimented with and implemented in the field to determine their efficacy as a potential replacement for destructive quality assurance methods.

1.2 Research Objective and Approach

The objectives of this research project were characterizing the capability and reliability of GPR and IE in detecting water or air-filled voids formed within the annulus space, providing a recommendation to the contractor on the most appropriate technique to employ in the field, and providing data analysis and an implementation technique that can be used for grout QA for the remainder of this tunnel construction project. The recommendations and results from this research can be extrapolated for use on future tunnel projects with similar conditions which consist of a segmental tunnel liner with two-component grout backfill. In order to achieve the stated research objectives, several critical steps were taken. First, a comprehensive literature review of previous projects using NDT methods was performed. The underlying physics of each method were also studied in detail. Next, laboratory testing was conducted on the annulus grout to estimate what void detection tools are most likely to work and what the expected results should be. After that, full-scale experiments were set up to calibrate and choose the most appropriate GPR antenna for void identification. Finally, the NDT methods selected were implemented in the tunnel field setting and the results and implementation methods were communicated to the contractor's field engineers for future data collection.

1.3 Thesis Structure and Organization

This research provides a detailed analysis of the GPR and IE methods to determine their feasibility in detecting complete grouting and potential voids. Chapter 2 provides background on generalized tunnel construction methodology and the significance of two-component annulus

grout. The underlying physics of GPR and IE are presented to enable complete understanding of how these methods work. Previous tunnel projects provide case studies using these methods. Chapter 3 presents specific details on the TBM and grout used in the Rondout project, as they are relevant to the research objectives. Chapter 4 details laboratory investigations into the relevant grout properties to assist with the geophysical assessment. The methods, materials, results, and discussions are provided for each of the different property tests. Chapter 5 discusses two mock-liner experiments which helped define the GPR assessment method and prove its capabilities before any field data were gathered. The experiments were vital in providing physical proof for the types of GPR radargrams expected in the different tunnel environments. Finally, Chapter 6 presents the field data gathered from the GPR and IE field investigation on installed segments in the tunnel. The full description of the methods, capabilities, and limitations is provided to allow for comparison of physical quality assurance (QA) data gathered by means of destructive methods. Conclusions and recommendations for future research related to this topic are presented in Chapter 7.

CHAPTER 2
BACKGROUND AND PREVIOUS STUDIES

This chapter provides technical background on the significance of annulus grout for generalized tunnel mechanics, GPR fundamental physics and applicability, and impact echo fundamental physics and applicability as they each relate to the findings of this research. Published works described herein demonstrate successful implementation of these NDT methods in similar applications.

2.1 Annulus Grout

Each tunnel project is built in unique ground conditions with different construction methods and therefore the annulus grout must be best-suited to the specifications set by the owner and contractor. A wide variety of grout types and injection methods exist to select from for any given tunnel project. This section details the mechanical effects of the annulus grout on a tunnel, typical grout washout prevention methods commonly used in tunnel projects, and two-component grout design.

2.1.1 Annulus Grout Significance in Tunnel Applications

Grout injected into the annulus gap between the tunnel segmental liner and the surrounding ground has several potential implications for the tunnel-ground interaction (Shirlaw et al., 2004):

- Provides uniform and immediate contact between the tunnel liner and the ground in order to prevent unequal loading to the liner. Lack of grouting in regions of the tunnel, or large voids can result in stress concentrations at particular locations on the liner which can ultimately cause cracking.
- Partially controls ground surface settlement, particularly in soft ground tunneling. Ground relaxation will inevitably occur after the advancement of the TBM shield support. This ground relaxation is counteracted by the stiffness of the tunnel lining system (i.e., the combination of annulus grout and the liner).

- Provides support for the tunnel rings while the TBM thrusts forward. When the TBM is directionally steering, the annulus grout is required to resist moments induced in the liner from unequally distributed loading on the previously installed ring.
- Supports loads from the TBM trailing gear and tunnel weight.
- Acts as a secondary means of water-tightness to the tunnel liner where the tunnel liner gaskets may fail or allow some seepage.

In addition to these design elements, a low density grout compared to the cross-sectional density of the tunnel, which is mainly comprised of air, will create buoyant forces on the tunnel liner before the grout has gained adequate shear strength (Bezuijen et al., 2005). The tunnel is considered a fixed beam supported between the hardened grout and the TBM tail shield (Bezuijen et al., 2005). The length of tunnel embedded within unset grout is considered an unsupported length. Therefore, the unsupported length must be minimized to prevent undesired displacement of the tunnel liner. TBM thrust forces on the liner, as well as buoyant forces of the unset grout can cause displacements on the unsupported liner. The grout stiffness also impacts the stiffness of the tunnel liner which can be considered a composite material with the annulus material and main liner. A stiffer grout will allow for less ground deformation which transfers more load onto the tunnel liner (Sharghi et al., 2017). All of these design elements of the grout result in the desire for a fast-setting grout, with a low density, that quickly gains high stiffness and shear strength.

2.1.2 Annulus Grout Washout Prevention and Assurance

Various techniques exist for the prevention of annulus grout washout in high ground-water flow environments. The first design aspect to consider is the type of grout used. In hard rock environments where ground support is of less significance, an inert mix can be used in the annulus gap (Peila et al., 2011). This can be composed of sand, pea gravel, and other filler, without cement. Use of aggregate provides enough support to transfer ground loads onto the tunnel liner and prevent in-situ rock from falling onto the liner. However, inert mixes are susceptible to a type of slope failure when the TBM advances forward and annulus material redistributes within the newly un-filled annulus space, resulting in a void at the crown (Henzinger et al., 2016). Cement may also be used in conjunction with pea gravel to induce additional strength and prevent slope failure (Henzinger et al., 2016). A single grout mixture injected into

the annulus space can be referred to as a single component grout. Anti-washout admixtures have been proposed to be added to single-component grout mixes with engineered rheology in order to help with washout prevention (Khayat, 1998; Bessaies-Bey et al., 2015; Cui et al., 2017). However, these admixtures do not necessarily help with immediate material strength. Two-component grout, which utilizes a retarded grout mixture injected concurrently with an accelerant, has more recently been implemented as an option of creating immediate strength in the annulus while still being a pumpable mixture (Sharghi et al., 2017).

In addition to the grout type, the grout injection method must also be considered. Past projects have injected grout through portals in the tunnel lining after the shield has passed (Xie et al., 2007; Aggelis et al., 2008). This method creates an unsupported length of tunnel before grouting takes place. By leaving time before grouting, water pressure may accumulate in the annulus space which can create the undesired washout effect when injecting grout. In most modern TBM's, grouting is now conducted out of portals at the back of the tail shield to provide continuous ground support as well as prevent water from accumulating in the annulus space (Bezuijen et al., 2005; Peila et al., 2011; Henzinger et al., 2016).

Methods for quality assurance of the annulus grout include monitoring the total volume of grout injected, direct testing through the liner by destructive or non-destructive methods, and evidence of significant water pressures from leaking gaskets or wet-patches on the segmental liner (Brantberger et al., 2000; Hee, 2012; Karlovšek et al., 2012). In a pressurized TBM, typically used in soft ground tunneling, the backfill grouting pressure may also be monitored to provide quality assurance (Brantberger et al., 2000; Hee, 2012; Karlovšek et al., 2012). If evidence exists indicating potential voids by primary monitoring methods, secondary QA methods, such as coring or drilled holes through the segmental liner may then be conducted to check for void spaces. Secondary grouting is typically performed to fill identified void spaces and can be performed through portals of the installed segments. If in-situ water conditions allow, an adjacent segment may be left with its center portal open to determine when grout begins seeping out, indicating full connectivity of the grout injection. Additional testing, by destructive or non-destructive methods, is then required after the secondary grouting is performed to prove the voids have been filled.

A new innovative approach for reducing grout washout in the annulus space is the bull flex ring installation (Henzinger et al., 2016). A common phenomenon experienced in tunneling

is perpetual grout washout along the tunnel alignment when a single high-water flow feature is encountered. The high-water flow essentially chases the TBM advancement. In order to prevent this situation, a special liner can be installed when washout is first detected that contains an inflatable bag on the liner extrados. After the bull flex ring is installed, a cementitious mix is pumped into the bags to secure the grout material in the annulus space. This bag is designed to be larger than the annulus space gap to ensure grout backfill reaches the in-situ ground and prevents water from running longitudinally along the tunnel alignment. This novel approach is still being experimented with but maintains the requirement of first detecting washout. Photos from a bull flex ring test are displayed in Figure 2.1 demonstrating the inflatable grout bag that fills in the annulus space circumferentially around the tunnel.

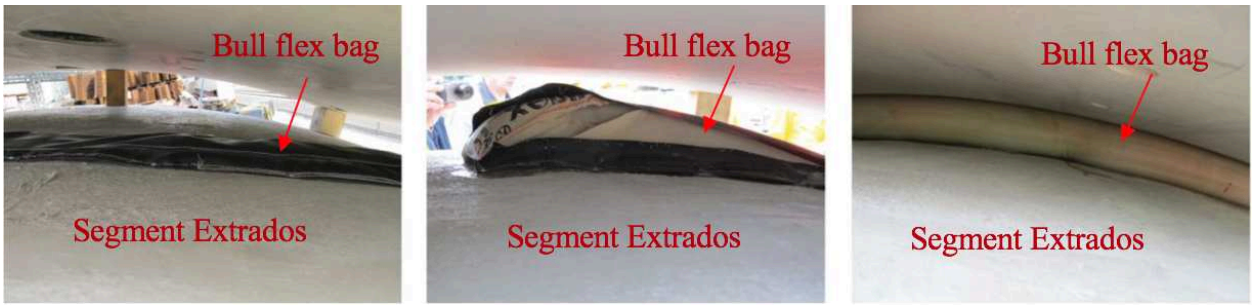

Figure 2.1 Bull flex ring experiment on two-stacked tunnel segments (Modified from Henzinger et al., 2016) (left) before bag inflation; (center) during bag inflation; (right) after bag inflation.

2.1.3 Two-Component Grout Design

The grout used in TBM's must meet specific requirements for constructability and structural design. Fluid ingredients are desired to be injectable into the annulus space and to gain strength instantaneously to provide immediate support for the liner. Two-components grouts achieve these requirements by being a flowable mix that can gel within 20 seconds and rapidly gain strength with time (Yang and Song, 2009; Pelizza et al., 2010; Azadi et al., 2017; Sharghi et al., 2017). If the material gels too quickly, it can clog the mixing pipe chamber. Whereas if it takes too long to gel, the risks of washout and surficial ground settlement, and liner design implications increase. Typical early strength requirements are between 0.1 to 0.3 MPa for 1 hour (Bernat and Cambou, 1998; Hashimoto et al., 2004; Pellegrini and Perruzza, 2009; Fowler et al., 2012). The final strength is typically regarded as less consequential than the short term strength,

and final design strength varies between 1 to 3 MPa in literature (Bernat and Cambou, 1998; Hashimoto et al., 2004; Pellegrini and Perruzza, 2009; Fowler et al., 2012).

The construction requirements of the grout are for each component to be pumpable for the full tunnel and shaft length, and stable for the duration of grout transport from the colloidal mixer until grout injection plus additional time for intermittent TBM maintenance periods. It is desired for the grout to be mixed above ground, sometimes on the order of miles from the final injection point, and pumped through pipes into the TBM. Therefore, grout viscosity is of significant importance for the design of the system pumps and flow rates. The grout stability is dependent upon its bleed, a measure of the percentage of water separation from the cement solution, which is often designed to be less than 5%. This allows the mixed grout to remain in pipes and be immediately available even after 72 hours or more of unexpected delays.

Typically, the first component of a two component grout consists of a cementitious mix, containing water, cement, bentonite, retarder, and sometimes fly ash (Sharghi et al., 2017). This is commonly referred to as the component A. Water to cement ratios (w/c) in this component are typically between two and three in order to create a low-viscous fluid. In order to prevent significant bleed, which would occur from an over-saturated cement solution, bentonite is mixed with the water first and then cement is added. The bentonite's high swelling capabilities allow it to adsorb water and prevent water separation from the cement mixture. Fly ash is a common pozzolan that can be used as a supplementary cementitious material and contribute to the final strength gain. Retarder is introduced to keep the component A fluid until combined with the accelerant. The component B is an accelerant, typically sodium silicate, calcium aluminate, or aluminum sulfate, that must also be pumpable and have fast set times with the stabilized component A.

2.2 Ground Penetrating Radar Background

GPR operates by emitting an electromagnetic (EM) wave pulse and measuring the return time and strength of the wave reflections off material boundaries (Daniels, 2004; Annan, 2005; Takahashi et al., 2012). When an EM wave reaches a material boundary with an impedance contrast, a portion of the wave energy will be reflected, and the remainder of the wave energy will be transmitted into the next medium. An example is a wave traveling through concrete and water, where part of the wave reflects off the water boundary and part continues on through the

water until reaching the next interface. The data collected by the transmitted EM wave pulse can indicate the depth and type of boundaries and is often analyzed in the form of a radargram which displays a 2-dimensional cross section of the arrival times and intensity for reflected wave fronts. EM wave propagation physics, necessary for the understanding and interpretation of results generated from GPR, are detailed in this section.

2.2.1 EM Wave Propagation

The principles for understanding GPR are founded in electro-magnetic wave theory. EM waves propagate according to a set of four mathematical equations known as the Maxwell equations (Annan, 2005):

$$\nabla \times \mathbf{e} = -\frac{\partial \mathbf{b}}{\partial t} \tag{2.1}$$

$$\nabla \times \mathbf{h} = \mathbf{j} + \frac{\partial \mathbf{d}}{\partial t} \tag{2.2}$$

$$\nabla \cdot \mathbf{d} = \rho \tag{2.3}$$

$$\nabla \cdot \mathbf{b} = 0 \tag{2.4}$$

where **e** is the electric field strength vector (V/m); **b** is the magnetic flux density vector (T); **d** is the electric displacement vector (C/m^2); **h** is the magnetic field intensity (A/m); ρ is the electric charge density (C/m^2); **j** is the electric current density vector (A/m^2); and t is time in seconds. These equations describe orthogonally oriented time-varying electric and magnetic fields. Constitutive relationships between the parameters defined above and material properties describe how EM waves are affected by the medium in which they travel through. The three relevant material properties are electrical conductivity (σ_T), dielectric permittivity (ε_T), and magnetic permeability (μ). The relative magnetic permeability is commonly assumed to be 1 for materials known not to have significant magnetic properties (Annan, 2005; Knight and Endres, 2005) and therefore not considered to affect the EM wave propagation in this study.

2.2.2 Complex Dielectric Permittivity

EM wave propagation through a medium is dictated by two sets of complex equations containing four material properties (Knight and Endres, 2005):

$$\varepsilon_T(\omega) = \varepsilon'_T(\omega) - i\varepsilon''_T(\omega) \tag{2.5}$$

and

$$\sigma_T(\omega) = \sigma'_T(\omega) - i\sigma''_T(\omega) \tag{2.6}$$

where $\varepsilon_T(\omega)$ and $\sigma_T(\omega)$ are the total permittivity and total conductivity, respectively. $\varepsilon'_T(\omega)$ is the dielectric polarization term, $\varepsilon''_T(\omega)$ represents energy loss due to polarization lag, $\sigma'_T(\omega)$ refers to ohmic conduction, and $\sigma''_T(\omega)$ is related to faradaic diffusion, all as a function of frequency (Knight and Endres, 2005). The ratio of energy lost to energy stored is referred to as the loss tangent. This ratio is used to predict the attenuation coefficient for an EM wave in a given material, and is written as:

$$tan\delta = \frac{\sigma' + \omega\varepsilon''}{\omega\varepsilon' + \sigma''} \tag{2.7}$$

where $tan\delta$ is the ratio of energy lost to energy stored. Materials with large loss tangents are commonly referred to as lossy materials, such as salt water with a loss tangent approximately equal to 0.75. Stored energy from dielectric polarization is due to molecular, ionic, or atomic polarization when an electric field temporarily rotates and aligns either the molecules, ions, or atoms in a material, depending on frequency and material susceptibility (Powers, 1997). Energy losses typically come from either electrical conduction due to electrical charge carriers present in a material or polarization lag from the EM frequency (Powers, 1997). Conducting materials dissipate the propagating EM wave into electricity described by diffusion. Polarization lag refers to the inability for part of an EM wave to polarize the material due to an out-of-phase polarization relationship. Due to the fact that only two terms are determined from laboratory measurements (Chen et al. 2014), these four properties are typically described by two effective parameters (Knight and Endres, 2005):

$$\varepsilon_{eff} = \varepsilon' + \frac{\sigma''}{\omega} \tag{2.8}$$

and

$$\sigma_{eff} = \sigma' + \omega\varepsilon'' \tag{2.9}$$

where effective permittivity (ε_{eff}) and effective conductivity (σ_{eff}) describe the total energy stored and lost in a material, respectively. Effective permittivity in this report is considered to be the relative effective permittivity, where the values denoted are the real-valued effective permittivity divided by the permittivity of free space (ε_o = 8.85418782 X 10^{-12} F/m). Using these effective parameters reduces the loss tangent to:

$$tan\delta = \frac{\sigma_{eff}}{\omega\varepsilon_{eff}} \tag{2.10}$$

Further simplifications are commonly made depending on the frequency range being analyzed. For frequencies above 100 kHz, σ''/ω may be assumed to be 0, and σ' is assumed to be equivalent to the DC conductivity, σ_{DC}. Hence, effective permittivity is approximated as the real component of the complex permittivity function and effective conductivity is the sum of the DC conductivity and the imaginary part of the complex permittivity function, as follows:

$$\varepsilon_{eff} = \varepsilon' \tag{2.11}$$

and

$$\sigma_{eff} = \sigma_{DC} + \omega\varepsilon'' \tag{2.12}$$

These forms of the simplified effective permittivity and conductivity are used herein. As described by equation 2.12, the DC conductivity represents the minimum possible conductivity of a material where energy loss to polarization is insignificant.

2.2.3 Electrical Conductivity

Electrical conductivity describes a materials ability to conduct electrical current. Current is typically carried by either mobile ions present in a solution, or through valence electrons typical in a metal (Tang et al., 2017). Due to the presence of water in porous materials, such as

soil, rock, or concrete, electrical conductivity is highly dependent upon the internal pore structure and water content. As described in section 2.2.2 , electrical conductivity provides the basis for interpretation of the attenuation of an EM signal in a material. For this reason, an in-depth look into electrical conductivity of grouts and other cementitious materials is described to relate to the GPR attenuation observed in the grout.

2.2.3.1 Electrical Conductivity of Cementitious Materials

Electrical conductivity is commonly used as a measure for set time and moisture content for cementitious materials (Tumidajski, 1996; Levita et al., 2000; Han et al., 2007; Li et al., 2007; Rajabipour and Weiss, 2007; Susanto et al., 2013; Weiss et al., 2013; Layssi et al., 2015; Harbec et al., 2016; Tang et al., 2017; Yousuf et al., 2017). In porous materials, electrical conductivity is a function of the pore solution conductivity and the surface conductivity. Surface conductivity stems from the intrinsic charges on the particle surfaces which are coated by an electrical double layer (Revil et al., 2017). Pore solution is responsible for the bulk of electrical conductivity in a porous media due to ion transport (Li et al., 2007). Therefore, available pore space is significant to the total measured conductivity. As a cement paste sets, the pore space is reduced and the measured conductivity decreases. Various bounding models have been proposed to estimate electrical conductivity in a porous media based on the geometrical factors and individual component conductivities that comprise the medium, summarized by Cai et al. (2017). Guéguen & Palciauskas (1994), proposed bounding models based on parallel or perpendicular structural forms that can have many conducting phases. The parallel model being the same as an arithmetic mean weighted by the volume fractions, and the perpendicular model expressed by a weighted harmonic mean. Hashin & Shtrikman (1962), produced bounding models derived from effective medium theory and more restrictive than the parallel and perpendicular models. Other conductivity models incorporate more complex geometrical considerations, such as spheres surrounded by a pore fluid (Waff, 1974). These models may be applied to cementitious materials with the consideration that the cement set time varies based on the rate of hydration. Archie's law has been applied to concrete with 100% saturation to determine the bulk measured conductivity of a concrete material (Li et al., 2007).

Yousuf et al. (2017) demonstrated through experimentation that cement with super plasticizer (sp) greatly effects the final micro-structure and results in a higher electrical

conductivity due to more inter-connected pore space. The superplasticizer retards the cement hydration process, which lowers the electrical conductivity rate at early time, and the final product contains less ions and less hydration products. Figure 2.2 displays the results from this study along with interpretation of the micro structure for two types of ordinary cement classes (32.5 and 42.5). Different dosages of sp were used, denoted in Figure 2.2 by the sp percentage.

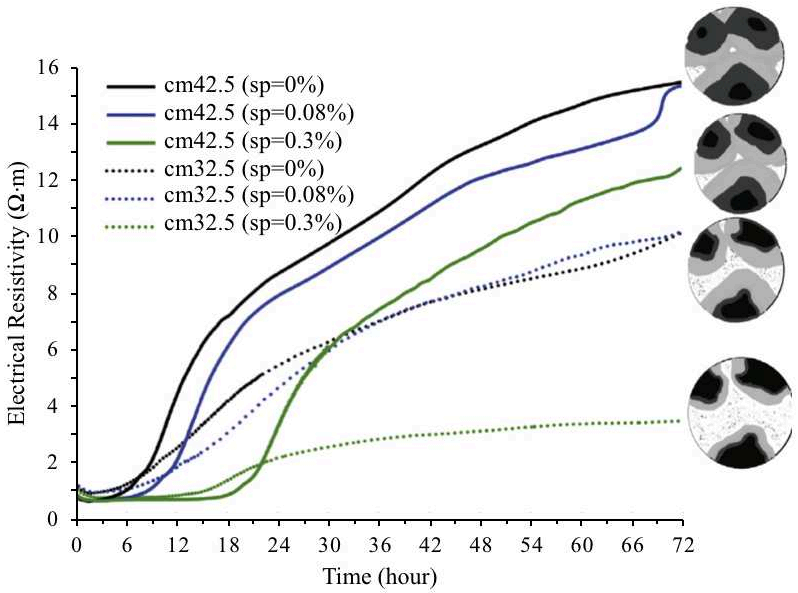

Figure 2.2 Results of electrical resistivity (inverse of conductivity) measurements conducted on cement mixes with varying amount of super plasticizer (modified from Yousuf et al. 2017)

The conductivity of the pore fluid itself is also changing as cement hydrates, and this phenomenon has been observed in several studies (Rajabipour and Weiss, 2007; Xiao and Li, 2008; Harbec et al., 2016; Yousuf et al., 2017). The change in pore fluid conductivity has been associated with the dissolution of Ca^{2+} ions in the pore solution when cement is put in contact with water (Harbec et al., 2016). Therefore, even though the relative connectivity of the pore space is decreasing with cement set time, the increasing concentrations of ions increases the total conductivity of the pore solution. Values of conductivity for early set time of cementitious materials tend to be relatively high (0.1 – 3 S/m) compared to other geomaterials, such as silt, shales, and limestone, due to the composition of cement which precipitates ionic species such as Na^+, K^+, Ca^{2+} and OH^- into the pore fluid (Rajabipour and Weiss, 2007).

2.2.3.2 Electrical Conductivity Lab Measurements

Various methods for laboratory measurements exist to determine a material's electrical conductivity. Most methods can be generally categorized into either Direct Current (DC) methods (Han et al., 2007; Layssi et al., 2015; Madhavi and Annamalai, 2016; Sharma and Kothiyal, 2016; Tang et al., 2017), or Alternating Current (AC) spectroscopy (Levita et al., 2000; Xiao and Li, 2008; Topcu et al., 2012; Tang et al., 2017). DC methods involve application of a direct current through the material and measuring the voltage drop through the use of Ohm's law ($V = I \times R$). This can incorporate 2 or 4 electrodes in various arrays. The two-electrode method utilizes the same electrodes to induce the current and measure the voltage differential. This method, however, has been shown to be affected by electrolysis at the connection between the electrodes and the cementitious materials (Han et al., 2007). The four-electrode method uses two outer-electrodes to apply DC current and measures the voltage differential in between the outer electrodes. This was shown to effectively eliminate the electrolysis effects of the 2-electrode method (Han et al., 2007). A Wenner array probe is a special type of 4-electrode DC measurement that can both apply current and measure voltage at the surface of a specimen (Instruments, 2010; Gucunski et al., 2013). All these methods provide relatively simple and inexpensive ways to measure DC conductivity.

AC-spectroscopy methods differ by use of an applied AC current which is capable of measuring the frequency dependent component of conductivity. These methods therefore measure the effective conductivity of a material and generally cannot distinguish the DC conductivity component. Tools such as a Vector Network Analyzer (Venkatesh and Raghavan, 2005; Kaatze, 2010; Tereshchenko et al., 2011; Josh and Clennell, 2015) can be used to determine the complex conductivity function, which includes measurements of permittivity.

2.2.4 EM Wave Propagation

Effective permittivity and conductivity determine EM wave velocity, impedance, and attenuation. All of these properties are essential to understanding the results from GPR scans since they effect the return time of a reflected wave off an interface, the amount of energy reflected from that interface, and the amount of energy lost as the wave travels through the material. The attenuation constant provides a basis for understanding the depth a GPR wave can propagate for a given material at a specific frequency (Daniels, 2004):

$$\alpha = \omega \sqrt{\frac{\mu \cdot \varepsilon_{eff} \cdot \varepsilon_o}{2}} \cdot (\sqrt{1 + tan\delta^2} - 1)^{\frac{1}{2}} \quad (2.13)$$

where α is expressed in dB·m^{-1}. Taking the inverse of the attenuation constant provides a depth at which ~37% of the energy is attenuated due to material losses, referred to as skin depth (Takahashi et al., 2012; Oldenburg et al., 2017):

$$\delta = \frac{1}{\alpha} \quad (2.14)$$

Skin depth is a useful indication of the depth GPR will image in a lossy material. This equation reveals that materials with high loss tangents will have greater attenuation and smaller skin depth. This is particularly true for conductive materials such as salt water and the two-component grout with high conductivity values. Skin depth of a typical concrete will be on the order of meters since the conductivity is relatively low. Dielectric property values of common geomaterials are presented in Table 2.1 (Soutsos et al., 2001; Annan, 2005).

Table 2.1 Dielectric properties of common geomaterials

Material	ε_{eff}	σ_T **(mS/m)**	v **(m/ns)**	α **(dB/m)**
Air	1	0	0.30	0
Distilled Water	80	0.01	0.033	2e-3
Fresh Water	80	0.5	0.033	0.1
Sea Water	80	3000	0.01	103
Dry Sand	3-5	0.01	0.15	0.01
Saturated Sand	20-30	1-10	0.06	0.03-0.3
Limestone	4-8	0.5-2	0.12	0.4-1
Shales	5-15	1-100	0.09	1-100
Silts	5-30	1-100	0.07	1-100
Clays	5-40	2-1000	0.06	1-300
Granite	4-6	0.01-1	0.13	0.01-1
Concrete	5-12	0.1 - 100	0.10	0.01-6

Figure 2.3 demonstrates the relative importance of effective conductivity compared to permittivity for evaluating a material's skin depth. At effective conductivity values greater than 1000 mS/m, GPR skin depth is less than 2 inches, rendering it an ineffective tool if trying to collect data beyond that depth. At an effective conductivity less than approximately 200 mS/m, the skin depth drastically improves and will eventually become a secondary factor of total attenuation to scattering, caused by inhomogeneities within the material. Scattering in earthen materials is the result of small reflections off inhomogeneous material boundaries such as soil grains or rock fractures. Concrete will not experience the same degree of scattering as the soil since the grain size in concrete is relatively small compared to the wavelength for the EM wave applied. Therefore, attenuation in dried single-component grout or concrete is typically not of great concern when using GPR to image on a centimeter scale.

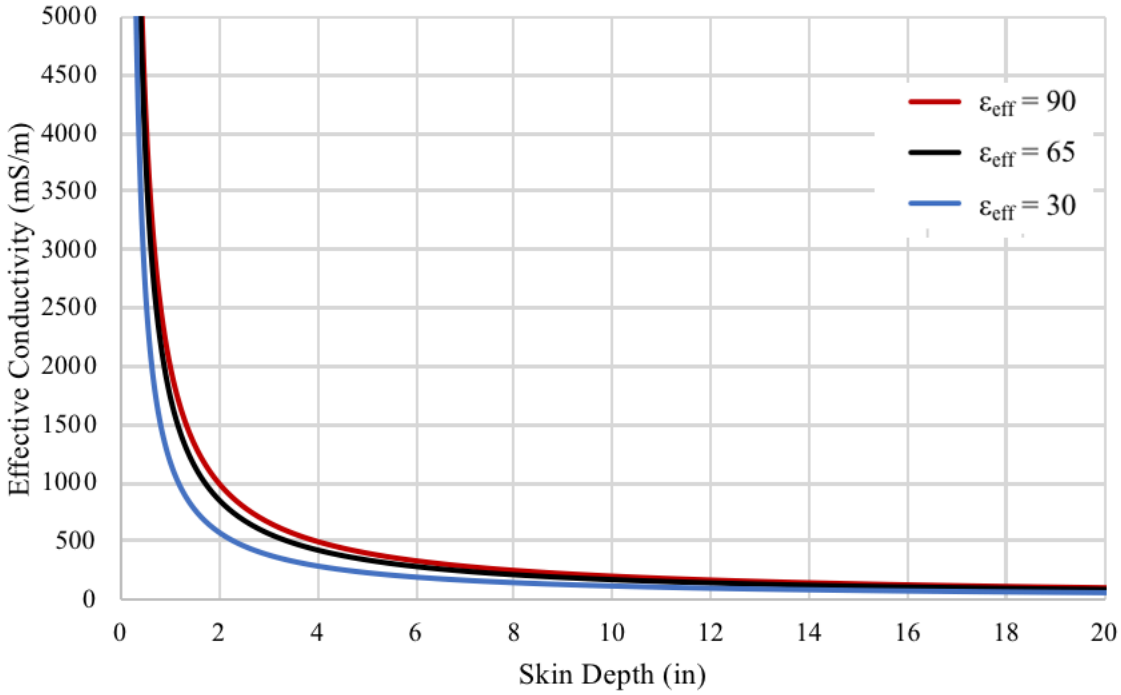

Figure 2.3 Skin depth as a function of material's conductivity and permittivity

EM wave velocity is determined from the wave phase constant (Daniels, 2004):

$$\beta = \omega \sqrt{\frac{\mu \cdot \varepsilon_{eff} \cdot \varepsilon_o}{2}} \cdot \left(\sqrt{1 + tan\delta^2} + 1\right)^{\frac{1}{2}} \tag{2.15}$$

and

$$v = \frac{\omega}{\beta} \tag{2.16}$$

where velocity (v) is typically expressed in m/ns. Estimating the EM wave velocity for a given material enables prediction for the timing of received waves off boundary reflections. The amount of energy reflected off a material boundary is determined by the contrast in material impedance (Daniels, 2004):

$$\eta = \sqrt{\frac{-j\omega\mu}{\sigma_{eff} - j\omega\varepsilon_{eff}\varepsilon_o}} \tag{2.17}$$

where η is the complex intrinsic impedance of the medium measured in Ohms. A material with a large impedance implies a small permittivity. Therefore, air, with a relative permittivity of 1, will have a relatively large impedance. Alternatively, a material with very large permittivity, such as water, will have a smaller impedance. Conducting materials, such as metals, will have an impedance approaching 0, indicating EM waves will be fully reflected. Reflection coefficients are then determined by (Daniels, 2004):

$$R = \frac{\eta_2 - \eta_1}{\eta_2 + \eta_1} \tag{2.18}$$

where η_1 is the impedance of the material in which the wave is propagating through, and η_2 is the impedance of the material at the boundary which the EM wave reaches. The reflection coefficient, R, can be negative or positive. The magnitude of the reflection coefficient indicates how much of the EM wave energy reflects off the boundary, where 0 indicates no impedance contrast, and 1 implies full reflection of the wave. Larger reflection coefficients indicate more energy is reflected off the interface and less energy transmitted. A positive reflection coefficient indicates the wave has reflected off a material with a greater impedance, and the returned signal will maintain its incident phase. An example is a wave traveling through concrete and reflecting off an air boundary. Alternatively, a negative reflection coefficient indicates the wave has reflected off a material with a lower impedance, and the returned signal will reverse its incident phase. An example of this is an EM wave traveling through concrete and reflecting off water.

2.2.5 GPR Resolution

GPR detection resolution is dependent upon the received wave frequency. Resolution in a radargram can be generally categorized between radial (vertical) and lateral (horizontal) resolution. As described previously, GPR emits an EM pulse which typically takes on the Ricker wavelet form, shown in Figure 2.4. A Ricker wavelet is a zero-phase wavelet with its amplitude defined by (Sheriff, 2002):

$$f(t) = (1 - 2\pi^2 \cdot f_M^2 \cdot t^2)e^{-\pi^2 \cdot f_M^2 \cdot t^2} \tag{2.19}$$

where f_M is the central frequency and t is time. The pulse width of this wavelet, T_D is:

$$T_D = \frac{\sqrt{6}}{\pi \cdot f_M} \tag{2.20}$$

A Ricker wavelet contains a range of frequencies in its signal, which can be described by a peak central frequency using a Fourier transformation. GPR antenna are defined by their peak central frequency and not the bandwidth of the pulse. However, resolution in a radargram is dependent upon the actual frequency bandwidth.

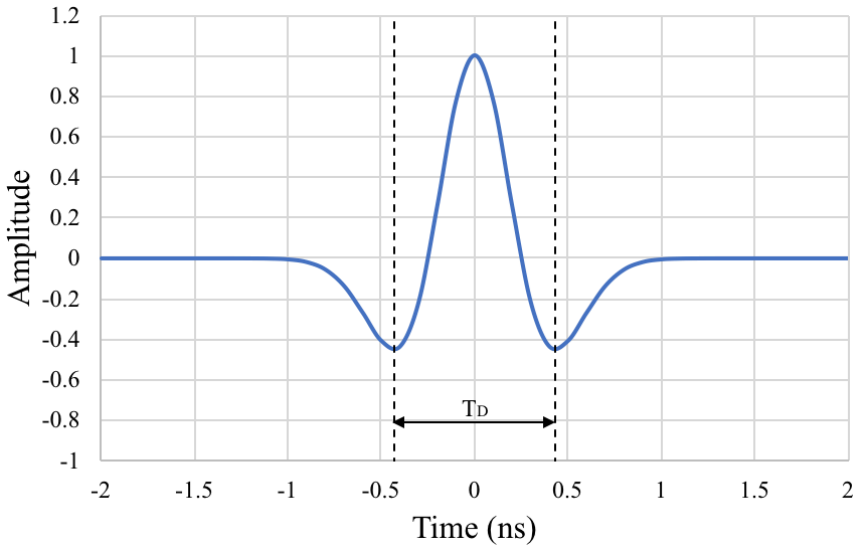

Figure 2.4 900 MHz Ricker wavelet

Radial resolution describes the ability to differentiate between reflected signals at the top and bottom of a void, stratigraphic layer, or object in the subsurface. In order to receive the top and bottom reflection separately to resolve the thickness, the two signals must arrive independently to eliminate constructive interference. Therefore, the radial resolution, Δr, can be defined by the pulse width and the known material velocity (v), such as:

$$\Delta r \geq \frac{T_D \cdot v}{4} \tag{2.21}$$

This equation indicates that higher central frequency pulses will have greater radial resolution. It should also be noted that in reality the bandwidth of the EM pulse is affected by attenuation and will change with propagation. Increased attenuation will cause the bandwidth to become greater (Daniels, 2004). As higher frequency signals have greater attenuation, the radial resolution will be more affected by depth. Theoretical radial resolution values for the different materials encountered in the Rondout tunnel are described in section 4.3.3 .

In addition to the intrinsic radial resolution based on the signal frequency, the GPR sampling frequency can also limit the radial resolution. Sampling frequency defines the amount of points sampled in a given time. This value is typically pre-defined in modern GPR equipment at a rate greater than the central frequency so as not to induce additional resolution limitations.

Lateral resolution defines the ability to distinguish between two adjacently located objects, or the ability to delineate the width of a small object. A very small buried object with adequate impedance contrast will induce a reflection of an EM wave, however, the radargram may depict a laterally-undefined parabolic reflection when the object width is below a threshold. The lateral resolution is dependent upon the depth, d, of the object, since the EM wave spreads as it propagates, and can be defined by:

$$\Delta l = \sqrt{\frac{d \cdot v}{2 \cdot f_M}} \tag{2.22}$$

Lateral resolution is closely related to the Fresnel zone concept, which describes the spreading wave front with depth dependent on signal frequency (Olhoeft, 1998; Cassidy et al., 2011). At shallow depths, lateral resolution is also limited by the spacing of the transmitter and

receiver on the antenna if this is greater than the calculated Δl. Additionally, similar to the sampling frequency limitation for radial resolution, the prescribed number of scans per distance of the GPR unit should be accounted for as this may also create a limitation on lateral resolution. Generally, GPR units can define scans per distance to be greater than the limiting lateral resolution of the antenna.

2.2.6 GPR Tunnel Case Studies

Parkinson and Ékes (2008) presents a field case-study of GPR inspection on a previously constructed water supply tunnel near Victoria, Canada. The tunnel was constructed in the 1960s and 1970s with drill and blast methods after a short section of TBM construction was halted due to poor ground conditions. The tunnel was not originally contact grouted which has since led to the presence of voids behind the liner. A 1 GHz GPR antenna from Sensors and Software was used for longitudinal surveys after construction. The presented radargrams display areas with heavy rock bolt frequency, honeycombing concrete, timber supports, and void anomalies. Air voids were identified separately from wooden supports by their unique geometric reflection signatures. Void thickness was not able to be determined. In total, 243 distinct voids were recognized with the GPR. Clear delineation was possible at the concrete-rock interface, demonstrating the undulating nature of the liner thickness from the drill and blast methods. This field case presented a successful investigation using GPR at detecting both voids and the liner-rock interface. However, no two-component grout was used in the original tunnel construction.

Zhang et al. (2010) presented GPR assessment on metro tunnel lines in Shanghai, China constructed using a TBM with segmental liners in silty clay and backfilled with a two-component grout. This paper provided the most relevant work to the current project being studied. Laboratory dielectric measurements using a VNA were made on grout samples and GPR penetration tests were conducted on the segmental liner to determine the optimal frequency. Grout effective permittivity values measured at 3 days and 14 days had values of 27 and 18 respectively. The imaginary part of the permittivity, or effective conductivity, was not mentioned from the VNA measurements. EM wave velocity with the 1 GHz antenna through the 35 cm thick liner was found to be 0.0933 m/ns. Field results suggested success of the 250 MHz and 500 MHz antenna at detecting the grout-soil boundary, while the 1000 MHz antenna's penetration depth was too shallow. No discussion was presented in this report about the attenuation of EM

signals through the grout, nor was there explicit proof of the GPR penetration through the grout aside from interpretations of the presented radargrams.

Yu et al. (2016) presented similar GPR evaluation to Zhang et al. (2010) on the Nanchang metro tunnel in China. The tunnel is a TBM constructed tunnel with segmental liner and grout backfill. The grout material composition was not provided, but was described as a mix of water, sand, cement and air. Penetration tests on a segment using a MALA 800 MHz antenna with an underlying steel plate were conducted. Penetration tests on a grout block were also conducted with only the ground beneath the block acting as a reflector. The permittivity of the segment was estimated to be eight based on the penetration tests. Radargram results for the grout block demonstrated a linear reflection band eight ns after the primary reflection. However, without the use of a partial reflector, this reflection band can be the base of the grout or simply a duplicate reflection. Effective conductivity of the segment and grout were not described in the numerical modeling. Field results were presented with assessment of the grout-soil boundary. Possible voids were identified in the radargrams, but were not independently verified.

Lalagüe et al. (2016) investigated the use of GPR for rock fall detection behind concrete tunnel liners with air void gaps between the liner and the in-situ rock. Several types of GSSI equipment were tested, including stepped frequencies, air-coupled (ac) and ground-coupled (gc) antennas. Frequencies ranged from 400 MHz to 2.6 GHz. Experiments were conducted in a tunnel as well as on a constructed concrete wall with rebar. Rocks that were placed against the concrete liner were detected based on the back-side reflection at the rock-air interface since the dielectric contrast between concrete and rock is too small to create a significant EM wave reflection. The most effective antenna was the 1.5 GHz (gc) antenna which allowed for the broadest range of rock sizes detected and a penetration depth up to 1 m. The 400 MHz (gc) antenna did not prove successful in identifying the rocks due to its poor resolution while the 2.6 GHz (gc) antenna was best at detecting small rocks but could not detect large rocks due to its small penetration depth. The (ac) antennas proved less effective compared to the (gc) antennas. This research provided valuable insight into various antenna types and their penetration depths through reinforced concrete as well as the ability to detect materials based on their back-side reflection.

2.3 Impact Echo

The impact echo (IE) method uses seismic wave pulses induced through a medium and measures the reflection response off material boundaries. As a seismic wave travels through a medium, it will reflect off boundaries of materials with differing seismic velocities and densities. The impact echo method utilizes this contrast to determine the depth of a boundary and has the potential to differentiate material boundary types based on the response of the reflection. The physics background of elastic wave propagation is described in this section, which is necessary for the interpretation of IE data.

2.3.1 P-Wave Propagation

Elastic (seismic) waves that propagate in the direction of particle motion are known as compressional waves, or P-waves. These types of longitudinal waves travel due to an induced transient stress gradient in the medium. Acoustic, ultra-sonic, and sub-sonic waves are types of compressional waves that are defined based on whether they are at, above, or below the human audible frequency range. P-waves can be described by a form of the wave equation related to the volume change in a material with respect to time (Everett, 2013):

$$\rho \frac{\partial^2 \Delta}{\partial t^2} = (\lambda + 2\mu)\nabla^2 \Delta \tag{2.23}$$

where ρ is the material density, λ and μ are the Lamé parameters, and Δ is the dilation of a body. Δ is given by the trace of the strain tensor (Everett, 2013):

$$\Delta = \varepsilon_{xx} + \varepsilon_{yy} + \varepsilon_{zz} \tag{2.24}$$

where ε_{ii} is the relative increase in length along the *i*-axis. Substituting velocity in place of the density and Lamé parameters gives the familiar form of the wave equation (Everett, 2013):

$$\frac{1}{V_P^2} \frac{\partial^2 \Delta}{\partial t^2} = \nabla^2 \Delta \tag{2.25}$$

where V_p is the P-wave velocity through a medium defined as $V_P = \sqrt{(\lambda + 2\mu)/\rho}$. The P-wave velocity can also be written in a more familiar manner in terms of bulk modulus, k, and shear modulus, μ, as (Everett, 2013):

$$V_P = \sqrt{\frac{k+4\mu/3}{\rho}} \tag{2.26}$$

Any material that can be defined by a bulk modulus and density is capable of transmitting a compressional wave. This includes solids, liquids, and air, but does not include vacuum. Seismic waves which propagate through earthen material and reach an air-boundary will dissipate the majority of their energy and therefore air cannot typically permit the transmittance of a seismic wave for any significant distance.

2.3.2 Elastic Properties of Materials

As described in section 2.3.1 , the compressional wave velocity through a material is dependent upon the elastic properties of a material, defined by k, and μ. The bulk modulus, k, can be further described by a materials inherent volumetric change when subjected to an isotropic force, such as (Everett, 2013):

$$k = \frac{F/A}{\Delta V/V} \tag{2.27}$$

The significance of the bulk modulus in the P-wave velocity formula necessitates a deeper understanding of the components of a material which effect this property. In a homogenous solid material, the P-wave velocity can be simply derived from the known material properties. However, in porous media, such as soil, rock, and cementitious mixes, the P-wave velocity is a function of the compositional velocities within the material. As an elastic wave travels through a non-homogeneous material, the different phases and components of the material will act in a complex interaction with one-another to allow for energy dissipation. Some known P-wave velocities of different materials are given in Table 2.2.

Table 2.2 Values for P-wave velocity and density of common geomaterials (Bourbie et al., 1987; Everett, 2013)

Material	P-Wave Velocity (m/s)	Density (g/cm^3)
Air	343	$1.2x10^{-3}$
Sand (dry)	200-1200	1.5-1.7
Sand (saturated)	800-2000	1.9-2.1
Clay (saturated)	1100-2500	2.0-2.4
Water	1450-1500	1.0
Limestone	2500-6500	2.4-2.7
Shale (saturated)	1100-2500	2.0-2.4

The range of velocities for porous media reflects the range in internal structure and density. Additionally, P-Wave transmission can be dependent upon the temperature and pressure of a material, which is reflected in the range given for water. Concrete, which can be composed of a wide-array of aggregate type, admixture, water, and cementitious materials, has a wide range of seismic velocities and densities. Furthermore, the amount of set-time for concrete also impacts the P-wave velocity as concrete gains strength and stiffness over time. During this time, phase changes from liquid-plastic-solid take place within the pore space when the cement particles hydrate in a chemical reaction. While simple soil mixtures and rock types can be somewhat predictable in terms of their seismic velocities, concrete velocity over set time is difficult to predict without a good understanding of the chemical reactions taking place and knowledge of the ultimate strength properties of the concrete as it sets.

2.3.3 Impact Echo Method

The Impact echo method is based on the reflection of a seismic wave as it travels through one medium and reaches the boundary of a second medium with differing elastic properties. The amount of energy that is reflected off a material boundary when the incident wave is normal to the material boundary, is defined by the reflection coefficient:

$$R = \frac{\rho_2 V_2 - \rho_1 V_1}{\rho_2 V_2 + \rho_1 V_1} \tag{2.28}$$

The product of velocity and density of a material is also referred to as the material's seismic impedance. The amount of energy reflected from the material boundary is proportional to the square of the reflection coefficient (R^2). Thus, the amount of energy transmitted through the boundary is equal to $1-R^2$. This reflection coefficient does not take into account an incident wave at an angle to the material boundary, but for the IE analysis, this will be considered inconsequential since the source is close enough to the receiver such that the angle of incidence can be approximated to be normal. As the source moves further from the receiver, the amount of energy reflected at the boundary will be affected by the angle of the incident wave.

A wave that is sent through a concrete medium will reflect off the first material boundary it encounters. The returned wave will then reflect again off the concrete surface boundary, where nearly 100% of the energy is reflected due to the small impedance of air. This phenomenon can be described as a ringing effect when a wave reflects back and forth within a material off the confining boundaries. The wave energy will eventually attenuate as it loses more energy at the material interfaces as well as due to scattering caused by impurities within the medium it is travelling through. The collected wave information can then be transformed using a Fast Fourier Transformation (FFT) method to categorize the different frequencies of the received waveform based on the relative amplitudes. For a large impedance-contrast boundary, where most of the wave energy rings between the boundaries, the peak frequency can be described as a resonant frequency (f_r), which is related to the material thickness (h) and velocity (V_p) by:

$$f_r = \frac{\beta V_p}{2h} \tag{2.29}$$

where β is a correction factor depending on Possion's ratio of the material. A typical value of β = 0.96 is used in concrete structures (Ryden et al., 2013).

When the incident seismic wave reaches a boundary of smaller impedance contrast, the amount of energy reflected will be diminished, and the FFT response will display a less prominent f_r peak. Figure 2.5 demonstrates idealized responses of an IE signal for different types of material boundaries behind a concrete structure. Ryden et al. (2013) described a quantitative method for assessing the prominence of the f_r peak in the FFT data by use of a quality factor (Q).

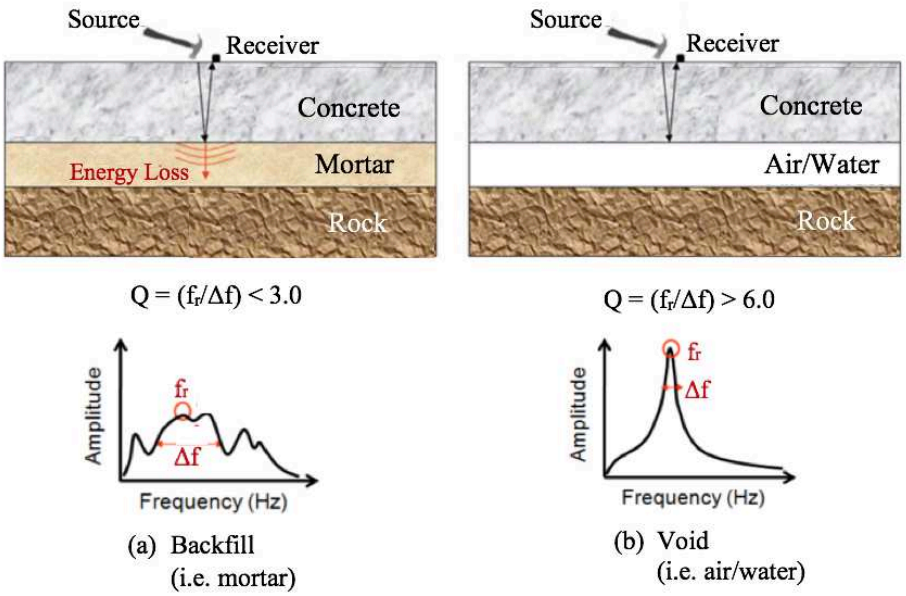

Figure 2.5 Characteristic forms of FFT data for backfill and void behind a concrete liner (modified from Ryden et al., 2013) © 2013 by RILEM, reprinted by permission of Springer Nature

Q is calculated based on f_r and the width (Δf) of the resonant peak at the half power bandwidth ($\sqrt{2}/2$):

$$Q = \frac{f_r}{\Delta f} \tag{2.30}$$

Q provides a sensitive method to material type boundaries for detecting flaws in the backfill material behind a concrete liner. Use of Q inherently eliminates the need to calibrate the source impact since the method uses a relative amplitude peak to the peak width (Ryden et al., 2013). This provides ease of use in a field setting where uniformity in data collection can be challenging.

FFT data can also be used in a visual inspection aid to determine the secondary boundary behind the backfill material of the tunnel lining (Aggelis et al., 2008). This requires more interpretation experience as noise can become prominent in the IE response. In theory, for good backfill material, little energy will be reflected at the liner-backfill boundary, but additional energy will reflect off the backfill-in-situ-material boundary. This will create a second peak in the FFT data set which can indicate the secondary boundary depth. In general, impact echo can be used for void detection, but not void size delineation (Razak et al., 2015).

2.3.4 IE Tunnel Case Studies

Aggelis et al. (2008) presented a case study with the use of IE in a tunnel setting. The tunnel being constructed was a utility tunnel built with a TBM in central Japan and constructed in low quality mudstone. Two-component grout backfill was used to fill the annulus space. The two-component grout used in the tunnel had a high bentonite to cement ratio (4:1) and a high water to cement ratio (4.25:1). Elastic properties of the grout were presented with the P-wave velocity of 1631 m/s. The concrete segment used in the tunnel was 225 mm thick with a P-wave velocity of 5000 m/s and a density of 2.5 g/cm^3. The paper discusses the main goal of the work to differentiate partially filled annulus space from a fully filled space by recognizing a secondary frequency peak at a lower frequency in the FFT data, compared to the main resonance frequency. Two data sets of FFT soundings were presented showing two cases; one comparing a fully-grouted annulus space data to a partially-grouted annulus space data where the two data sets where clearly distinguishable; and one where a partially- grouted annulus and fully-grouted annulus were indistinguishable. Therefore, it was concluded that attempting to analyze IE data by sole visual inspection of the FFT data for a secondary peak at the grout-rock interface is not a sufficient NDT technique for comparison of a fully grouted annulus to partial washout cases. However, further analysis was presented by looking at the time domain of the IE response, in which more distinguishable features were found in the fully grouted vs partially grouted cases. The analysis presented works on a similar concept to the one that the Q analysis utilizes. The paper did not present any use of the Q technique.

Kang et al. (2017) presented an investigation using the IE technique to detect cavities behind concrete sewage pipelines. A mock-concrete half pipe, 55 mm thick, was constructed on top of fabricated voids to determine the capabilities of the IE method. The backfill material behind the concrete was sand, and the void was air-filled. IE data analysis included methods in the time domain, such as the sustained duration of the acoustic signal. This technique is similar to the technique presented by Aggelis et al. (2008). The sustained duration technique utilizes the ringing effect of an elastic wave reflecting off a void compared to lower impedance contrast boundary such as sand. Clear distinction was able to made in the time domain for detecting the cavity. The Q method was not discussed in this work which operates on similar principles as the sustained duration but analyzes data in the FFT form rather than the time domain.

CHAPTER 3
RONDOUT TUNNEL PROJECT, METHODS, AND MATERIALS

3.1 Construction Method

An open-face TBM was selected for tunneling the entire 4 km (2.5 mile) alignment. Before assembling the TBM, a shaft and cavern, referred to as the starter tunnel, were blasted out underground at the elevation at which the TBM was launched. The TBM was assembled underground and a steel head-frame was used as the initial reactionary force to start the TBM advancing into the in-situ rock. The first ten rings assembled were initially supported by wooden blocks, and later backfilled with concrete. After launching the TBM, construction methods consisted of mining pushes, in which the machine thrusts forward using hydraulically powered thrust cylinders with the previously built rings providing a reaction force. While thrusting, a cutter head equipped with rock cutter discs rotates and breaks the in-situ rock. Excavated material falls through openings in the cutter face and is transported out of the machine via a conveyer belt. The conveyer belt then dumps the material into train bins which get lifted out of the tunnel from the shaft. After a mining cycle is complete, six prefabricated concrete segments are installed to form a single ring using a ring erector. Since the cutter head must be a larger diameter than the segmental liner, an annulus gap is left between the tunnel liner and rock excavation which must be backfilled. During the next mining cycle, as the TBM advances, it continuously injects grout into the annulus gap between the liner and rock cut.

3.2 TBM Specifications

The Rondout Tunnel Project uses a single shield open-face TBM with a 6.6 m (21.6 ft) excavation diameter and sealable excavation chamber sufficient up to 30 bar (435 psi) of pressure. A model of the Rondout TBM, called Nora, is shown in Figure 3.1. The pre-cast segmental liner installed inside the TBM tail shield has an outside diameter of 6.2 m (20.3 ft), which creates an annulus space of approximately 19.8 cm (7.8 in) between the rock and the liner. A two-component grout, also referred to as A-B grout, is continuously injected into the annulus space through the back of the tail shield as the TBM advances. Two-component grout is transported as separate components and mixed upon ejection into the annulus space, where it is designed to have a high early strength to support the weight of the TBM as it passes over the

segments. Spring plates on the tail shield exterior and four sets of brushes on the interior are designed to prevent grout from back flowing into the TBM or into the excavation chamber, shown in Figure 3.2. These brushes are capable of withstanding up to 30 bar (435 psi) of pressure. Six grout injection ports are located on the tail shield, two below the spring line and four above, one of which is depicted in Figure 3.2. Grout is injected from four of the injection portals during production with each portal capable of approximately 110 L/min (29 gpm), for a total of 440 L/min (116 gpm) into the annulus space.

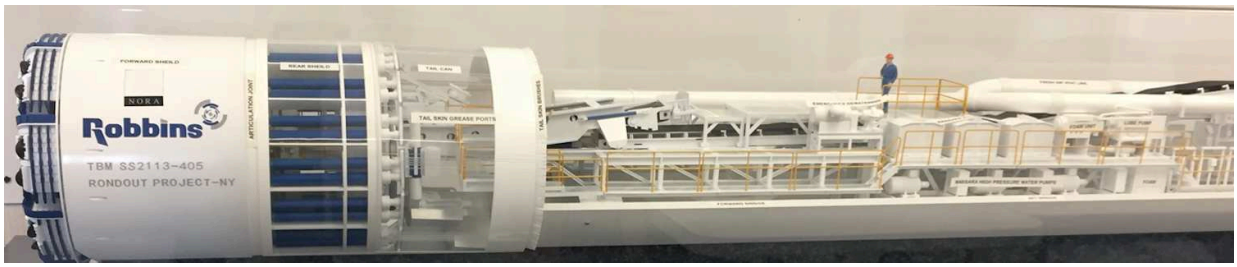

Figure 3.1 Model of the Rondout TBM "Nora"

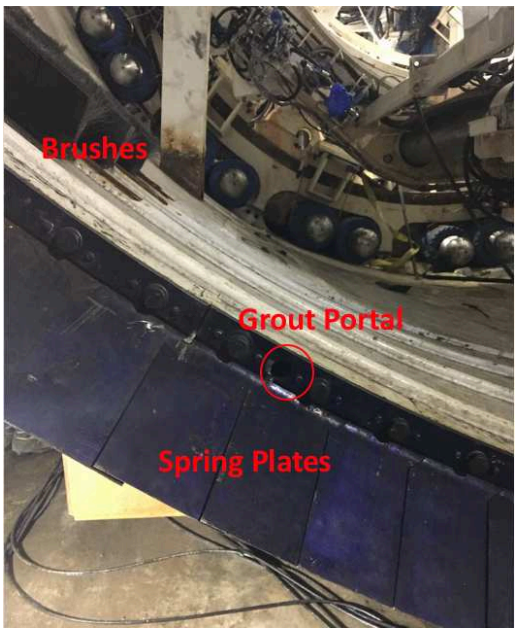

Figure 3.2 Photo of the tail shield on the Rondout TBM

Segmental liner rings are composed of six individual pre-casted segments that form a complete circle, as shown in Figure 3.3. Each segment has tapered edges to allow for directional steering of the tunnel by positioning one key piece at different radial positions. Five segments are

composed of 67.25-degree arcs with 3.1 m (122 inch) outer radius, 33 cm (13 inch) thickness, and 152 cm (5 ft.) width. The sixth piece, referred to as the key piece, is a 22.5-degree arc with the same thickness and width. The double-matted rebar cages molded in each segment are separated by approximately 19.5 cm (7.65 in) and embedded 3.8 cm (1.5 in) in the segment forming a variable grid array with rebar spacing between 13.4 cm (5.28 in) and 21.6 cm (8.5 in). Rebar diameters include 15.7 mm, 15.17mm, and 13.75 mm. Details of the rebar cage are shown in APPENDIX A.

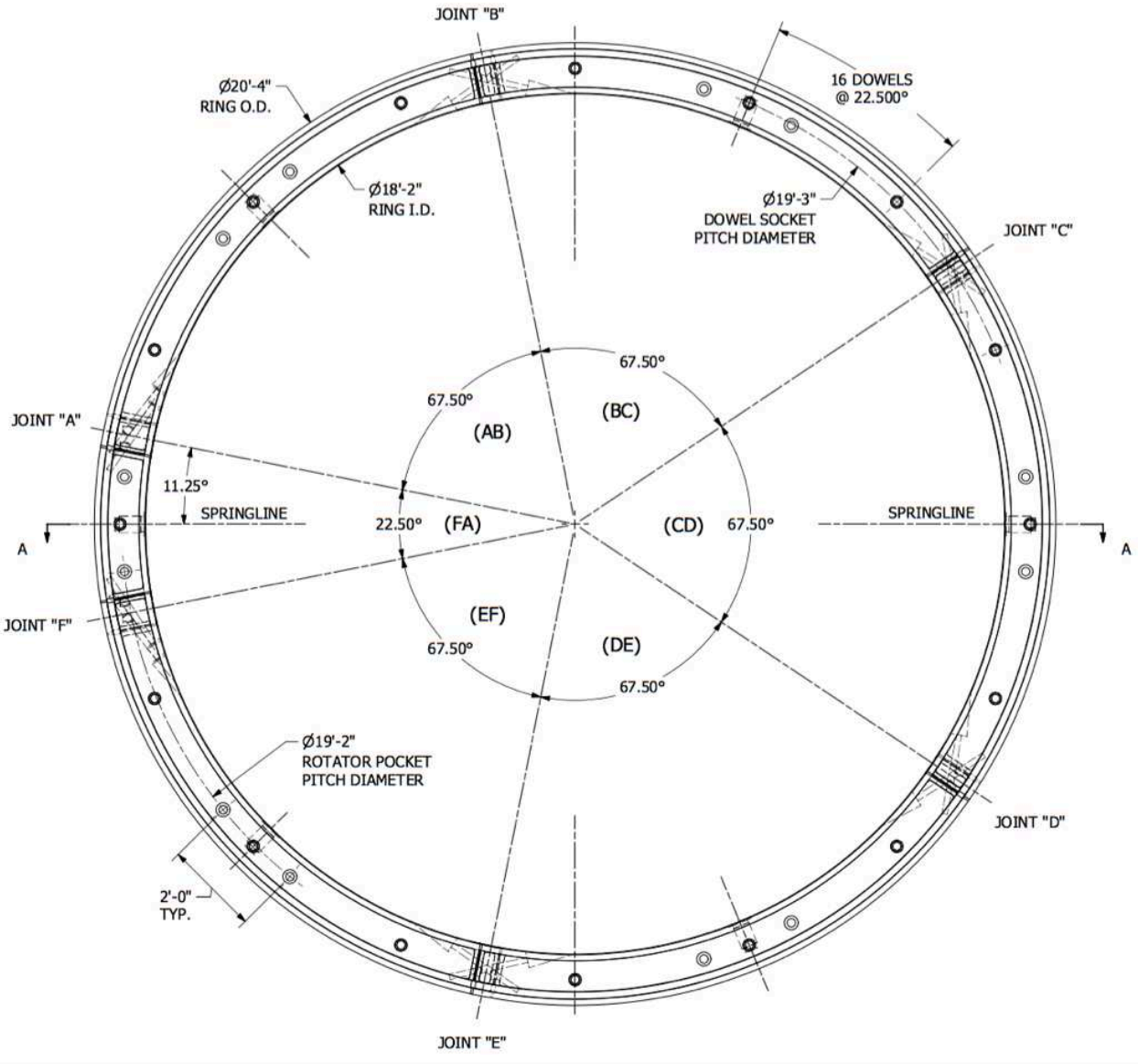

Figure 3.3 Segmental liner ring configuration

3.3 Annulus Grout Mix

The two-component annulus grout mix design for the Rondout Project is comprised of water, bentonite, cement, retarder, and sodium silicate accelerator. The first four ingredients mixed are referred to as component A while the accelerant is component B. A water to cement ratio (w/c) equal to approximately 2.2 was used and accelerator dosage is between 6 and 12 percent by volume. This proprietary mix was specially designed to meet the annulus grout requirement set by the owner displayed in Table 3.1. As discussed in section 2.1, the grout must maintain a stable, flowable mixture until injected in to the annulus space, where it then must gel within seconds and quickly gain strength and stiffness. The highly fluid component A enables pumpability but also creates a relatively low final strength as compared to ordinary cementitious mixes that can have 28 day curing strengths more than ten times greater than the two-component grout. However, the strength-gain rate and pumpability of the mix take precedent over the final strength of the grout.

Table 3.1 Two-Component Grout Design Requirements

Property	**Value**	**Set Time**
UCS (psi)	25	1 Hr
	150	24 Hr
	300	7 Day
	500	28 Day
Gel Time	< 15 s	
Bleed	< 4 %	
Viscosity	< 55 cp	

Component A of the grout is batched in a colloidal mixer above ground on the project site and then transferred to an agitator tank where it is held until being transported by pipes into the TBM. The Portland cement being used is an ASTM C150 Type I/II low alkali type with its chemical properties and cement potential phase composition, as designated by the supplier, listed in Table 3.2 and Table 3.3 respectively.

Table 3.2 Cement Chemical Properties (ASTM C150)

Item	Test Result (%)
SiO_2	19.45
Al_2O_3	4.72
Fe_2O_3	3.55
CaO	63.34
MgO	3.15
SO_3	2.74
Ignition Loss	2.02
Na2O	0.18
K2O	0.55
Insoluble Residue	0.18
CO_2	1.3
Limestone	3.1
$CaCO_3$ in Limestone	90

Table 3.3 Cement Potential Phase Composition (ASTM C150)

Item	%
C_3S	60
C_2S	10
C_3A	6
C_4AF	11
$C_4AF + 2*(C_3A)$	23
$C_3S + 4.75*(C_3A)$	91

3.4 Existing QA Method for Annulus Backfill Grout

Physical evaluation for the quality assurance of the backfill grout is currently completed by drilled holes though the segment and annulus space. Holes are drilled with a ¾ in drill bit through the center lifting portal of the segment, approximately halfway thru the segment

thickness (13 in). Therefore, the rock interface is expected to be reached 15 in into the hole. This process involves a four-step procedure for verification of complete annulus grouting:

1. While drilling, water flows are recorded that come out of the drilled hole.
2. After drilling, visual inspection is made with a flashlight and human eye peering down the hole.
3. Probe rods are pushed down hole and manually probed to feel for complete grouting along the drilled hole walls.
4. A camera is pushed down hole and video is recorded inside the probe hole.

The total combined four-step procedure provides evidence for the state of grout at that location, with a lack of water flow being the primary source of evidence for good grouting. In theory, while the drill is still within the annulus space, complete grouting would prevent water from flowing out of the drill hole. Photos and videos taken within the probe holes have not shown clear evidence for complete grouting through the entire annulus space. As discussed previously, this destructive means to evaluate the annulus backfill grout is sought to be replaced by the findings of this research. Holes put through the segment are time consuming to complete and require extreme caution with the high-water pressures existing along the tunnel alignment. Furthermore, this method does not provide lateral information on the quality of backfill grout as it is a point measurement.

CHAPTER 4
LABORATORY STUDIES

Laboratory studies were performed on the two-component grout designed for the Rondout tunnel in order to assist in the geophysical data assessment. These laboratory studies included defining material properties related to the transmittance of both EM waves and Elastic waves. Properties characterized include electrical conductivity, dielectric permittivity, P-wave velocity, and density. This chapter provides methods, materials, results and discussion for each of the properties investigated.

4.1 Two-Component Grout Preparation

Two-component grout was prepared for the various laboratory experiments according to the mix design described in section 3.3. This grout was designed for the Rondout Bypass Tunnel project and represents a typical two-component grout. Grout component A was mixed using a hand drill with a Jiffler shear mixing attachment for the purposes of laboratory studies, as shown in Figure 4.1. The shearing capabilities of the drill attachment are similar to the shearing of the colloidal mixer used on the tunnel site. Components were individually mixed together with times designated by the grout mix designer.

Figure 4.1 Photos of grout mixing process and pouring into cubic molds

Different methods were used for mixing the accelerant depending on what mold the two-component grout was to be set in. For cubic specimens, accelerant was poured into the component A while the shear drill was left mixing for 3 seconds. The combined components were then quickly poured into 2x2x2 in cubic molds. The molds were initially saran wrapped and left in laboratory atmospheric conditions. After one hour the cubes were taken out of the mold

and individually saran wrapped. Cubes were placed in a cooler kept at laboratory temperature (19 °C±2°C) and maintained at nearly 100% relative humidity, monitored by a digital humidity gauge.

4.2 DC Electrical Conductivity

Electrical conductivity of the two-component grout was measured on laboratory prepared samples using a four-electrode resistivity meter in order to predict GPR signal attenuation. Previous studies (Karlovšek et al., 2016), as well as field GPR results, indicate that the two-component grout has exceptionally high attenuation properties even after the material has set. These results are not comparable to ordinary single component grout or ordinary concrete where GPR signal attenuation significantly reduces over set time and allows for reliable GPR performance (Tumidajski, 1996; Rajabipour and Weiss, 2007; Topcu et al., 2012; De Rosa et al., 2016). Therefore, an in-depth study of the grout's electrical conductivity was necessary to determine which elements within the two-component grout are contributing to the GPR signal attenuation. Ultimately these results may be used as an aid in future two-component grout designs to incorporate GPR signal attenuation as a design consideration.

In these experiments, the percentage of sodium silicate accelerant in the mix was controlled as an independent variable and observations on the effect of set-time were taken. Additionally, grout with aluminum-sulfate accelerant was tested to compare the two types of accelerants. Conductivity measurements of the individual two-component grout constituents were used to provide baseline assessment for the cause of high electrical conductivity.

4.2.1 Methods and Materials

Two-component grout was tested as well as individual constituents of the grout mixture. Specially designed grout tubes were constructed and tube resistance was measured over set time. Specifics of each of the materials used in these experiments and the testing methods are provided herein.

4.2.1.1 Electrical Conductivity Testing Apparatus

A four-point electrode method with a Mini Res electrical resistivity meter was used to measure the electrical resistance of the grout. A laboratory test setup was implemented in which

grout was poured into a PVC tube with two electrodes in the middle to measure voltage drop and an applied current to the two end electrodes. The test setup was a combination of test setups described for resistivity test methods of concrete and soil (Instruments, 2010; Layssi et al., 2015).

The Mini Res manual describes an experimental test setup for soil testing in a laboratory setting, which was adapted in cylindrical form for the grout testing as depicted in Figure 4.2. This method uses a tube with a current applied at the two ends and the voltage drop measured across the center. A tube was used instead of a rectangular testing apparatus, as it provided a simple means of casting the grout specimen in an inexpensive and repeatable fashion.

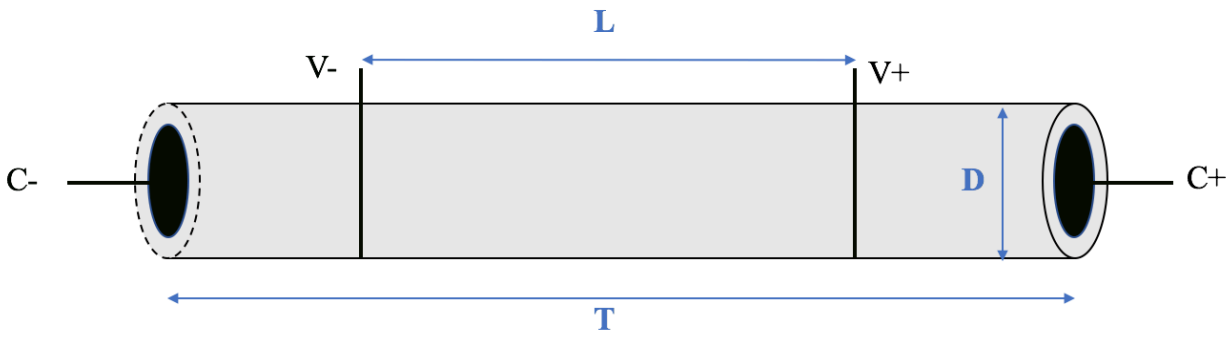

Figure 4.2 Laboratory electrical conductivity test setup, adapted from the MiniRes manual

The cylindrical setup allows for an easily manufactured apparatus by using a PVC pipe with end caps. Test tubes were made from 10 in long PVC pipes with a 1.5 in inner-diameter. The end caps were made from PVC caps with galvanized-plated steel washers on the inside of the cap, attached to a bolt sticking through the cap to act as electrodes. These electrode tips allowed for the MiniRes alligator clips to be attached with an applied current. Silicon was placed around the bolts where they pierced the end caps to ensure fluid solutions would not leak during calibration and that no moisture could enter or escape the tube during curing. Two galvanized nails were put through the center of the pipe at 6 in spacing, 2 in from the tube ends, where the voltage differential was measured. The two-component grout was poured directly into the testing tube with the nails already in place to form good contact with the embedded electrodes. Figure 4.3 displays photos of the MiniRes meter used and the test tube apparatus materials.

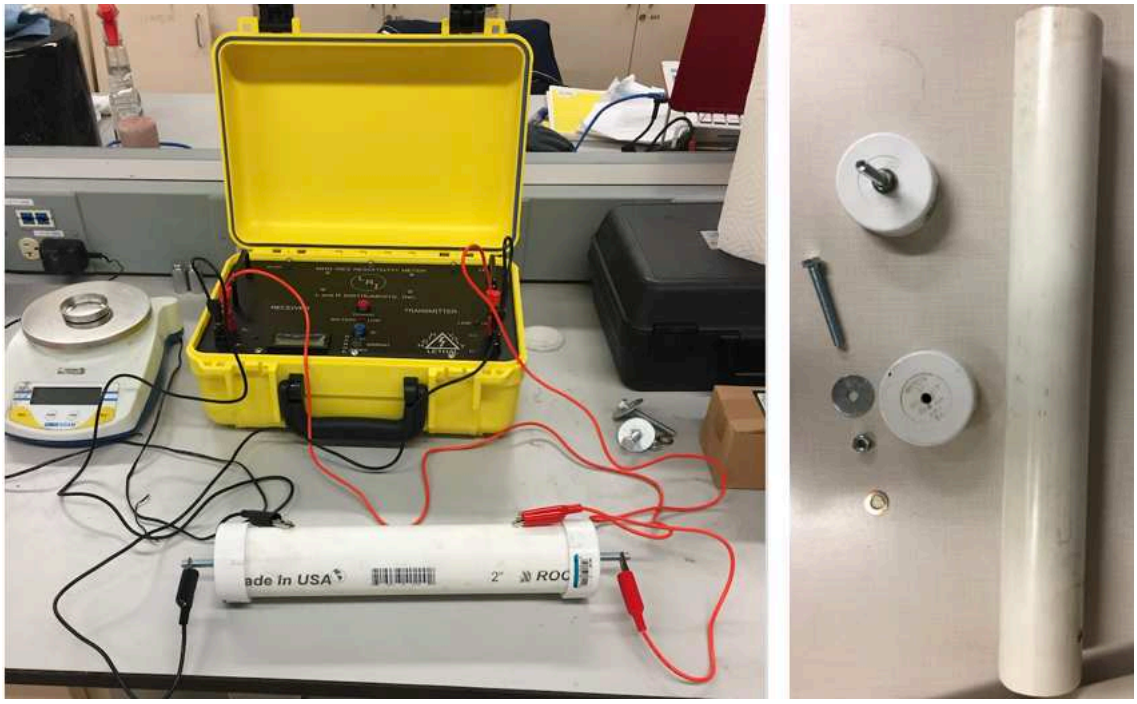

Figure 4.3 (left) Photo of testing tube connected to the MiniRes (right) Picture of test tube components disassembled

Various tube dimensions were experimented with to verify the tube dimensions did not impact the testing results. Results from the tube dimension experiments are shown in APPENDIX B. The final tube dimensions, including diameter, length, and voltage nail spacing, were designed to enable resistance readings within the MiniRes resolution for the full range of expected resistance of the various materials tested. Spacing of 5 cm between the voltage electrodes and end electrodes met the minimum spacing requirement of 0.75 cm determined by Han et al. (2007) to eliminate electrolysis effects at the end electrodes. A large ratio of cross-sectional area to voltage-electrode area was desired to minimize effects of the embedded electrodes on the measured resistance. Therefore, the largest possible grout volume was selected which could first be mixed with the accelerant and also enabled enough time to pour the mixed grout into the tube before gelling.

The MiniRes meter outputs a total measured resistance. This is the measured resistance of the equivalent circuit of the grout within the tube. A conversion from resistance to resistivity can be made according to the shape factor (Instruments, 2010):

$$\rho = R_{meas} \frac{A}{L_V} \tag{4.1}$$

where ρ is the electrical resistivity in Ω-m, R_{meas} is the measured resistance in Ω, A is the cross-sectional area through which the current flows, and L_V is the distance between voltage meter electrodes. The corresponding electrical conductivity of the material is the inverse of the measured resistivity:

$$\sigma = \frac{1}{\rho} \tag{4.2}$$

where σ, the electrical conductivity, is typically denoted in mS/m.

4.2.1.2 Tube Calibration

Each grout specimen was tested in a separate tube which required individual calibration. The tube calibration was required to eliminate errors from imperfect tube construction which could lead to systematic errors in the shape factor. A single point calibration procedure was developed to determine an additional multiplier variable in the shape factor used for the resistivity conversion.

Pure NaCl solutions using deionized water were mixed with a 10mg:1L ratio. The conductivity of the solution was first measured using a calibrated Vernier Conductivity Probe, and the NaCl solution was poured into the grout tube. Tube resistance was then measured and an α factor was calculated which was applied to all future testing with that tube. The α value was included as an additional term in the resistivity equation, such that:

$$\rho = R_{meas} \frac{A}{L_V} \alpha \tag{4.3}$$

The α value was evaluated so that the measured resistivity from the MiniRes matched the known conductivity of the solution using the probe. Measured α factors varied from 1%-5%. By using the α factor calibration technique, consistency among tubes was found to be within 1% deviation for the same grout mixes.

4.2.1.3 Two-Component Mixing

Component A was prepared according to section 4.1. Components A and B were then mixed together with the drill attachment as was done for the cubic molds, but were directly funneled into the conductivity tubes. Since gel time is less than 15s, the two components could only be mixed for approximately 3 seconds to leave enough time to fully fill the tube. One liter of component A was poured into a funnel with a closed ball valve, as shown in Figure 4.4, and mixed with the drill shear attachment. The required dosage of accelerant was then poured into the funnel and the two components were mixed for 3 seconds. Then the ball valve was opened to allow the mixture to pour into the tube with the bottom end cap attached. After the tube was filled with grout, the top end cap was secured.

Figure 4.4 Photo of funnel used for pouring mixed grout into electrical conductivity test tubes

4.2.1.4 Sample Curing and Testing

Tubes were connected to the MiniRes meter for timed-trial testing. Tubes were stored in a water-curing bath monitored at laboratory temperature (19 C) in between measurements. The two-component grout tubes were stored horizontally since the grout gels and cannot separate

inside the tube. Tubes with liquid mixtures of variable or no set time were stored vertically and tested vertically to ensure no air gap existed longitudinally in the tube which would affect the cross-sectional area used in the shape factor.

For the two-component grout, resistance measurements were conducted every 5 min for the first 30 min, then 15 min intervals until 1 hr, and then at 2 hr, 4 hr, 6 hr, 24 hr, 48 hr, 72 hr, 7 days and 14 days. For measurements on fluid mixtures less time intervals were conducted at early times since no major changes were occurring.

4.2.2 Results

Electrical conductivity test results are described according to the testing method and independent variables analyzed. Conductivity results for the mixtures and combinations of constituent grout materials provided evidence for the cause of high attenuation in the two-component grout.

4.2.2.1 Two-Component Grout with Sodium Silicate

Four different sodium silicate dosages were tested to demonstrate the effect of the accelerant percentage on conductivity. Figure 4.5 shows the results of the different grout mixtures over set time. The early effects of the accelerant create an initial spike in conductivity that reaches a maximum at about 30 min and then gradually decreases over a three-day period. The grout stabilizes near its final conductivity value after approximately three days. The dosage of accelerant was shown to have a positive effect on early set time conductivity, where the maximum conductivity reached at 30 minutes was largest with the 12% sodium silicate grout dosage and smallest with the 6% dosage. However, the long-term conductivity was shown to not be significantly affected by the percentage of sodium silicate. After approximately 2 hours, the conductivity values are inverted with respect to the sodium silicate percentage, with the highest dosage of sodium silicate having the lowest conductivity. This trend continues for the remainder of set time, but all grout mixtures asymptote near the same conductivity of approximately 900 mS/m. The conductivity measured after 14 days varied between 832 to 972 mS/m with the 6% dosage having the highest conductivity and the 12% dosage having the lowest.

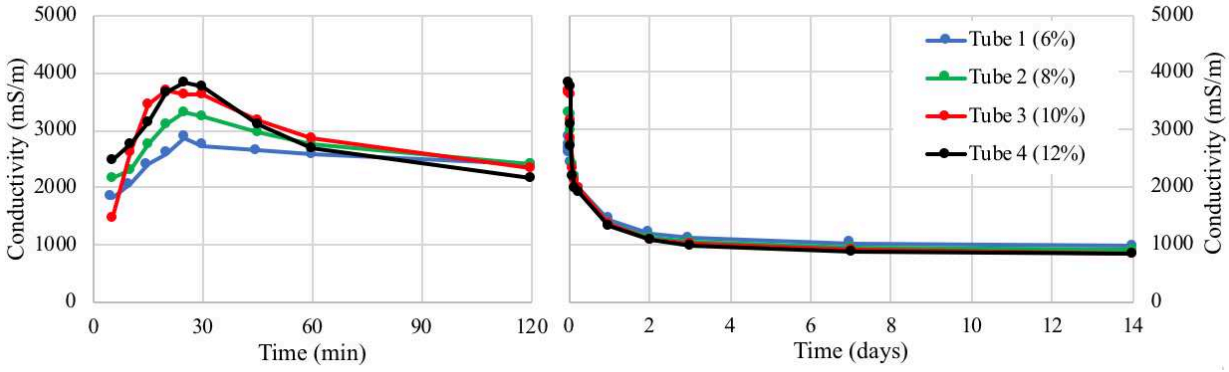

Figure 4.5 Electrical conductivity of two-component grout with variable sodium silicate percentages

The initial conductivity spike is associated with the initial gel period as the sodium silicate reacts with the grout mixture. After 30 minutes, the stabilized cement mixture begins to hydrate and gains strength over the 3-day period. This period of conductivity decrease matches the period of material strengthening evaluated by compressive strength and P-Wave velocity measurements. Leaching of ions into the grout solution also increases the total conductivity at early set times, as it has been shown that pore solution in a cementitious mix increases over set time (Harbec et al., 2016). The addition of ions to a solution increases the amount of mobile charge carriers.

4.2.2.2 Two-Component Grout with Aluminum Sulfate

To contrast the effects of a sodium silicate accelerant, a mixture using Aluminum Sulfate as the accelerant was tested. This accelerant is commonly used in shotcrete applications due to its fast reaction time. Due to the fast gel time with this accelerant (typically in less than 5 seconds), a modified procedure was required to test this material. Not enough time existed to mix the two-components and then pour the mixture into the tube before it gelled. Therefore, the two components were mixed together with the Jiffler drill and then compacted into the tube while in a semi-solid state. After gelling, the grout maintains a soft pudding-like consistency. This grout did not endure the same hardening that the sodium silicate provided and was still soft after multiple days of set time. An 8% dosage was used for two tube tests, results for each tube are shown in Figure 4.6.

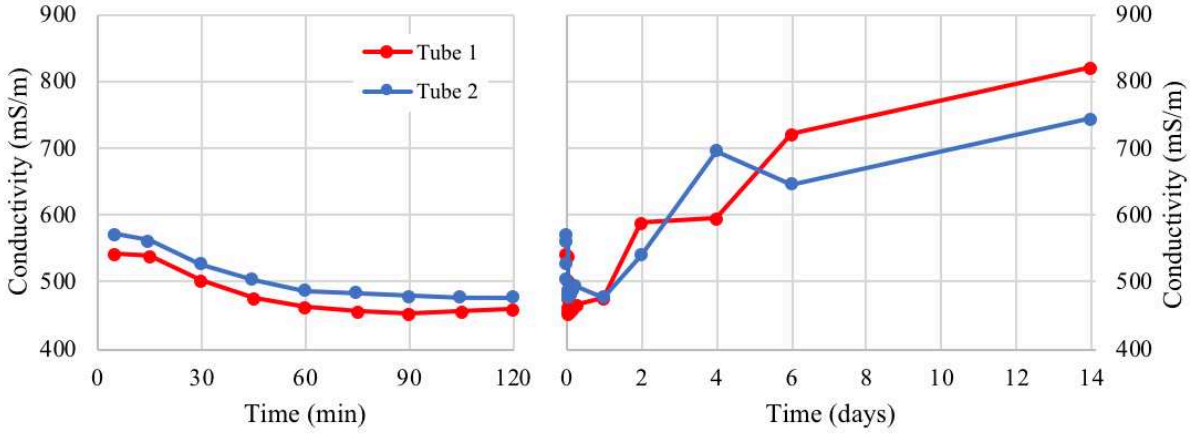

Figure 4.6 Electrical conductivity of two-component grout with 8% Aluminum Sulfate accelerant for two tubes mixed with the same procedure and components

The aluminum sulfate accelerated grout demonstrated different early-set time electrical conductivity behavior compared to the sodium silicate. The electrical conductivity started much lower, at about 550 mS/m and then rapidly declined to a minimum at 1 hr of 460 mS/m. After reaching a minimum, the conductivity continually increased for the remainder of the test to about 800 mS/m after 14 days. Unlike the sodium silicate, which creates a more conductive medium for electrical current when reacting to the cement solution, the aluminum sulfate inhibits the mobile ions in the pore solution leached from the cement. This causes the decrease in conductivity at early set time as the aluminum sulfate continues to react with the pore solution. The late time increase in conductivity may be due to the grout moving towards the conductivity of the remaining pore solution as ions continue to leach into the pore solution from the cement. The fluctuation in conductivity after two hours between the two tubes was not directly accounted for, but the average trend can be assumed to describe the physical impact of the aluminum sulfate on the grout.

4.2.2.3 Two-Component Grout Constituents

Individual constituents as well as solutions were tested to help determine which aspects of the grout induce the high observed total conductivity of the mixed two-component grout. Constituent solutions were placed in the tubes and procedures described for the two-component grout were followed. Results are displayed in Figure 4.7. The main differences between the two-

component grout studied and ordinary grouts and mortars are the sodium silicate accelerant, and the high water to cement ratio. Mixtures tested maintained the same grout mixture ratios in the two-component grout, described in section 3.3.

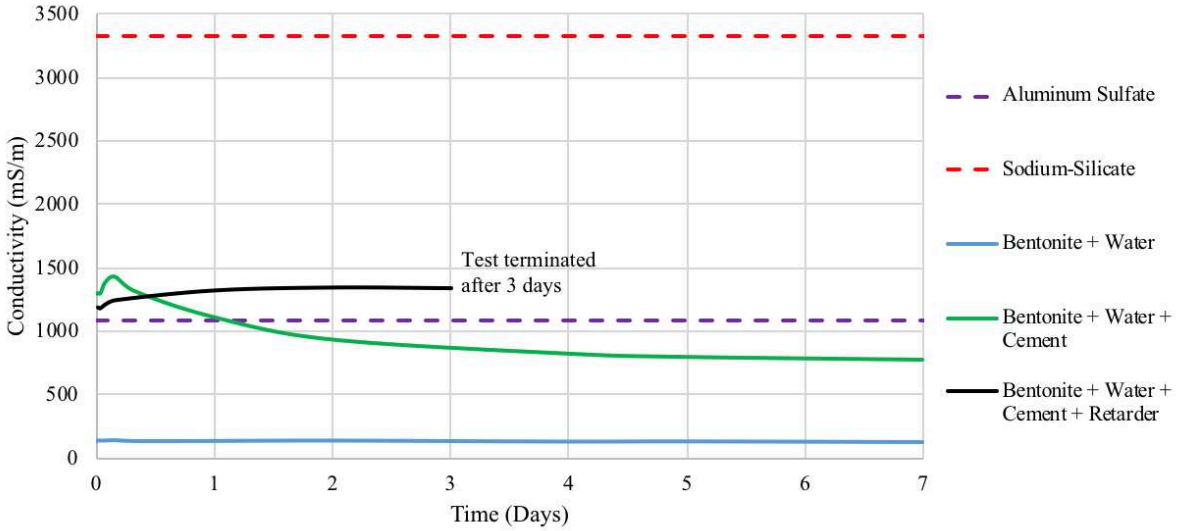

Figure 4.7 Two-component grout constituent conductivity. Aluminum sulfate and sodium silicate accelerants were point measurements. Component A was terminated after its assumed stability time of 3 days

Component A of the grout is composed of the Bentonite, water, cement, and retarder. This mixture will retain its fluid-consistency for several weeks, although the water will begin to bleed after only a couple days. In order to create consistent conductivity readings, the component A fluid was mixed to create a homogenous mixture before each reading. Since this material doesn't change phase in the time period studied, the conductivity change can be associated solely with the leaching of ions from the cement into the water. The conductivity reaches a steady value of approximately 1350 mS/m after 2 days.

The Bentonite, water and cement mixture (component A minus retarder), displays the conductivity change during cement hydration which solidifies the total mixture. The initial increase in conductivity can be associated with the leaching of ions into the solution, as observed with the component A. However, without the retarder in the mix, the initial conductivity is higher than that of component A. A decrease in conductivity after 2 hours is consistent with other cementitious mixtures as it solidifies (Rajabipour and Weiss, 2007). The bentonite, water, and cement mixture then decreases to a conductivity of approximately 770 mS/m after 7 days of

curing. This conductivity value is higher than literature values of other cementitious mixes after they have set, where conductivity values typically decrease below 100 mS/m (Tumidajski, 1996; Rajabipour and Weiss, 2007; Xiao and Li, 2008; Topcu et al., 2012; Weiss et al., 2013; Yousuf et al., 2017).

A bentonite and water solution was analyzed separately from the cement to provide a basis for evaluation of the amount of conductivity influence from bentonite. The mixture was tested over time to demonstrate any effects of continued adsorption of water molecules to the bentonite particles surface. No significant changes of conductivity were measured over the seven-day test duration. It is shown that the bentonite and water mixture had relatively low conductivity (137 mS/m) compared to that of the cement mixture. The value measured of the bentonite solution is within the range of conductivity for clays shown in Table 2.1.

Both sodium silicate and aluminum sulfate accelerants were also measured and plotted on the time scale, though they did not vary with time. Sodium silicate was found to have the highest conductivity value of any substance measured at 3325 mS/m, and the aluminum sulfate was measured at 1081 mS/m. The high conductivity value of sodium silicate may help explain the initial spike in conductivity measured in the two-component grout at earlier set time. The aluminum sulfate was higher than the conductivity of the two-component grout reached at early set times. This is evidence that the aluminum sulfate neutralizes some of the mobile ions in the component A solution fluid.

4.2.2.4 Water to Cement Ratios

After observing the high conductivity of the cement, water, and bentonite mixture after sufficient set time, further experiments were conducted to investigate the effect of the water to cement ratio (w/c) with respect to conductivity. It was shown that the high electrical conductivity in the two-component grout can be attributed to the higher w/c than more common cementitious materials with typical w/c of 0.6 or less. Four w/c mixtures were tested, with results shown in Figure 4.8, with w/c equal to 0.5, 1, 2.2, and 3.

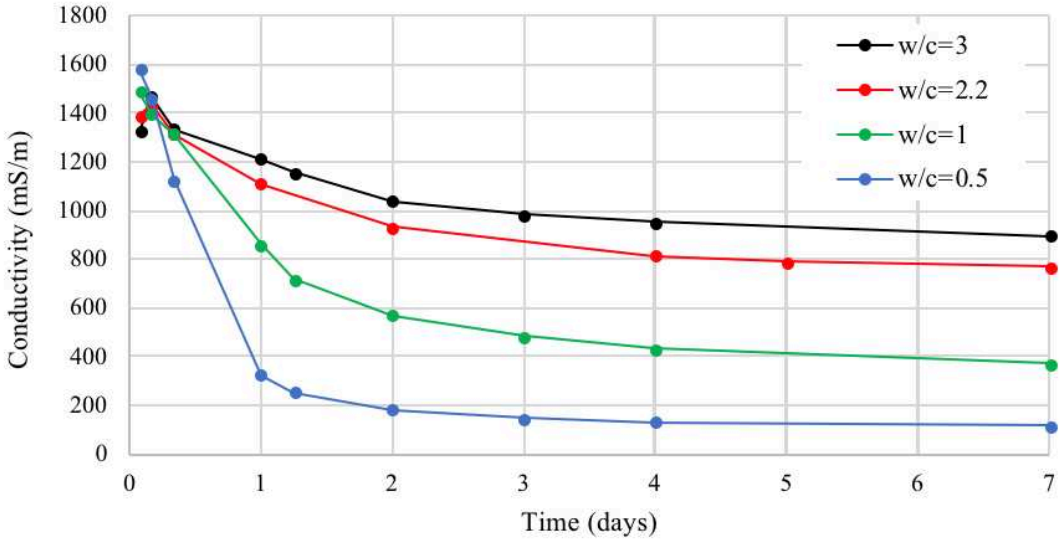

Figure 4.8 Conductivity for water, bentonite, and cement mixes with variable w/c

Results demonstrate that mixes with higher w/c ratios have significantly higher electrical conductivity after seven days of hardening. The mixture with a w/c ratio of 3, which other tunneling projects have used similar ratios (Aggelis et al., 2008; Flores, 2015), had a seven day hardening time conductivity of 897 mS/m, while the w/c of 0.5 had a seven day hardening time conductivity of 116 mS/m. The large contrast of conductivity is logical since with a high porosity cementitious mix, only a small portion of the water will be able to hydrate the cement particles, leaving more mobile ions present in the pore solution of the hardened mix. Even after the mixture solidifies, enough free water will exist in the pore space which can continue to conduct electrical current.

4.2.3 Discussion

Electrical conductivity testing revealed the total DC conductivity of the two-component grout to be relatively high compared to ordinary cementitious mixes, which provides an explanation for the observed high EM signal attenuation in the material. GPR attenuation would be worst in the grout at early set time due to the conductivity spike, but attenuation still remains significant even after the grout sets. Accelerant percentage positively impacts early time signal attenuation, but after approximately 1 day the accelerate percentage does not significantly affect attenuation.

The high observed electrical conductivity of the grout is attributed to the high w/c of the mix. The sodium silicate adds to the conductivity during the gel phase, but then the conductivity appears to asymptote towards the conductivity of component A. Higher sodium silicate dosages create the highest conductivity at early gel times due to the high conductivity of sodium silicate in its individual form. However, the longer-term trend of the higher percentage sodium silicate resulting in lower total electrical conductivity is likely due to the higher dosage reacting with more free water and thus eliminating more free-mobile ions in the pore solution. The use of an alternative accelerant in aluminum-sulfate did induce lower conductivity and therefore would cause less GPR signal attenuation. However, the measured conductivity was still relatively high for GPR use and the skin depth remains on the order of inches. GPR may be best used at early set time with the aluminum sulfate accelerant since it reaches a minimum conductivity during the first hour.

In order to create an annulus grout material that can be penetrated by GPR, the component A would have to contain a significantly lower w/c or mobile ions would need to be neutralized. Therefore, a super plasticizer with a lower w/c ratio may be an alternative option. However, using sodium silicate may still influence the conductivity. Detailed electrical studies like the one presented here would need to be conducted on any new mixture because of the complex interaction of the different constituents.

Frequency effects of EM waves were not accounted for in this study. The DC conductivity provides a minimum possible value for attenuation. At certain frequencies, the effective conductivity may be significantly higher than what was observed here. However, understanding the DC conductivity is essential to fully understanding the results from a spectroscopy study which normally cannot separate out the DC conductivity contribution. Furthermore, the frequency effects are insignificant to GPR unless the DC conductivity is low enough to provide an attenuation constant with reasonable penetration depth.

4.3 Complex Dielectric Permittivity

Complex permittivity of the two-component grout was measured using a vector network analyzer (VNA) with an open-ended coaxial (OC) probe. This device produces an electro-magnetic wave pulse which is then reflected off the material surface where the stored energy and dielectric losses are recorded (Blackham and Pollard, 1997; Wu et al., 2000; Kaatze, 2010). The

response can be measured over a desired frequency spectrum to understand the frequency effects on complex permittivity. An equivalent circuit is used to measure the real and imaginary parts of the response, with the real part measuring the energy stored, or the effective permittivity, and the imaginary part measuring the energy lost, or the effective conductivity. Knowledge of a materials complex permittivity is crucial to evaluating the response in a GPR assessment since it provides the materials velocity, impedance, and intrinsic attenuation, as discussed in section 2.2.

4.3.1 Methods and Materials

A Keysight E5071C VNA with a frequency range between 300 kHz and 20 GHz was used, providing the range of frequencies for the anticipated GPR antenna used for the Rondout Tunnel Project. The VNA, shown in Figure 4.9, was calibrated with a three-part calibration using the open-water-short (OWS) method as described by Wu et al. (2000), Wagner et al. (2014), and Karlovšek et al. (2016), in order for the VNA to analytically solve for the equivalent circuit and output complex permittivity.

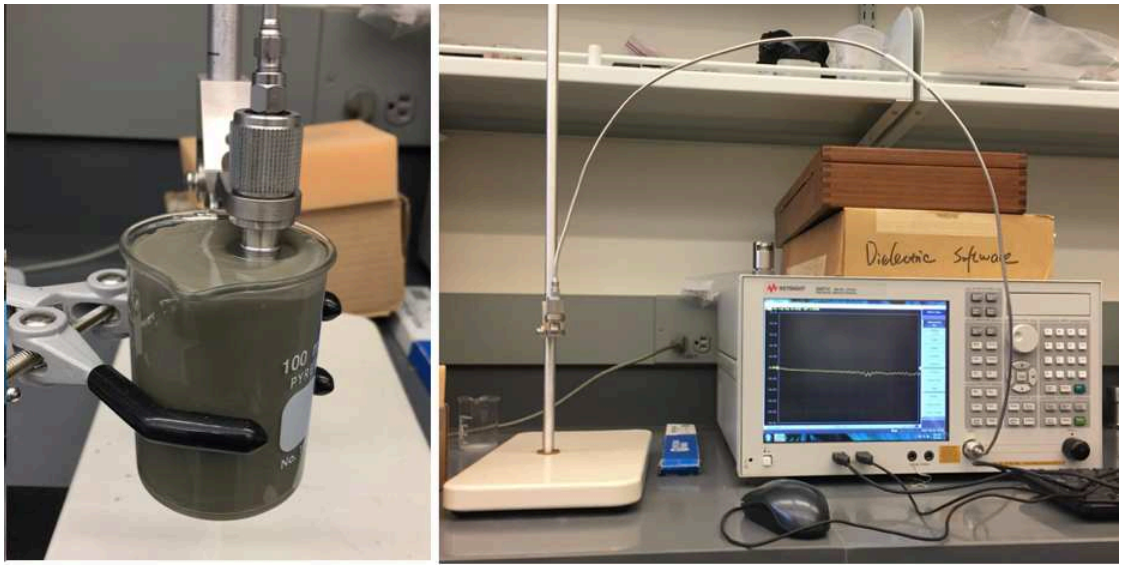

Figure 4.9 Photos of the VNA used for dielectric permittivity testing. (left) grout component A specimen with inserted OC probe; (right) VNA machine

Component A and B were tested individually in their fluid forms by inserting the OC probe directly into a beaker with the material, as shown in Figure 4.9. Accelerated cubic grout specimens were attempted to be tested with the methods described by Zhang et al., (2010) but

contact issues between the probe and specimen surface were encountered. These results are displayed in APPENDIX B.

4.3.2 Results

Complex permittivity results conducted on the components A and B individually are shown in Figure 4.10.

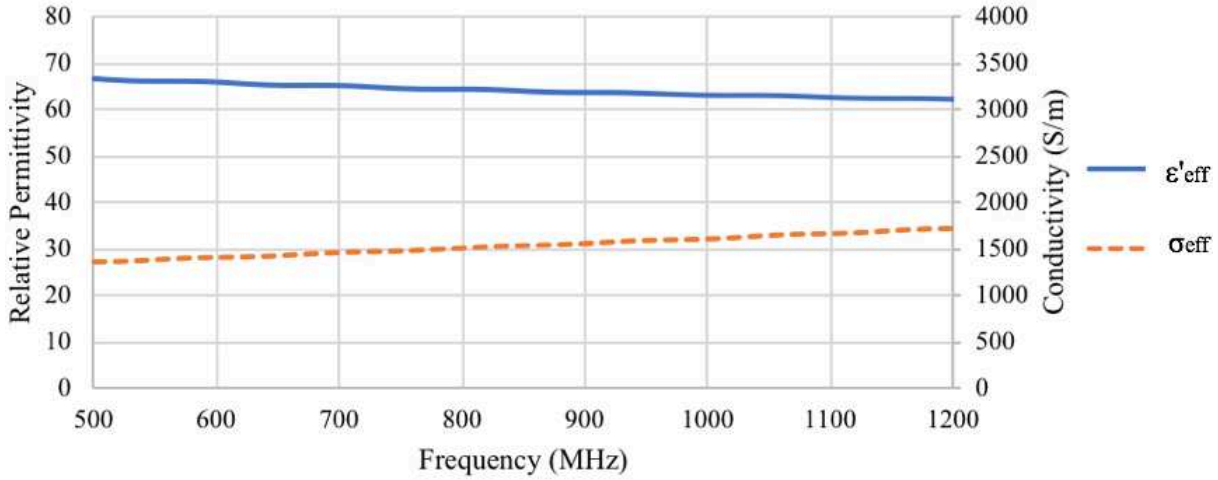

(a) Component A (Cement, Water, Bentonite, Retarder)

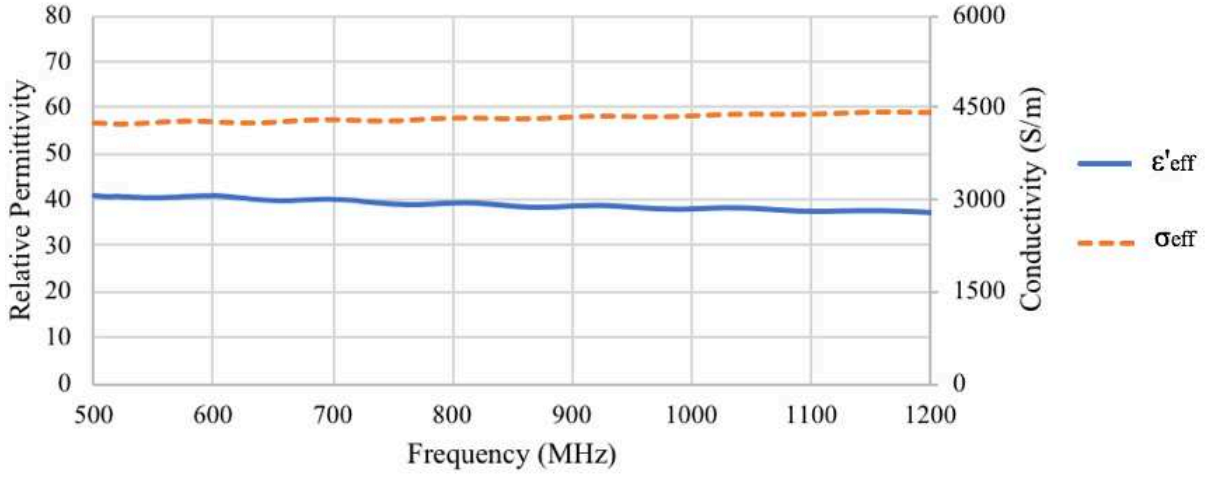

(b) Component B (Sodium Silicate)

Figure 4.10 Dielectric permittivity results from measurements performed (a) component A and (b) component B

Each component was in fluid form and allowed for the probe to be embedded into the material, thereby eliminating the contact issues encountered with hardened specimens. These values provide insight into the material component behavior, but fail to provide a value for the accelerated grout since the phase change has a large impact on permittivity. Due to the high water-content in component A, it is logical that the permittivity would be close to that of pure water (80).

The effective conductivity measured at 500 MHz for the component A of the grout is slightly higher than the DC conductivity values measured, which reveals the small comparative losses derived from frequency effects on the materials. It may be interpreted that the high DC conductivity dominates the losses of this material even after the grout gels and solidifies. The sodium silicate had more substantial frequency losses compared to that of component A when comparing the effective conductivity to the measured DC conductivity.

4.3.3 Dielectric Property Summary

Assumed electrical properties from literature review (Daniels, 2004) as well as properties indirectly observed from the actual GPR scans are shown in Table 4.1. The permittivity of the concrete segment was estimated from the results of the penetration tests, described in section 5.1.2.1, in order to match the two-way travel time through the segment. The anticipated conductivity of the grout was based on laboratory results from Karlovšek et al. (2016) for early set time, which were validated from the DC conductivity laboratory measurments conducted in this study. The high anticipated conductivity of the grout results in a skin depth of less than 2 cm. The electrical conductivity of the water was measured in a geotechnical study for the Rondout project. Radial resolution values displayed in Table 4.1 are absolute minimum theoretical values based on a 900 MHz central frequency antenna. However, as noted in section 2.2.5 , in reality the bandwidth of signals broadens when propagating through an attenuative material and therefore the actual radial resolution would be greater (worse) than that shown here.

Based on the impedances shown in Table 4.1, reflection coefficients at each possible material boundary were tabulated in Table 4.2. As discussed in section 2.2.4 reflection coefficients are dependent on which direction the EM wave is traveling when reaching the material boundary. This table can be used to evaluate the relative amplitudes for the reflected signals off different interfaces, with a coefficient of 1 being the greatest amount of reflected

energy. The square of the reflection coefficient is proportional to the amount of energy reflected at the interface (Daniels, 2004). As shown in Table 4.2, an EM wave traveling through air and reflecting off water would provide a coefficient of -0.80, which indicates a relatively large amount of energy is reflected with a phase-reversal for the returned signal. Whereas an EM wave traveling through water and reflecting off grout will provide a coefficient of 0.25, which indicates a relatively smaller amount of reflected energy and no phase reversal.

Table 4.1 EM properties of tunnel materials

Material	ε_{eff}	σ_T **(mS/m)**	v **(m/ns)**	δ **(cm)**	**|η|**	**2t (ns)**	**Δr (cm)**
Concrete	10	0.1	0.10	1.7×10^4	119	6.96[1]	2.05
Grout	62	4420	0.03	1.11	36.3	12.5[2]	0.71
Air	1	0	0.30	∞	377	1.35[2]	6.49
Water	81	55	0.03	86.8	41.9	12.2[2]	0.72
Gravel	2	0.1	0.17	9.2×10^3	218	-	-
Limestone	8	1	0.11	3.0×10^3	133	-	-

[1]Two-way travel time through 33 cm (13 in) (segment thickness)
[2]Two-way travel time through 20.3 cm (8 in) (annulus thickness)

Table 4.2 Reflection coefficients for materials in tunnel

		Material 2				
		Air	**Water**	**Concrete**	**Grout**	**Limestone**
Material 1	**Air**	0	-0.80	-0.63	-0.84	-0.48
	Water	0.80	0	0.48	0.25	0.52
	Concrete	0.63	-0.48	0	-0.58	0.06
	Grout	0.84	-0.25	0.58	0	0.62
	Limestone	0.48	-0.52	-0.06	-0.62	0

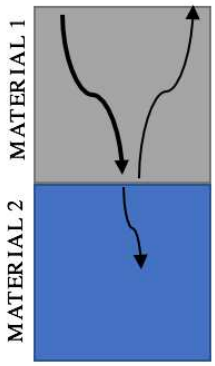

4.3.4 Discussion

Attempts to measure the complex permittivity with a VNA on cubic grout specimens provided inaccurate results due to improper contact between the specimen and probe. Contact issues are a common phenomenon when using a VNA. In order to combat contact issues, the probe should be embedded into the sample being measured (Karlovšek et al., 2016). Probes were unable to be embedded in this experiment since the OC probe provided is a specialized part that cannot be easily replaced if grout adheres to its surfaces. Use of a custom constructed OC probe would require a calibration kit to calibrate the VNA for each probe constructed which was not available. Additionally, false permittivity readings were occasionally encountered which likely necessitate an alternative calibration method than the OWS used.

The combination of values found from direct testing and values described in literature for common materials provided quantitative assessment for reflection coefficients and skin depths for materials within the tunnel. These values provide a basis of interpretation for GPR results to predict the strength and timing for the various types of reflections. Attenuation of the grout demonstrated that EM waves could not penetrate more than 2 cm into the grout material. Reflection coefficients between the segment and water compared to the segment and grout were very similar, indicating these materials would produce similar reflections. The segment-air boundary shows an opposite phase reflection compared to the water or grout boundary which would make it more easily identifiable at the immediate boundary reflection.

4.4 P-Wave Velocity

Seismic wave velocity measurements were conducted on the two-component grout to aide with Impact Echo assessment. As discussed in section 2.3, P-wave velocity is used to calculate travel time through a specimen as well as to calculate the impedance of a material. Impedance determines the amount of energy reflected at material interfaces. Knowledge of a materials impedance is essential to IE data interpretation in order to differentiate types of material boundaries.

4.4.1 Methods and Materials

Two-component grout was batched and formed into cubic mold specimens according to methods described in section 4.1. A total of 9 specimens were created from a single batch of

component A mix. Three sets of cubic molds were poured, each with the same accelerator dosage. One cube from each batch was continuously tested for two weeks, while two cubes from each batch were only tested once at 24 hours and 7 days to check how the velocity was affected by exposure to laboratory atmosphere while being tested at numerous time intervals.

A seismic imaging system was used for measuring P-wave velocity of the specimens. Cubes were weighed and the dimension between the signal source and receiver was measured before each test to calculate velocity and density and to check for moisture loss. Tape was first attached to the two grout-surfaces where the source and receiver were placed. Honey was then placed in between the taped surface and source/receiver probes with a rubber band to hold the probes in place. Figure 4.11 depicts the setup used for P-wave velocity measurements. A pulse-generator (Panametrics 5077PR) was used with 100V excitation magnitude with a repetition rate of 5 kHz and a gain of 10 dB. The transducers that were used for wave acquisition were broadband with a central frequency of 1 MHz. For more information about the experimental setup, please refer to the following references (Hedayat et al., 2012; 2013; 2014a-d; Hedayat and Walton, 2017; Shirole et al., 2017; Gheibi and Hedayat, 2018; Shirole et al., 2018). Visual inspection was performed to ensure the source and receiver were at the same height and aligned at the two sides of the specimen. Seven measurements were taken at each time interval per cube to ensure measurement repeatability and each wave measurement was an average of 50 waveforms stacked to maximize the signal to noise ratio.

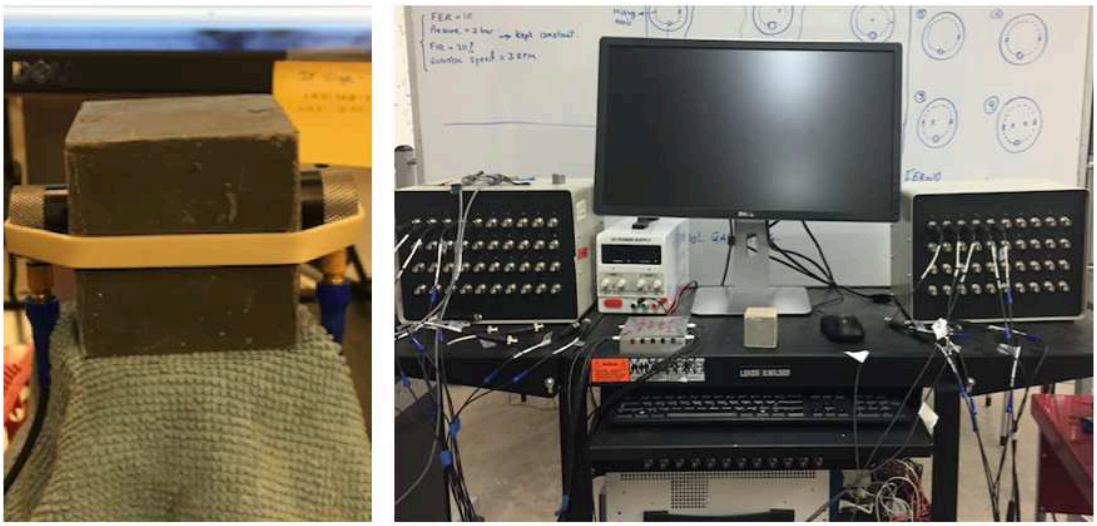

Figure 4.11 Photo of the seismic imaging system for P-wave velocity measurements. (left) source and receiver connected to grout specimen; (right) pulse generator system

4.4.2 Results

Averaged results from three specimens measured over a 14-day period at the same time intervals are displayed in Figure 4.12. The P-wave measurements match expected material behavior with quick velocity increase over the first 24 hours as the material gains strength through the gelling period, then velocity increases more gradually thereafter. The magnitude of results reported by Aggelis et al., (2008) was 1631 m/s, which is slightly less than the final hardened grout velocity measured in this study. This would be expected as this grout has a lower w/c ratio compared to the grout reported in that study. Grout velocity is significantly lower than the assumed segment velocity, shown in Table 4.3. This corresponds to the lower material strength and stiffness of the grout. Grout velocity beyond 14 days can be assumed to not vary significantly from the 14-day measurement of 1970 m/s.

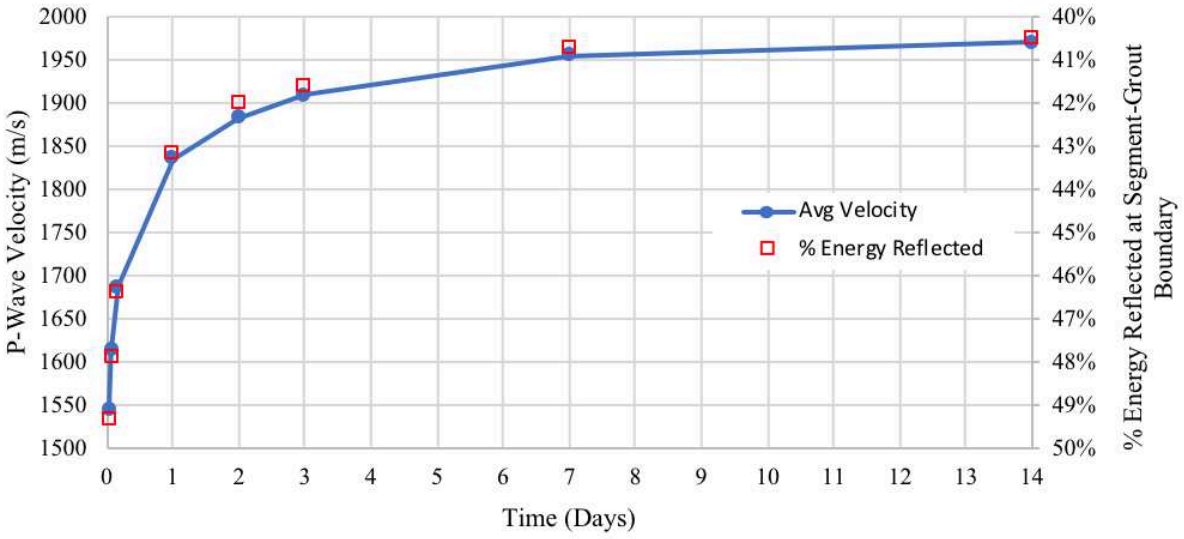

Figure 4.12 P-wave velocity results for three averaged grout specimens. Secondary axis represents the reflected energy between grout at that particular set time and the segmental liner based on impedance contrast between the segment and the grout.

The change in velocity corresponds to a change in impedance, as impedance is the product of velocity and density. Since the density of the material was measured, and not found to change significantly during curing, the impedance can be proportionally correlated to velocity. The percentage of energy reflected at the segment-grout boundary was plotted against set time as these values are changing with velocity. This plot demonstrates the decrease in energy reflected as the grout hardens which corresponds to a lower expected Q-value for IE.

4.4.3 Discussion

Changes in the grout velocity and impedance are significant in order to use IE to contrast grout at the segment interface from water. Table 4.3 shows the relative properties of the segment, grout, water, and limestone. The velocity of the segment was indirectly determined by the Impact Echo testing described in section 6.2, while the density was estimated based on its composition, compressive strength, and past projects (Aggelis et al., 2008). Grout properties change over set time due to the hydration of cement particles and change in internal structure, which is reflected by the range displayed.

When a seismic wave travelling through the segment reaches a water-interface, approximately 60% of the wave energy will be reflected. As the grout sets, the energy reflection contrast between a water boundary and a grout boundary becomes stronger, allowing for a better chance of distinguishing the material types using IE. If an air boundary exists at the segment interface, nearly 100% of the energy would be reflected, since the impedance of air allows for very little energy to pass through the boundary. This creates the strong resonant frequency that the impact echo method utilizes. The differentiation of impact echo response based on the impedance contrast of grout and water is further discussed in section 6.2 where field data is presented. These laboratory studies provided the basis to understand the field implantation results.

Table 4.3 Elastic properties for materials within the Tunnel (Bourbie et al., 1987; Aggelis et al., 2008)

Material	Velocity (m/s)	Density (g/cm^3)	Impedance ($kg*m^{-2}*s^{-1}$)
Segment	4554	2.50	$1.15x10^7$
Grout	1545 - 1955	1.31	$2.02x10^6 – 2.55x10^6$
Water	1500	1.00	$1.50x10^6$
Limestone	3500 - 6000	2.4 – 2.7	$8.40x10^6 – 1.62x10^7$

CHAPTER 5
GPR CALIBRATION EXPERIMENTS

Experiments using segments molded for the Rondout bypass tunnel were conducted to select the most appropriate GPR equipment for imaging beneath the segment and calibrate the filter settings for the highest resolution void detection possible. These experiments included the use of multiple frequency antennas, two-component grout, and simulated water and air voids. EM properties of the grout and segment were indirectly measured through these experiments as well as the penetration ability for the various signal frequencies. Two experiments were separately conducted, the initial one on the Colorado School of Mines (CSM) campus, described herein as the CSM experiment, and a secondary experiment conducted on the Rondout Bypass Tunnel site, described herein as the Rondout Experiment. Numerical modeling was used in conjunction with field experiments to support the GPR results interpretation and to validate the expected EM material properties.

5.1 CSM Mock Liner Experiment

Experiments performed on the CSM campus were initially conducted to determine the frequency penetration capabilities for various GPR antennae with different frequencies as well as to validate their ability to differentiate water or air voids compared to a fully grouted annulus space. A segment from the Rondout project supplier was shipped to campus and tested. Grout was injected into compartments underneath the segment containing fabricated mock-voids. Various antennas were tested, ranging from 400 MHz to 2.4 GHz using both MALA and GSSI equipment. The selected frequency range was based on anticipated permittivity of the materials being scanned, and literature review of past projects (Parkinson and Ékes, 2008; Zhang et al., 2010; Lalagüe et al., 2016; Yu et al., 2016).

Three scenarios were chosen to most accurately represent possible field conditions. The first is a perfectly filled annulus space with grout. This is the baseline condition that void scans can be compared against. The second represents complete grout washout leaving an air or water void that fully fills the depth of the annulus space. The third condition is partial washout of grout with a void beneath a thin layer of grout. A 5” diameter plastic pipe with a thin cover of grout beneath the segment, which was interchangeably filled with air and water, was installed within a

grouted compartment. Results from these experiments helped determine the EM wave velocity and attenuation coefficients for the segment and grout.

5.1.1 Materials and Equipment

In order to re-create conditions simulating the expected environment in the tunnel, a pre-cast segment was obtained and two-component grout was mixed and injected into fabricated spaces underneath the segment. A range of GPR equipment was obtained for determination of the most appropriate frequencies for this application. In order to inject the two-component grout, separate pumps were required and a specially fabricated Y-connection was built to simulate conditions in the TBM.

5.1.1.1 Pre-cast Segment

A pre-cast concrete segment formed from the same concrete and mold-cast used for the Rondout production segments was tested. Segment dimensions are specified in section 3.2. The rebar cage was slightly modified from the actual design. A double layer rebar cage with similar rebar spacing was provided but missing some of the cross supports on the ends of the segment. An image of the rebar cage inside the formed tested segment is displayed in Figure 5.1. The rebar cage pictures can be compared to the rebar cage design for the actual segments shown in APPENDIX A.

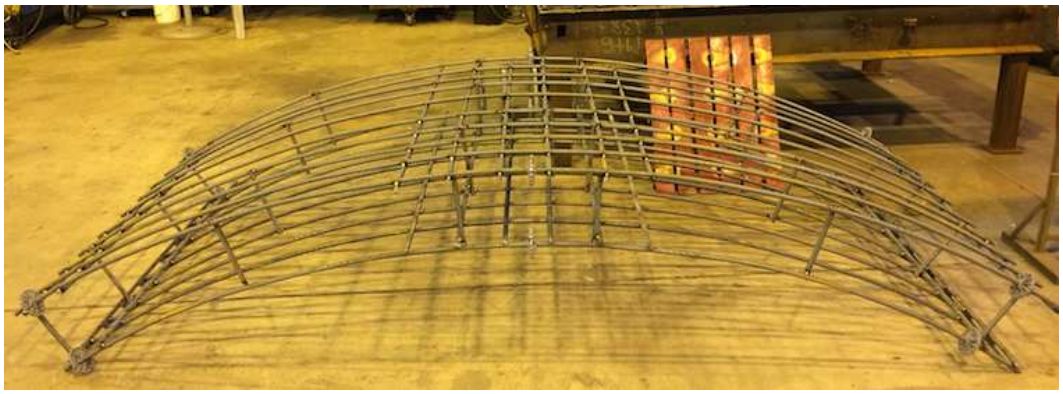

Figure 5.1 Rebar cage used inside segments tested during the CSM Experiment

5.1.1.2 Support Frame

A wooden support frame was constructed to elevate the segment off the ground and create mock-void and grouted compartments underneath the segment. Figure 5.2 shows the void compartment design for the CSM experiment.

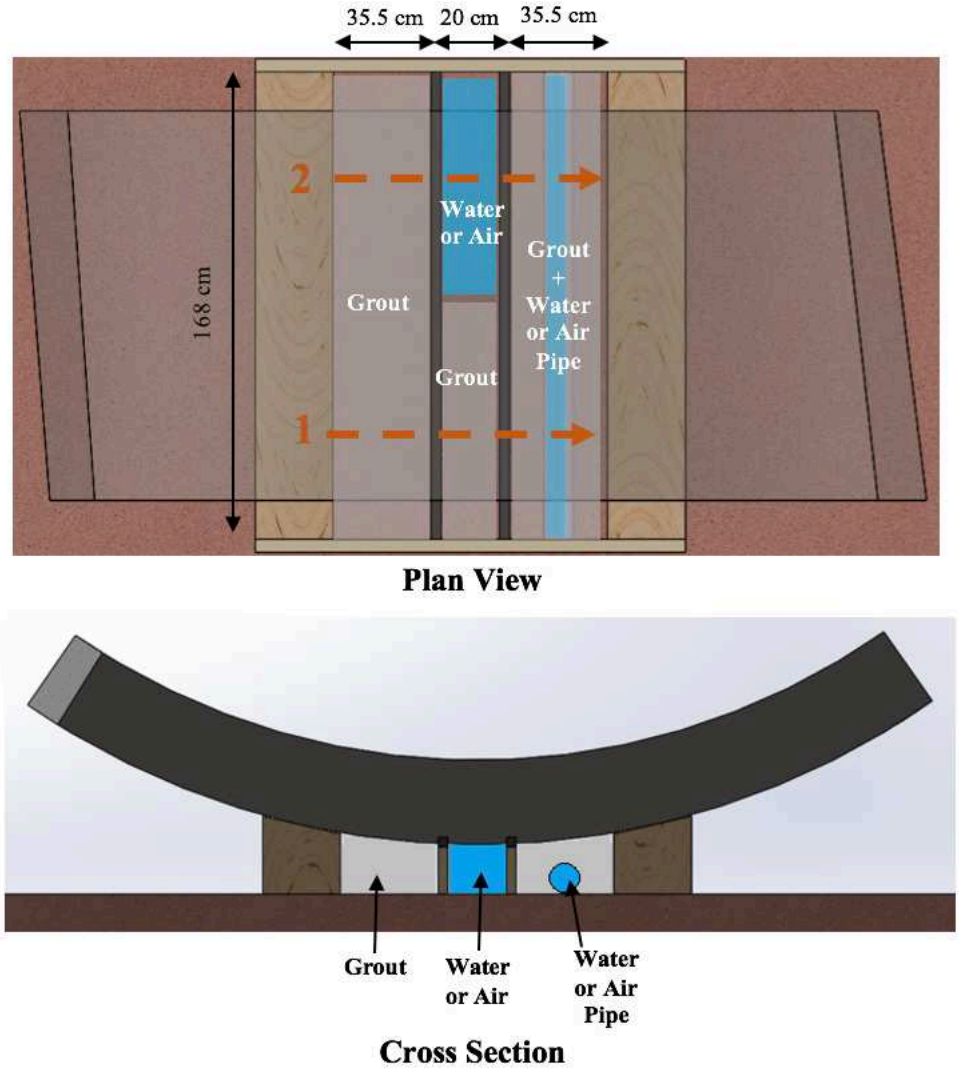

Figure 5.2 Void compartment design for CSM experiment. GPR scan lines shown in orange

Wooden timbers with nominal 12x12 inch dimensions were placed under the two curved ends of the segment to provide the main support. The timbers were cut at a 12.7-degree angle, approximating the curvature of the segment at that location. Wooden beams were connected to the timbers to provide lateral bracing support as well as to contain the grout. Two additional

beams were placed in the center of the segment to create a total of three compartments for grout injection and mock void space. Foam blocks were placed on top of these central wood beams to ensure good contact was made between the wood and the segment so that grout could be contained in the compartments upon injection. The center void compartment was further divided in half to create scan lines with a fully grouted annulus (scan line 1) compared to one with a water or air void (scan line 2).

The center void was designed to be the minimum resolvable width (19.8 cm) of the lowest frequency antenna used (400 MHz). The pipe embedded within the grout had a total diameter of 14 cm which meant its width could be resolved with the 800 MHz antenna. GPR can detect smaller objects than this minimum, but the width cannot be resolved from the radargrams. The total width used beneath the segment was designed to be the largest width possible with the 12x12 timber supports while maintaining a 20 cm height above the ground for the center void, simulating the annulus gap thickness. The total designed grouting volume was the maximum volume possible with the grout pumps available at the time of the experiment.

5.1.1.3 Grout Pumps

Due to the quick-forming nature of the grout, individual injection pumps were required for each component emulating the pumps on the Rondout TBM. A CG-550 Workhorse Series pump was used for the component A grout and an A20 Peristaltic accelerant dosing pump from Putzmeister was used for the sodium silicate, both of which are shown in Figure 5.3.

Figure 5.3 Photos of the pumps used for the CSM experiment. (Left) CG-550 pump for component A; (Middle) Putzmeister peristaltic dosing pump for accelerant; (Right) Wye connection for combing the two components upon injection

The two output hoses from the pumps were connected with a wye-connection and the grout was ejected out a 1.8 m (6 ft) steel pipe.

5.1.1.4 Grout

The two-component grout used for the experiment is the same as described in section 3.3, with the addition of fly ash as it was still a part of the grout design at the time this experiment was conducted. Grout component A was pre-mixed with the Jiffler drill attachment, as described in section 4.1, and then poured into the paddle mixer on the CG-550 pump.

5.1.1.5 GPR Equipment and Filter Settings

GPR equipment was provided from MALA Geoscience and GSSI in order to test a wide array of antenna frequencies. The antenna sizes tested ranged from 400 MHz to 2.6 GHz. MALA supplied a high frequency module with 1.2, 1.6, and 2.6 GHz antenna along with a Pro-Ex control unit and an 800 MHz antenna. GSSI supplied a SIR 4000 control unit with 400 and 900 MHz frequency antenna as well as Mini 1600 MHz control unit and antenna. The antennae that were tested are displayed in Figure 5.4.

Figure 5.4 GPR equipment used in CSM Experiment (a) MALA 2.3 GHz antenna; (b) MALA 1.6 GHz antenna; (c) MALA 1.2 GHz antenna; (d) MALA 900 MHz antenna; (e) GSSI 900 (near) & 400 MHz (far) antennas; (f) GSSI SIR 4000 control unit (g) MALA control unit

Filter settings used for the final radargrams were determined experimentally after data was collected. The ultimate goal of the radargrams was to be able to visually identify the reflection of the segment-annulus material boundary and the reflection of the annulus material-rock boundary. Therefore, the rebar cage reflections in the segment were not significant for annulus grout detection. Three types of filter settings were necessary to accomplish these goals. The first was a time zero setting that was automatically applied with the GPR equipment to enable accurate time measurements of the reflected wavelets. The second was an exponential gain filter to increase the signal amplitude at greater times, shown in Table 5.1. Attenuation causes reflections at greater penetration depths to be less visible compared to shallow reflections, such as the rebar. Manual adjustment of the exponential gain points was performed to help illuminate the reflection band beneath the segment while diminishing the rebar reflections. The third was an infinite impulse response bandpass filter to eliminate high and low frequency signals, shown in Table 5.1. Reflections beneath the segment were not apparent without an applied bandpass filter due to the broadband frequencies induced as the EM wave pulse is transmitted.

Table 5.1 GPR Filter Settings

Filter	**Value**
Gain Mode	Manual
# Gain Points	8
Gain Points	-20
	10
	50
	50
	50
	50
	51
	51
IIR Low Pass	1500
IIR High Pass	500

5.1.2 Experimental Procedures and Results

Before grout injection, penetration tests were performed on the segment with the various antennae to determine which frequencies could image beneath the segment. Grout was then injected into the compartments underneath the segment in two separate events. The primary injection used the grout pumps described above, while the secondary injection used a gravity pour system. Void detection testing was then performed to observe the signatures for water and air voids, determine the most appropriate GPR post-processing filters, and indirectly analyze the EM properties of the grout. Procedures and results are described in detail below.

5.1.2.1 Penetration Testing

GPR penetration tests were performed by moving the GPR antenna across the segment intrados with a steel plate held in contact with the segment extrados. The steel plate was held flush against the segment directly beneath the GPR scan line, as depicted in Figure 5.5. Each of the antennas described above was tested to see if the steel plate was apparent in the GPR scans. Resolved radar grams were compared to numerical model simulations to further validate the results and help resolve the effective velocity through the segment.

Figure 5.5 Picture of the segment on top of support frame used for penetration depth testing

GPR radargram results from the field penetration tests through the segment are displayed in Figure 5.6. These radargrams are visual representations of hundreds of individual EM wavelets combined to create a 2-D rendering. The vertical axis is displayed in time units demonstrating the two-way travel time of a reflected EM wave received by the GPR unit, and the horizontal axis is real distance along the scan-line. White bands represent peaks of returned signals and black represents troughs. In other radargrams of this report, blue is used to indicate peaks and red used to indicate troughs. Filters were applied to the data sets in order to aid interpretation including time zero, bandpass, and time-gain filters. Deconvolution and background noise removal were not found to have positive impacts on data assessment and were therefore not used.

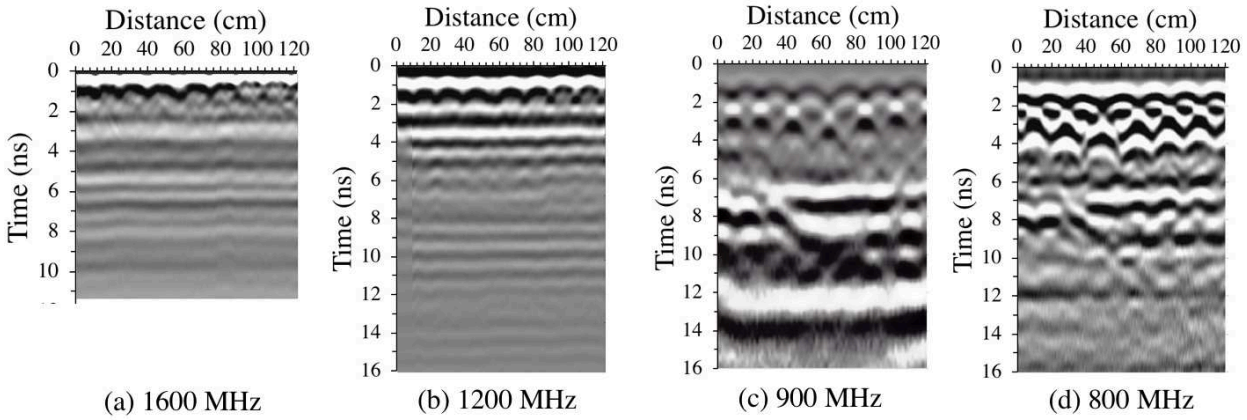

Figure 5.6 Radargrams from four selected antennas on the steel plate penetration test. (a) 1600 MHz antenna; (b) 1200 MHz antenna; (c) 900 MHz antenna; and (d) 800 MHz antenna

Radargrams provide a basis of interpretation to demonstrate GPR results along the scan line. The depth of rebar and the steel plate beneath the segment can be visually identified by the reflections shown at specific times. Six to seven parabolas are evident at approximately 1 ns on each of the radargrams and can be interpreted as the primary steel rebar layer in the segment. Point reflectors in a GPR scan appear as parabolas because as the GPR antenna moves towards or away from the point reflector, some of the spreading wave front will reflect off the point but be returned to the receiver at a later time. Shadowing effects, caused by the inability of an EM wave to propagate through steel, masks the second layer of rebar directly beneath. Additionally,

wave fronts have the ability to combine with one another which can create an interference pattern, observable as the bright white spots between 2-3 ns on the 900 MHz radargram.

The steel plate reflections and adjacent air reflection appears at approximately 7-9 ns on the 900 and 800 MHz radargrams in Figure 5.6. The steel plate reflection tapers off as the antenna is moved away from the plate and on top of air due to the same effect that generates the parabolic reflection from steel rebar. Reflections beneath the segment display a slight wavy nature which can be attributed to shadowing and refraction effects from the EM wave passing through the steel rebar cage. The phase reversal is evident for the steel plate as demonstrated by a slight time-offset in the reflection bands. The reflection time of the steel plate is a two-way travel time, therefore the effective EM wave velocity through the segment can be determined from half that time divided by the segment thickness. This resulted in an apparent velocity of ~0.1 m/ns. GPR antenna with frequencies above 900 MHz did not did not demonstrate clear ability to penetrate through the segment and receive reflected signals.

Other linear features displayed in the radargrams may be interpreted as background noise. Means of noise reduction are possible through background removal filters but these tend to also eliminate the air and steel plate reflections. Background noise is common in most radargrams at times greater than when the original EM pulse has attenuated (Alani and Tosti, 2018).

Numerical modeling was used to aide in interpretation of the GPR scan results using GPRMax open source software. This software solves Maxwell's equations in 3D using a Finite-Difference Time-Domain (FDTD) algorithm (Warren et al., 2016). Modeling the GPR setup provided additional support for radargram interpretation. Model parameters included a maximum discretization at least ten times smaller than the shortest expected wavelength (based on material permittivity and selected frequency), and beginning the simulated scans at least 15 cells from the boundary in order to minimize effects of the software absorbing boundary conditions (Warren et al., 2016).

Models provide an example of the steel plate reflection if the signal were to pass through the segment. These models are unable to predict segment penetration without prior knowledge of the segment's electrical conductivity. Furthermore, additional signal attenuation is caused by scattering from in-homogeneities within the segment that cannot be captured in the model. The model displayed in Figure 5.7 features a 900 MHz frequency antenna with receiver spacing of 15 cm, matching that of the 900 MHz antenna used. An effective permittivity of 10 was used for the

segment, which was chosen to match the field results for reflection time of the steel plate. This permittivity is within the high end of the concrete permittivity spectrum found in the literature (6-12) due to the high strength concrete used and the effects of the rebar cage refracting the signal. An assumed electrical conductivity of 0.1 mS/m was used matching values found in the literature (Daniels, 2004; Zhang et al., 2010) since conductivity testing was not be conducted directly on the segment. Rebar was not input in the modeled segment in order to simplify the results for demonstration of the expected wave-phase arrivals and steel plate reflection shape.

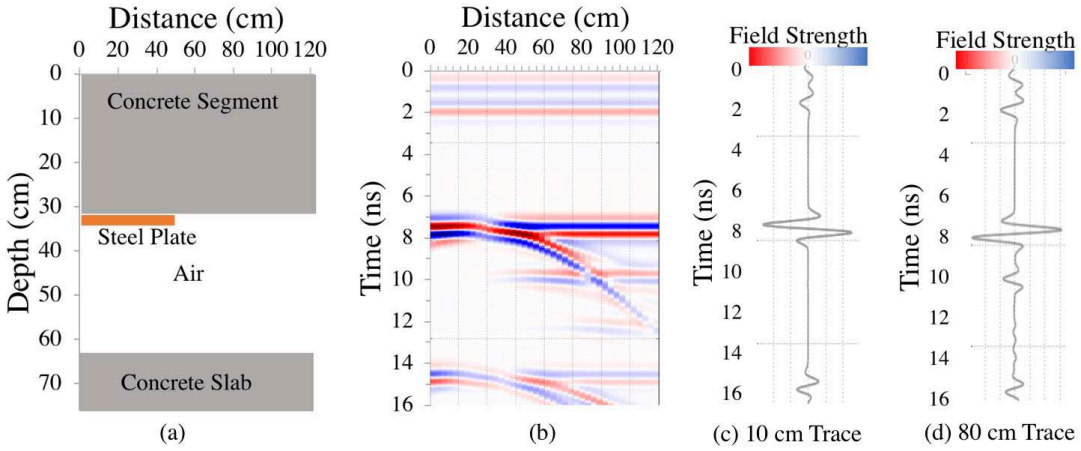

Figure 5.7 900 MHz numerical model (a) Geometry of model (b) GPRMax radargram results; (c) single trace at a distance of 10 cm, reflection off steel; (d) single trace at a distance of 80 cm, reflection off air

The numerical model in Figure 5.7 displays direct waves from the transmitter to the receiver as the initial horizontal color bands between 0 to 2 ns. Direct waves are not displayed in the actual radargrams due to the processing filters used. The numerical model demonstrates two key features from the steel plate. The first feature is a phase reversal of the original wavelet from the reflection off steel compared to the in-phase reflection caused by air. This phase reversal can be identified by the reverse coloring of the reflection band between 7 to 8 ns on the left side versus the right side of the radargram in Figure 5.7b. Single traces of EM wavelets are plotted in Figure 5.7 c-d demonstrating the phase reversal of wavelets between reflections off steel versus air, respectively. Phase reversal can sometimes be identified in the actual radargram results by an apparent time offset in the reflection bands when signal background noise is prominent. The second key feature identifying the plate is the parabolic reflection shape of the steel plate as the

GPR antenna moves away from the plate and directly over air. The shape of the steel plate reflection demonstrated in this numerical model matches the field results for the 900 and 800 MHz scans, while no such feature is visible in the higher frequency scan lines.

A numerical model with steel rebar modeled inside the segment is shown in Figure 5.8. The numerical model results display the interference patterns created by the steel rebar cage. The shallowest rebar, embedded approximately 3 cm within the segment, creates the parabolic interference pattern between 2 and 4 ns on the numerical model. This is consistent with GPR radargrams taken on the segment. The deepest rebar, embedded approximately 30 cm in the segment, creates an interference pattern which arrives at approximately 6 ns, just before the arrival of the wave reflection off the material beneath the segment (7-9 ns). This secondary interference pattern makes the steel and air reflections challenging to discern on the numerical model. Results are consistent with field radargrams that demonstrate bright reflection bands arriving just before the reflection bands of the material behind the segment.

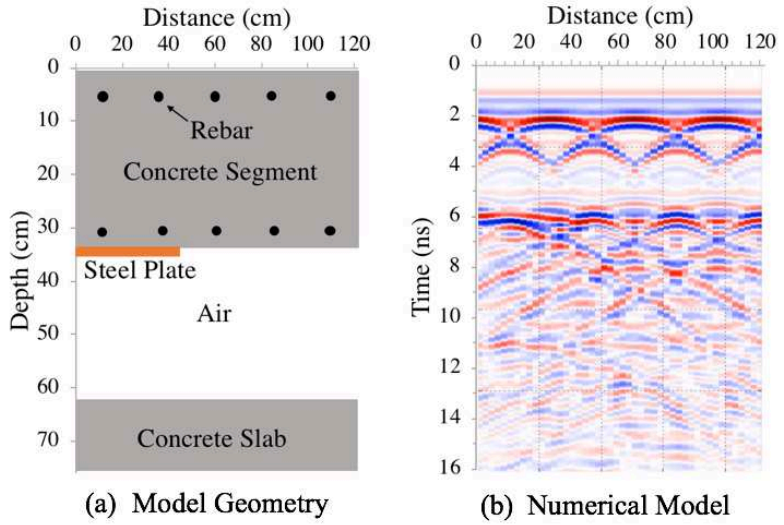

Figure 5.8 900 MHz numerical model of the penetration test with rebar in the segment

Due to the added complexity that modeling the rebar creates, steel rebar in the segment was left out of the numerical models for the remainder of this study. The numerical models are intended to help identify reflections for different materials within the field radargrams, which is best achieved by eliminating the additional interference patterns created by the rebar in the models.

5.1.2.2 Void Detection Testing

The ingredients for component A of the grout were measured and mixed in 15 L (4 Gal) batches in order to make a total of 318 L (84 Gal). Due to the unavailability of a mobilized colloidal mixer at the time of testing, Component A was mixed with a Jiffler power-drill attachment prior to being poured into the grout-paddle mixer. The drill attachment simulates shearing experienced in the colloidal mixer on the TBM. The grout paddle-mixer could hold 151 L (40 Gal) at a time. The left and right compartments were pumped with grout separately due to the limitation of the paddle mixer volume. The grout pump was turned on first, followed by the dosing pump. Once accelerated grout was observed to be flowing, the pipe was inserted into the grouting compartment and filling was observed from the 15 cm gap along the segment widths, Grout was observed to fill up the end of the compartment to a height greater than the bottom of the segment before being pulled out of the compartment. The open areas on the ends of the segment were covered with plastic sheets to help enable proper curing of the grout. The center grout compartment was filled separately by mixing the two components together and then pouring the grout into the compartment in lifts. Water was filled into the central void compartment and void tube before designated water scan lines.

Following the primary grout filling, GPR scans using MALA and GSSI equipment were run along the scan lines depicted in Figure 5.2. After determining the lack of penetration ability from antenna frequencies above 900 MHz, only the 900, 800 MHz and 400 MHz antenna were used for the void detection. GPR scans were collected at regular time intervals until a 3-week cure time to determine how the EM properties changed with set time. Before each scanning period, temperature measurements were taken of the water in the central compartment and on the surface of the grout with a temperature gun. Each GPR antenna used an encoder wheel to measure distance along the scan-line and emit GPR pulses at regular spacing.

Results from the void detection tests for the 900 MHz antenna are shown in Figure 5.9 alongside the scan line geometry and numerical model results. There are two models presented for each scan line demonstrating two possible grout electrical conductivity values. The intent in displaying two conductivity values is to demonstrate radargram results for a grout with a high electrical conductivity of 4500 mS/m, which is believed to be the actual effective conductivity, compared to what the radargram would look like if the grout had a low conductivity. Demonstrating what the reflection would look like if the EM wave were to fully penetrate the

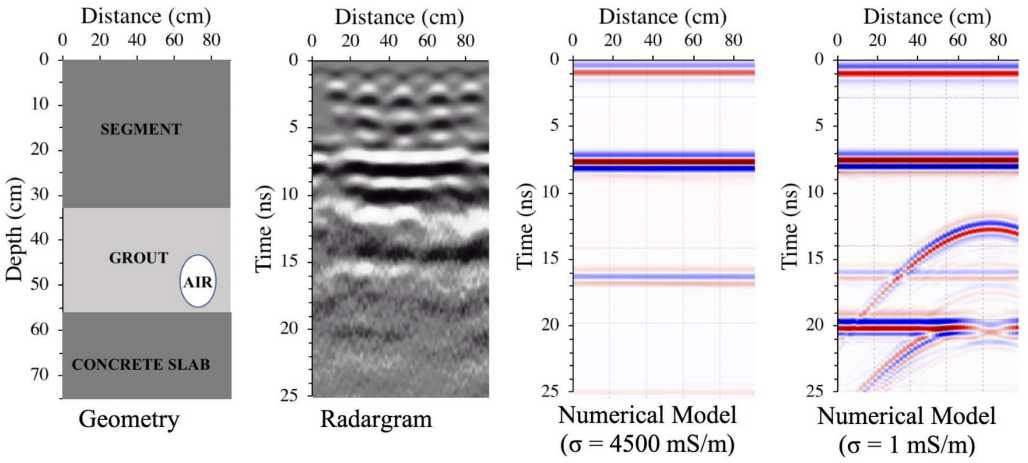

(a) – Scan line 1 (Full Grout)

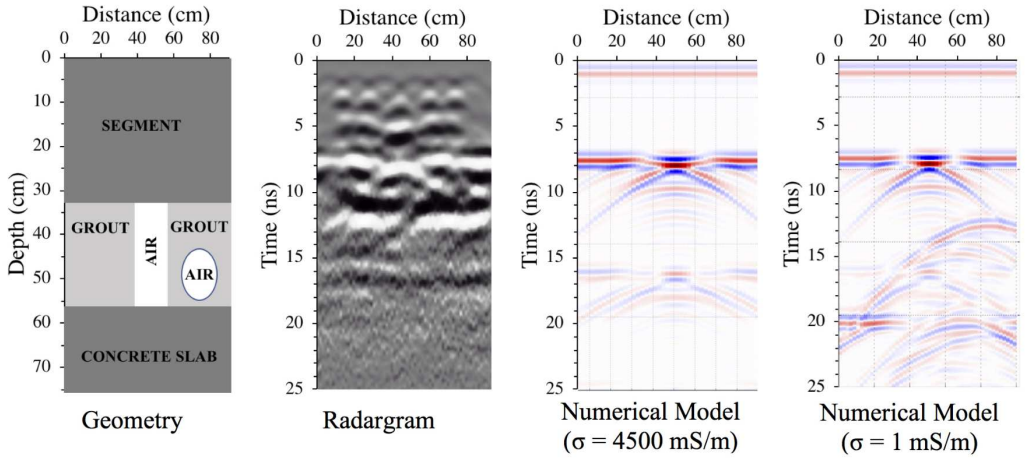

(b) – Scan line 2 (Air Void)

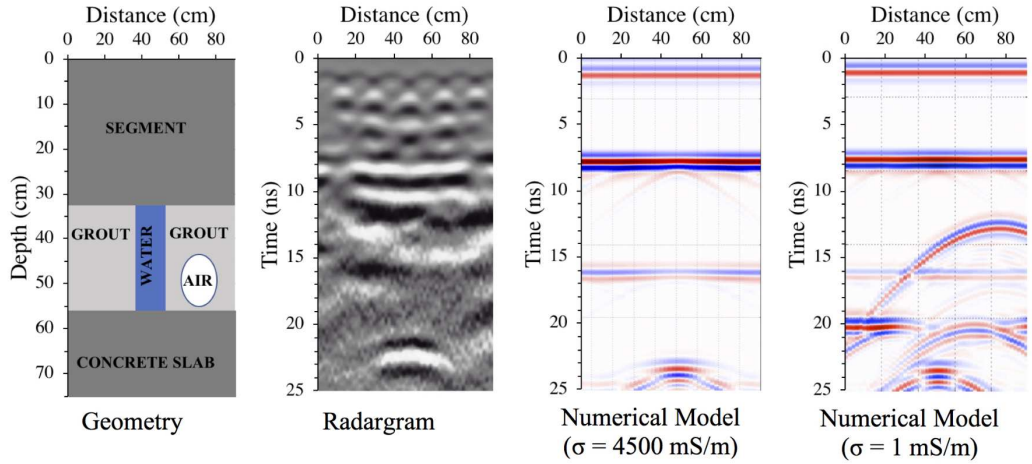

(c) – Scan Line 2 (Water Void)

Figure 5.9 Void detection results demonstrating the scan line geometry, actual radargrams, and two numerical models with different plausible electrical conductivity values (a) scan line 1 with all grout; (b) scan line 2 with air in the center compartment and; (c) scan line 2 with water in the center compartment

grout with a low conductivity is necessary to eliminate interpretation errors that can occur when there is uncertainty whether a received EM wavelet is due to a true reflection, a duplicate caused by ringing, or simply background noise. This distinction is crucial to help eliminate false identification of radargram features.

Figure 5.9a demonstrates a fully grouted scan line. The radargram displays reflections off of the rebar cage as parabolic reflections at approximately 3 ns. As described in the penetration test results, the second layer of rebar cannot be clearly identified due to shadowing from the first row. Several bright horizontal reflection bands appear between 7 to 9 ns which have been interpreted as the segment-grout interface reflection. While a standard reflection will typically appear as a triplet of wave fronts (negative-positive-negative, or positive-negative-positive), the addition of duplicate reflections and background noise can add to the number of received wave fronts at any specific time. Therefore, the segment-grout reflection is not a perfect triplet but contains additional noise likely due to the rebar interference pattern. This is supported by comparison to the numerical model which does not contain rebar interference. A secondary reflection appears at approximately 15 to 16 ns which has been interpreted as a duplicate of the primary grout reflection. The high conductivity numerical model also displays this reflection band at approximately 16 ns where the known skin depth is less than the grout thickness. The numerical model with low conductivity displays a bright horizontal reflection band at approximately 20 ns which is the grout-concrete reflection. Radargram results from the field also indicated no true reflection off the air pipe buried beneath grout. Comparison with the low conductivity numerical model displays a parabolic reflection feature with a peak at approximately 12 ns and 75 cm into the scan line which can be confidently interpreted as the air pipe reflection.

Scan line 2 with air in the center compartment is displayed in Figure 5.9b. The radargram displays clear evidence of the air void reflection at the immediate segment-annulus boundary. The air void is determined by the phase-shift relative to the grout reflection band that creates an inverse of reflected wave amplitudes at the same time intervals. Due to the relatively small air void depth relative to the EM wavelength, the bottom of the air void cannot be determined by these results. The secondary reflection at the bottom of the air void-concrete boundary interferes with the primary reflection because of the high EM wave velocity in air. Based on the EM wave

velocity displayed in Table 4.1, the two-way travel time through the air void thickness is less than 2 ns which is shorter than the duration of a single wavelet to be received.

Scan line 2 with water displayed in Figure 5.9c also demonstrated clear ability for the GPR to detect complete washout of the annulus grout leaving behind a water void. The primary reflection at the segment-grout boundary is non-distinct from the segment-water boundary. This result coincides with the calculated reflection coefficients in Table 4.2 which demonstrate the small impedance contrast between water and grout. However, unlike the grout which has a skin depth of less than 2 in, the EM wave travels through the full depth of the water void with little attenuation and reflects off the water-concrete interface. This secondary water void reflection between 22 to 24 ns creates a distinct signature when compared to the fully-grouted annulus space.

5.1.2.3 Grout Set Time Effects

GPR scans were conducted over scanline 1 with water filled in the buried pipe at discrete times. The geometry of the scan line is the same as Figure 5.9a but with water in the pipe. The results from measurements taken at 1 hr, 24 hr, and 4 day set time are displayed in Figure 5.10a-c alongside a numerical model for the same scan line with a low grout conductivity. This numerical model can be used as a baseline to determine if the conductivity of the grout becomes low enough to identify the features created by the water filled pipe.

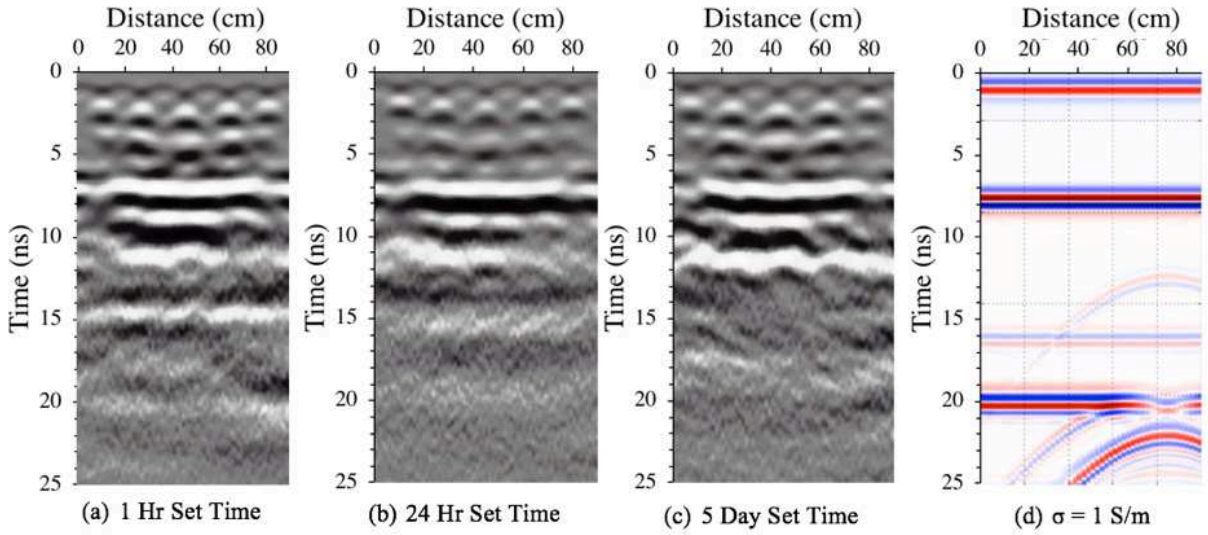

Figure 5.10 (a-c) Radargrams for grout with various set time along scan line 1 with water filled in the tube; (d) low conductivity numerical model of scan line 1 with a water filled tube

As demonstrated by the numerical model in Figure 5.10d, with the grout conductivity low enough to allow for penetration of the EM signal through the 10 cm grout thickness above the pipe, a parabolic reflection at the grout-water interface would appear at approximately 12 ns, and a secondary reflection at the bottom of the water pipe would appear at approximately 21 ns. The primary reflection at the grout-water interface is weaker than the reflection at the water-concrete interface due to the larger dielectric contrast between water and concrete.

On the radargram results, a slight parabolic feature does appear slightly visible at 10 ns, but no secondary reflection is apparent at 21 ns. The lack of a secondary feature suggests that the EM signal is not fully penetrating the grout thickness even after four-day cure time. Therefore, the curing time of the grout did not impact the penetration depth of the GPR to allow for confident detection of the buried water void.

5.1.3 Discussion

The CSM mock liner experiment produced valuable insight into EM properties of the segment and the grout. Penetration results indicated that 900 MHz was the highest frequency to fully penetrate the segment and would therefore have the greatest resolution for void detection. Additionally, the segment velocity was estimated directly from this experiment which enables prediction of the annulus material reflection timing in the field. A permittivity of 10, deduced from the velocity, is on the higher end for concrete likely due to the high-strength concrete material used. Mock-void detection demonstrated clear ability to differentiate between grout at the segment-annulus interface compared to air or water. Air voids can be differentiated based on the relative phase-shift of the primary reflection, whereas water voids are differentiated by the secondary reflection at the bottom of the water void. Results matched the numerical models well which indicates the assumed dielectric permittivity and effective conductivity are within the correct range for the segment and grout. Inability to detect a water or air-filled pipe buried 10 cm within the grout after 4 day set time further supports the high effective conductivity of the grout determined in the laboratory testing.

These results proved the GPR effective in detecting complete washout of the annulus grout material on a one-meter scale. The ability to differentiate larger regions of grout washout was still requested by the contractor and owner's engineers before adapting the GPR technique for field use. Furthermore, additional evidence for the GPR skin depth in grout after longer set

time was required to determine whether or not the GPR could detect a void buried beneath a thin skin of grout at the segment extrados interface. These remaining questions led to the development of a secondary mock-liner experiment conducted on the Rondout project site.

5.2 Rondout Mock Liner Experiment

A secondary mock-liner experiment was conducted using two pre-cast segments supported on specially designed wooden frames on the Rondout project site. Compartments under the segment were backfilled with grout, water or air to simulate different possible scenarios. Objectives for this experiment were to build upon results gathered from the CSM mock liner experiment in order to demonstrate the key GPR signatures for larger voids and provide additional evidence for the abilities of the GPR to detect a void beneath a thin layer of grout. Conducting this secondary experiment on the Rondout project site allowed for the contractor field engineers and the owner's engineers to observe the use of GPR in real time.

5.2.1 Materials

The Rondout experiment used two-component grout batched on the project site using the TBM colloidal mixer. Two production segments were supplied for complete simulation of the segments installed in the tunnel. Segments were supported on constructed wooden frames and grout was pumped underneath the segment and contained within the support frame.

5.2.1.1 Support Frames

Wooden support frames were constructed to elevate the segments off the ground and create four sealed compartments. Gravel was spread inside the frames at the approximate curvature of the TBM rock cut and covered with plastic sheeting to ensure grout did not seep into the gravel and mask the grout-gravel boundary. Two separate frames were built, as shown in Figure 5.11a and b, to allow for a total of four different scan lines. The void spaces could be left empty with air or filled with water to demonstrate the different void signature types. Scan lines are depicted in Figure 5.11a and b as the orange dashed lines labeled A1, A2, B1, and B2.

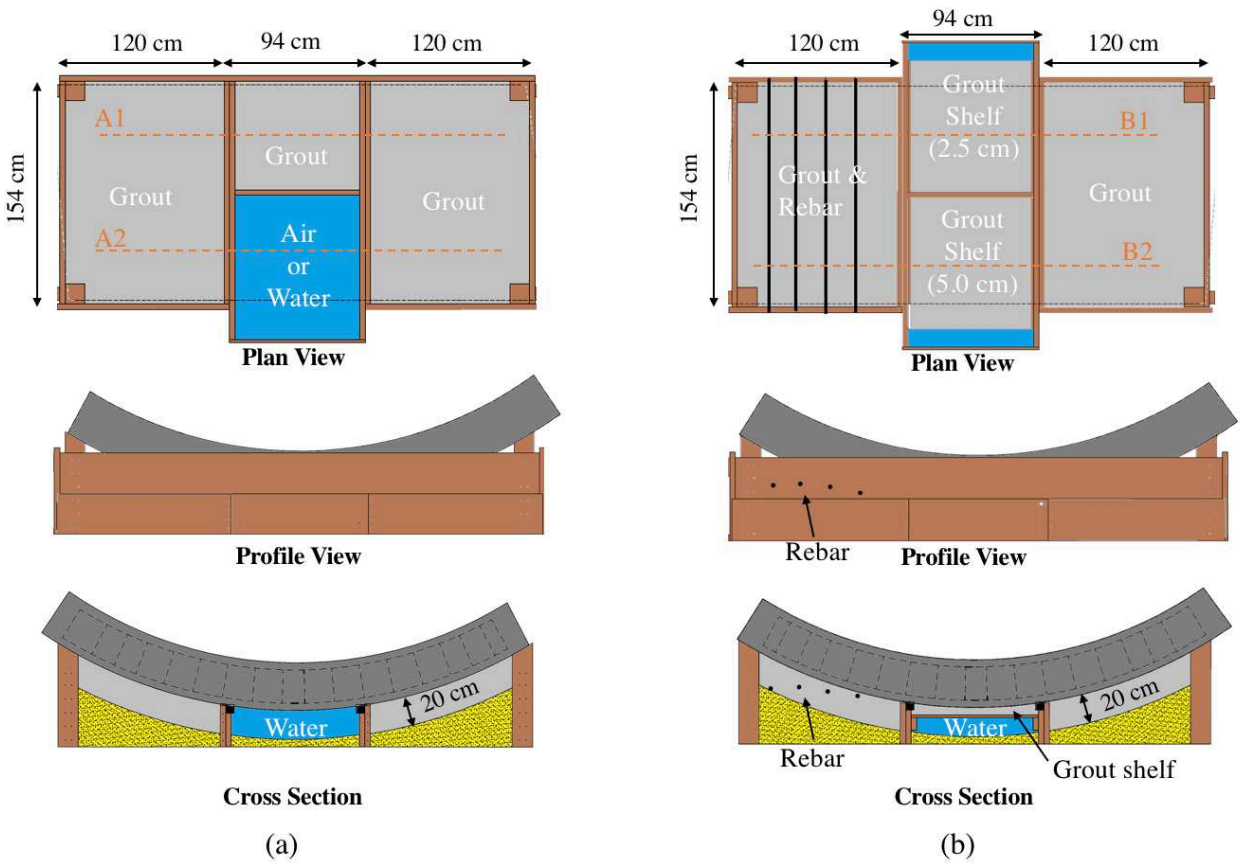

Figure 5.11 (a) Support frame A plan view, profile view, and cross section (b) Support frame B plan view, profile view, and cross section

Segment support box A provided three different scan lines; a fully grouted annulus (A1), a water-filled void (A2-water), and an air-filled void (A2-air). The two outer and one central compartment in box A was filled with grout, while the remaining central compartment was left empty to be filled with air or water. Segment support box B provided additional scan lines with the two outside compartments completely grouted, and shelves installed on the two center compartments with grout placed in between the shelf and the segment extrados. This enabled a 2.5 cm (1 inch) grout layer (B1) and 5 cm (2 inch) grout layer (B2) in contact with the segment and a water or air-filled void beneath. The two grout thicknesses were designed to demonstrate GPR signatures from varying grout thickness that may form in contact with the segment with a void behind. Additionally, rebar was embedded within the grout compartment at varying depths to act as perfect reflectors to provide evidence of GPR penetration depth and grout EM velocity. Rebar was positioned at depths of 2.5 cm (1 inch), 5 cm (2 inch), 10.2 cm (4 inch), and 20.3 cm

(8 inch) beneath the segment, spaced approximately 20 cm apart from each other and positioned such that each rebar in the grout was radially centered in the segment's steel rebar grid. This prevented shadowing effects of the segment's rebar falsely masking the rebar in the grout. The rebar in the grout was meant to provide additional evidence for the grout attenuation constant as well as to help estimate the grout EM velocity.

5.2.1.2 Grout

Two-component grout was prepared by mixing component A in a colloidal mixer, according to the mix design described in section 3.3. Component A was then transferred to an agitator tank where it was kept until being pumped. Pumps on the agitator tank were used to pump in the component A through a hose. The sodium silicate accelerant (component B) was pumped in separately at a controlled volumetric flow rate. Both components were connected with a wye-connection through a 1.2 m pipe to emulate the mixing pipe length on the TBM. The two component pumps were turned on individually while pumping grout into a garbage pail and monitoring the measured flow rates. When the grout was observed to be gelling in 15 s, the grout was then poured into the grout compartments under the segments.

5.2.1.3 GPR

GSSI GPR equipment was used for the grout and void assessment. Following the results from the segment penetration tests, 900 MHz and 350 MHz GSSI antennas were used with a SIR 4000 control unit. Only the 900 MHz antenna was used for the secondary scans conducted 3 weeks after the initial scans.

5.2.2 Test Procedure

The segment support frames were constructed and the segments placed on top as shown in Figure 5.12a-c. One cubic meter of grout component A was mixed in a colloidal mixer and then moved to an agitator tank for two hours. This emulates conditions experienced on the TBM since grout will typically take a minimum of two hours to be transported from the batch plant into the annulus gap. Component A set time has effects on the set properties of the final product as the free water content in the mix declines over time. The component A pump and the accelerant pump were attached to volumetric flow meters and piped into a wye connection with a

122 cm (4 foot) pipe outlet, also emulating the Rondout TBM mixing pipe length. Volumetric flow rates of the Component A and the accelerant were dialed to produce the Rondout project mix design, described in section 3.3. Component percentages were achieved by first pumping component A into an empty container until producing a steady flow rate, then dialing in the accelerant pump to meet the mix design. After grout was observed to properly gel the pipe was inserted into the grout compartments and filled individually.

(a) (b) (c)

Figure 5.12 Photos of constructed support frames (a) Support frame A; (b) Support frame B; (c) Scanning segment on support frame B with 900 MHz antenna

After the compartments were grouted, GPR scan lines were conducted. The earliest scan line was conducted approximately 12 hours after grout was placed, representing the time between grout placement and scanning in the TBM. GPR scans were initially tested with air filled voids that were then filled with water so that water was in contact with the bottom of the segment. GPR scans using the 900 MHz antenna were re-performed after 3 weeks.

5.2.3 Void Detection

Radargrams from 900 MHz GPR imaging of support box A are presented in Figure 5.13 along with geometry of the scan line cross sections. Time zero, bandpass, and range gain filters were applied to the radargrams. The color scheme displayed used a selected amplitude threshold such that the positive white peaks turn to blue, and the negative black peaks become red making high amplitude reflections more easily identifiable. This enables differentiation between reflections off of different material boundaries.

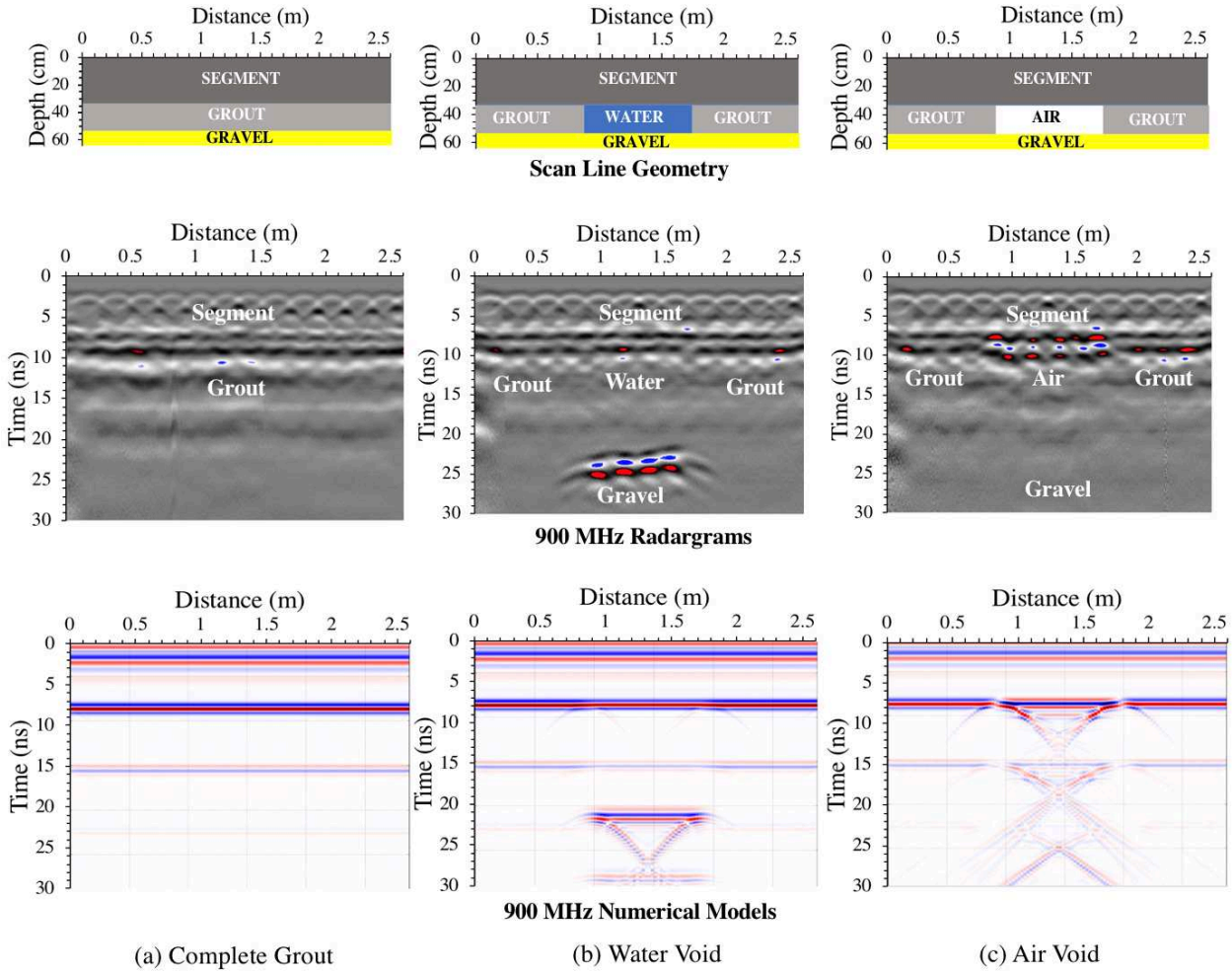

Figure 5.13 Results from the field test experiment with the scan line geometry on top, GPR radargrams in the middle, and numerical model results on the bottom (a) Scan line A1 with complete grouting (b) Scan line A2 with water void (c) Scan line A2 with air void

The segment-grout interface is revealed as a linear reflection band between 7 and 12 ns in Figure 5.13a due to the uniform segment thickness and constant EM velocity. Shadowing effects from the rebar created a wavy pattern in the returned signal. The segment-water interface from the water void in Figure 5.13b reflects the EM wave at approximately the same amplitude, phase, and time as the segment-grout interface, therefore making the two primary reflections indistinguishable. This is due to the reflection coefficient of the concrete-grout and concrete-water boundaries being similar, shown in Table 4.2. However, because water has a significantly lower electrical conductivity, the EM wave is able to travel through the full water thickness and reflect off the gravel boundary behind it. This creates the reflected signal between 21-23 ns. This reflection is strong because the impedance contrast between water and gravel is large and water

allows for a sufficient amount of EM energy to pass through without significant attenuation. The lack of a strong reflection beneath the grout reflections (Figure 5.13a) is the first line of evidence that the GPR signal was unable to penetrate the grout thickness.

Air voids leave a different signature than the water voids due to the difference in impedance between water and air. Air voids are distinguished by the in-phase reflected wave compared to the phase reversal of the grout reflection. The phase difference is demonstrated in Figure 5.13c by the reversal in color bands between 7 and 12 ns at the void location. The secondary reflection at the bottom of the air void occurs approximately 1.35 ns after the primary which makes the secondary reflection indistinguishable from the primary, unlike the late arriving strong reflection in the water void. As is commonly observed in air voids of small thickness relative to wavelength, the two reflected waves off the top and bottom of the void combine with each other to induce positive interference which increases the amplitude of the returned EM signal and amplifies the strong reflection on the radargram (Chen and Scullion, 2008; Nobes, 2016).

GPRMax numerical models were run to create idealized radargrams to compare against the field data. Material properties used in the model are displayed in Table 4.1 and the model geometry is shown in Figure 5.13a-c. Wooden structural supports in the support frame were not modeled for simplicity. Similarly, rebar in the segment was not included in the models in order to clearly represent void signatures without convoluting the results with interference patterns, as was the case with the penetration test model.

Numerical models can be interpreted similarly to the field results with more clearly identified reflections and lack of background noise. The reflection coefficient between the segment and grout is negative which indicates a phase reversal illustrated on the model by the negative (red) central peak of the returned signal shown in Figure 5.13a. The second reflection shown by the model between 14-16 ns can be interpreted as a duplicate of the first reflection due to the commonly observed ringing effect. Ringing is caused by the reflected EM wave from the grout interface bouncing off the air as it returns to the surface and then reflecting off the grout interface a second time. Ringing was not as evident in the field results due to the addition of background noise and greater signal attenuation. Another line of evidence that this apparent reflection is due to ringing is that this reflection shows up uniformly in all the models regardless of void type present. Numerical models presented the same void signatures for the air and water

voids as the field results, shown in Figure 5.13b and c. However, the air void model did not produce the interference effect observed in the field tests. Instead it produced separate arrival bands for the primary and secondary air void reflections.

Void detection radargrams created using a 350 MHz digital antenna from GSSI are depicted in Figure 5.14a-c. These results correspond to the same scan lines presented in Figure 5.13. As shown, the 350 MHz demonstrated capability of detecting the void signatures but had significantly lower resolution. The lower resolution makes the air void phase-shift contrast less pronounced and limits the size of the void that can be detected. Due to the minimal penetration depths necessary for this investigation, the 900 MHz antenna was selected for all further work.

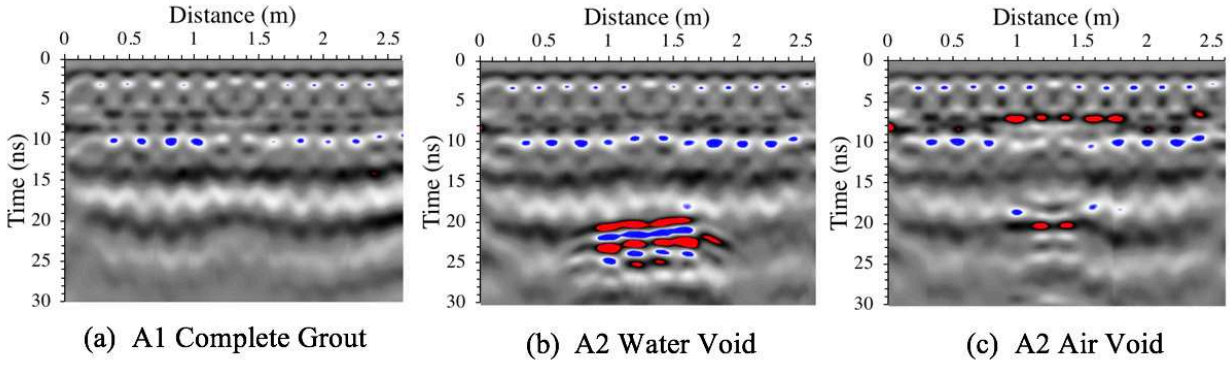

Figure 5.14 Radargrams for 350 MHz antenna on Scan lines A1 and A2

5.2.4 EM Penetration through Grout

GPR results along scan line B1 after 12-hour and 3-week grout set time are displayed in Figure 5.15a and b, respectively. The 12-hour set time grout resembles the fully grouted scan line A1 from Figure 5.13a, where no clearly identifiable features are demonstrated below the concrete-grout reflection band between 7 to 12 ns. The lack of any parabolic reflections from steel is indicative that the EM signal was unable to penetrate through any thickness of grout at the 12-hour set time. Similarly, the air void beneath the 2.5 cm grout thickness was not discernable with a phase-shift or strong reflection Figure 5.13c.

Scan line B1 after 3-week grout set time, shown in Figure 5.15b, demonstrated evidence of partial EM wave penetration through the grout. The segment-grout reflection band between 7 to 12 ns is less intense and interrupted by subtle parabolic features. The loss of intensity of this reflection is demonstrated by the lack of the thick white linear band at approximately 11 ns

displayed in the 12-hour radargram. The subtle parabolic features between 0.4 and 0.9 m and at times greater than 11 ns can be inferred to be the steel rebar reflections. These features are more easily identifiable by comparison to the numerical model results also shown in Figure 5.15b. Based on an overlay of the numerical model with the field results, the steel reflections shown in the actual GPR scans are inferred to be rebar embedded at depths of 2.5 and 5 cm. The air void buried beneath 2.5 cm of grout in the center of the scan line is not as evident as the air void demonstrated in Figure 5.13c but the air void interrupts the linear segment-grout reflection band similar to the rebar reflections. The right side of the scan line, between 1.9 to 2.5 m, provides the baseline conditions for full grout reflection with no interruption at the same set time.

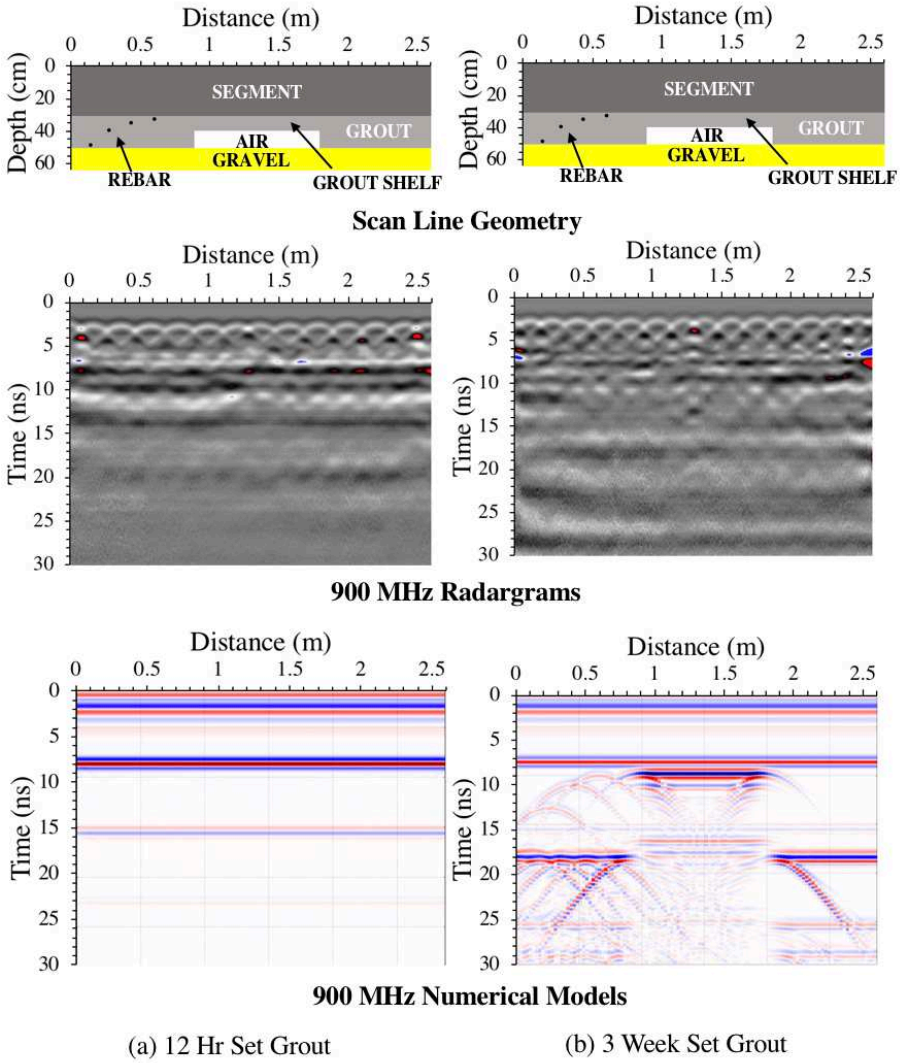

Figure 5.15 GPRMax models of scan line B1 with air and a 900 MHz frequency. (a) Grout electrical conductivity set to 4500 mS/m; (b) Grout electrical conductivity was set to 0.1 mS/m

The numerical model results shown in Figure 5.15a and b used different values for the grout conductivity. A conductivity equal to 4500 mS/m was used to model 12 hours and 0.1 mS/m was used to model 3-week old grout. These conductivity values were selected to represent a relatively high conductivity material as is expected for the grout at early set time based on lab testing results from Karlovšek et al. 2016, and a relatively low conductivity comparable to a dry concrete. Figure 5.15a, displaying model results with a relatively high electrical conductivity demonstrates a linear segment-grout reflection with neither the rebar nor air void beneath the grout identifiable. This result coincides with the observation from the field and represents a skin depth of less than 2.5 cm at a 12 hr set time. Figure 5.15b, with a relatively low electrical conductivity produces reflections for all four rebar within the grout, as well as the void reflection beneath the grout shelf. The rebar is displayed as parabolic-shaped reflections at times beyond 9 ns and distances between 0 to 0.7 m. The left most rebar is not as clearly identified since it is masked by the gravel reflection. The air void is identified immediately beneath the grout reflection and demonstrates a phase shift after the wave has passed through grout. Field results for the 3-week set grout displayed partial features from the low-conductivity model, indicating the actual conductivity of the grout after 3 weeks has decreased and enables a penetration depth of approximately 5 cm.

5.2.5 Discussion

Complete grout washout within the tunnel annulus grout, as described in section 2.1, has been shown to be identifiable with a 900 MHz radar antenna and is both more likely than partial washout of grout and a more serious issue to identify in the field. Water and air voids at the interface of the segments revealed signatures that technicians with minimal training could identify if the technology were to be deployed in the field. The main signature demonstrated by the water void was the reflection of dry gravel at the bottom of the water void. Imaging the bottom water-void reflection requires that the water present in the void has an electrical conductivity of that equal to the measured in-situ conductivity of the ground water (55 mS/m), or at least less than 500 mS/m, to allow for full signal penetration. In-situ rock in the tunnel will be fully-saturated which will decrease the reflection coefficient at the water-rock boundary and make the void signature less strong then demonstrated here. However, the difference in

impedance between saturated limestone and water produces a reflection coefficient of 0.522, shown in Table 4.2, which is still sufficient to create an identifiable water void signature.

While not directly demonstrated from this testing, several other possible cases in the annulus gap can be inferred from these results. Grout formed at the bottom of an air void would produce very similar results to the air void shown from this testing. However, grout at the bottom of a water void would diminish the reflection at the bottom of the water void. This is due to the smaller impedance contrast between water and grout compared to water and rock demonstrated in Table 4.2. The water void with grout at the bottom may still be detectable with careful inspection for a secondary reflection beneath the primary reflection band. Rock over break may be detected as similar to the air void signature with a parabolic feature if there is some air or water surrounding the rock over-break since the reflection coefficient between limestone and the segment is too low to be detected on its own (Lalagüe et al., 2016).

Penetration tests through grout demonstrated that voids formed beneath a 2.5 cm thickness of grout may not be detectable with the GPR at set times less than 12 hours, but have the potential to be detected after a 3-week set time. The signature used to identify this in the field is a disturbance in the linear reflection pattern from a fully grouted annulus. This type of feature is most easily identified when scanned next to a region of complete grout. Since a 3-week set time did not enable complete penetration of grout beyond 5 cm, it is unlikely that any set time would allow for the complete penetration. Inability to penetrate a GPR signal through more than 5 cm of two-component grout implies that the grout thickness and grout-rock interface may not be resolved. The penetration depth of the GPR coincides with laboratory measurements described in section 4.2.

The position at which GPR data is collected on a TBM is not significant for detecting complete washout of the grout can since the void signatures are evident while the grout is at early set time. Thin layers of grout, less than 2 cm, adhered to the liner extrados surface may become penetrable with the GPR after three weeks. Voids formed within or behind greater than 2 cm of grout are unlikely to be detected with the GPR.

CHAPTER 6
NDT ASSESSMENT OF INSTALLED SEGMENTS

Non-destructive testing techniques using GPR and IE were implemented inside the Rondout tunnel during construction. Both methods were used at the same locations on segments to determine the efficacy of results. Collected geophysical data was later compared to drilled-holes through the segment for physical evidence of annulus grout conditions. The implementation of each method and the corresponding results are described in detail in this chapter.

6.1 GPR Assessment

Implementation of the GPR testing methods was performed at various locations within the tunnel on the TBM trailing gear. Limited access along the TBM was available due to the ongoing construction operations. Regions of known conditions were assessed in the starter tunnel where false rings were installed containing backfilled concrete below the spring-line and air above, as well as at the ring installation location where active grouting was taking place.

6.1.1 GPR Equipment

GSSI GPR equipment was used in this data collection. A 900 MHz antenna was selected based on penetration testing and mock-liner testing described in section 5.1.2.1 with a SIR 4000 control unit. This unit enables live-time imaging of the GPR results along with prescribed filter settings. A transmit rate of 100 kHz is the prescribed rate for the 900 MHz antenna. In order to create the greatest resolution image for imaging the annulus, 90 scans per foot were selected with 512 samples per scan. The samples per scan describes the number of points collected for each wavelet trace, where greater samples are needed for imaging greater depths. The number of scans per foot effects how many wavelet traces are collected per horizontal unit, with more samples creating better resolution but requiring slower collection speed. Data was collected for 40 ns which is greater than the longest time needed to image annulus voids of the largest anticipated size.

Filter settings were selected in order to best interpret the field data and were calibrated to void images from the prior mock-liner test results described in section 5.2. An infinite impulse

response (IIR) boxcar filter was applied to the data with a 1500 MHz low pass and 500 MHz high pass to reduce background noise. An exponential gain filter was applied to amplify the reflected wave data at the segment-annulus space boundary and reduce the rebar reflection amplitudes in the segment. By trial, these filters provided the best results for data interpretation both in real time and with post processing.

The GPR antenna was attached to a retractable rod and was fit with a calibrated measuring wheel. The antenna was moved along each scan line by pressing the antenna firm against the segment and maintaining contact between the bottom of the antenna to the segment intrados surface. Slight data variation can result from the antenna becoming differentially elevated off the segment surface along a scan line and producing non-uniform ground-coupling effects. For proper ground-coupling with the antenna, the antenna should be no further than a distance of 1/10 of the signal frequency off the concrete surface (Geophysical Survey Systems Inc., 2017). For the 900 MHz antenna being used, this requires the antenna be no more than 1 in off the concrete surface. The curvature of the segments does not inherently create a gap larger than 1 in between the antenna bottom and the concrete, but firm pressure must be maintained throughout the scan.

6.1.2 Longitudinal vs Circumferential Scan Lines

GPR scan data was collected in the Rondout Bypass Tunnel during construction of rings 45 to 55. This translates to bored tunnel depths between 68.5 m (225 ft) and 83.8 m (275 ft) along the alignment within the Shale unit. GPR scanning of the segmental liner can be performed in two directions: longitudinally along the tunnel alignment, and circumferentially around each tunnel ring. Both methods were tested in the tunnel, however, preference was given to circumferential scanning for a multitude of reasons.

The primary reason for focusing on circumferential GPR data is that grouting data is desired to be collected by mining cycle push. If there is suspicious grouting performance, either from grout volume deficiency/excess, observed grouting leakage through the inner tail-shield brushes, or known high groundwater flow rates or pressure, the contractor must provide assurance on the complete annulus grouting for that specific ring. Therefore, performing a circumferential GPR scan can provide a data set for the suspected ring.

Secondly, large interference from the gasket joints between segments was observed in the GPR radargrams, as demonstrated in Figure 6.1. This interference is caused by the GPR signal reflecting off the gasket joint when it is located within the radial spreading front of the EM wave. The approximate distance of interference from the gasket joint was found to be 0.3 m, which is evident in Figure 6.1 between 1.4 to 1.7 m horizontally, and at a time of 7 ns. Since the width of each segment is only 1.5 m, gasket interference decreases the available annulus data size to less than 1 m per segment when scanning longitudinally. On a circumferential scan, annulus data can be observed for up to 2.1 m per segment. With five accessible segments available to scan per ring from a single forward bridge position, approximately 10 m of the ring can be scanned. This total scan length accounts for obstacles on the TBM trailing gear that prevent access to certain aspects of the ring.

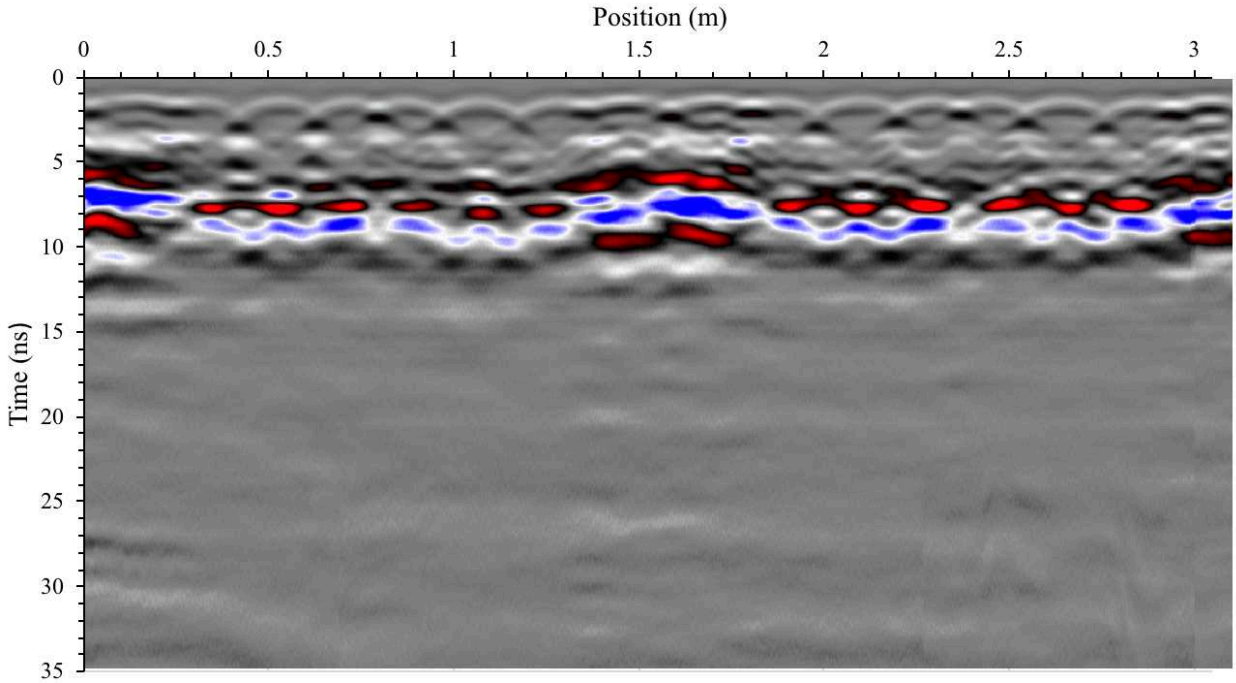

Figure 6.1 Longitudinal scan radargram crossing a segment gasket

Lastly, when performing longitudinal scans, the different segmental ring configurations makes a perfectly linear scan line down the tunnel alignment not possible if trying to avoid scanning over the center lifting portal and across the circumferential segment gasket-joints. Avoiding these are necessary to create an annulus image that can be interpreted in the field

without excessive interference noise. However, by distorting the scan line to avoid these obstacles, the rebar spacing becomes non-uniform and makes the reflected grout image non-linear and more challenging to interpret. The reflection of the grout at 7 ns on Figure 6.1 is fragmented due to the distorted rebar spacing scanned.

6.1.3 GPR Scanning Access

Access to the greatest circumferential area of the tunnel liner was achieved on the forward deck location of the TBM trailing gear. This position was 6 to 8 rings behind the ring erector on the TBM. At the time of data collection, this contained grout with a set time between 24 hours and 6 days. The grout set time variation was due to different down time events associated with the tunneling process. At estimated maximum tunnel advancement rates, this position could contain grout with 12 hours or less set time. Figure 6.2 depicts a cross sectional view of the trailing gear at the forward bridge scanning location. The portions of the segments highlighted in yellow are areas that could be accessed with the antenna. Figure 6.3 shows pictures of scanning the segments illustrated in Figure 6.2.

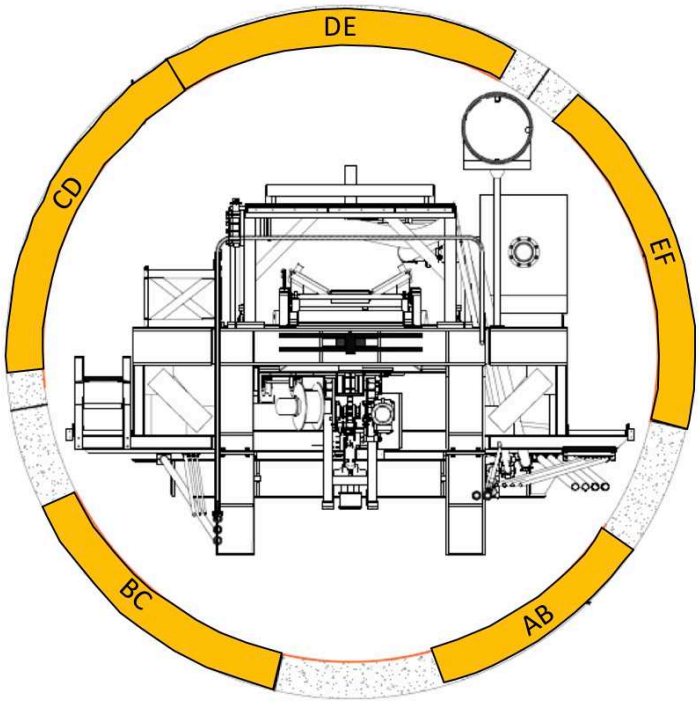

Figure 6.2 Segment scanning access from TBM forward bridge

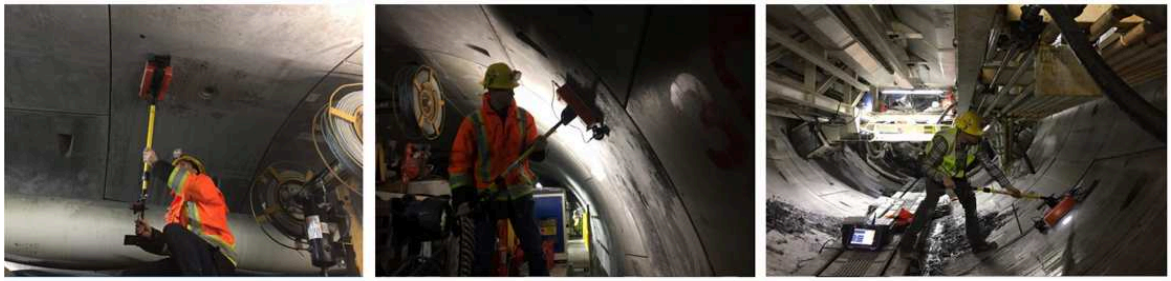

(a) Segment DE (b) Segment CD (c) Segment AB

Figure 6.3 Photos of GPR scanning conducted at the forward bridge on three different segments

Segments at the tunnel crown at the second ring position behind the ring erector were also scanned. This location allowed for scans to be conducted during and after grout injection. While the grout filling was being conducted during mining advancement, a time delay between the completion of the mining cycle and completion of the grouting cycle allowed for the crown to be scanned with air still behind the segment, and again when grout had been completely filled.

6.1.4 Baseline Field Assessment

As described in section 6.1.3 , crown segments were scanned before and after grout injection. These radar images provided a baseline condition to compare to the mock-liner experiment and demonstrate known air versus known grout behind the segments. Figure 6.4 displays three radargrams taken at the crown, two rings behind the ring erector. In Figure 6.4a, the tail shield had just passed over the segment, known by the mining position, but grout had not fully filled the annulus, which was known by the grout volume injected. This provided a scan with a complete air-filled annulus gap. Figure 6.4b was taken during grouting when 90% of the grouting was complete. The radargram taken can be interpreted as being partially grout and partially air. Figure 6.4c was taken after grouting was completely finished, and the radargram can be inferred to be a fully grouted annulus space.

In each of these radargrams, the same filters were applied to magnify the wave intensity at the concrete-annulus space position which was previously determined by the mock-liner experiment. Rebar reflections, which appear as parabolas, were dimmed relative to the annulus material reflection. All EM pulses were recorded for 40 ns to enable potential water void reflections to be recorded at positions between 20 to 30 ns depending on the anticipated water void depth.

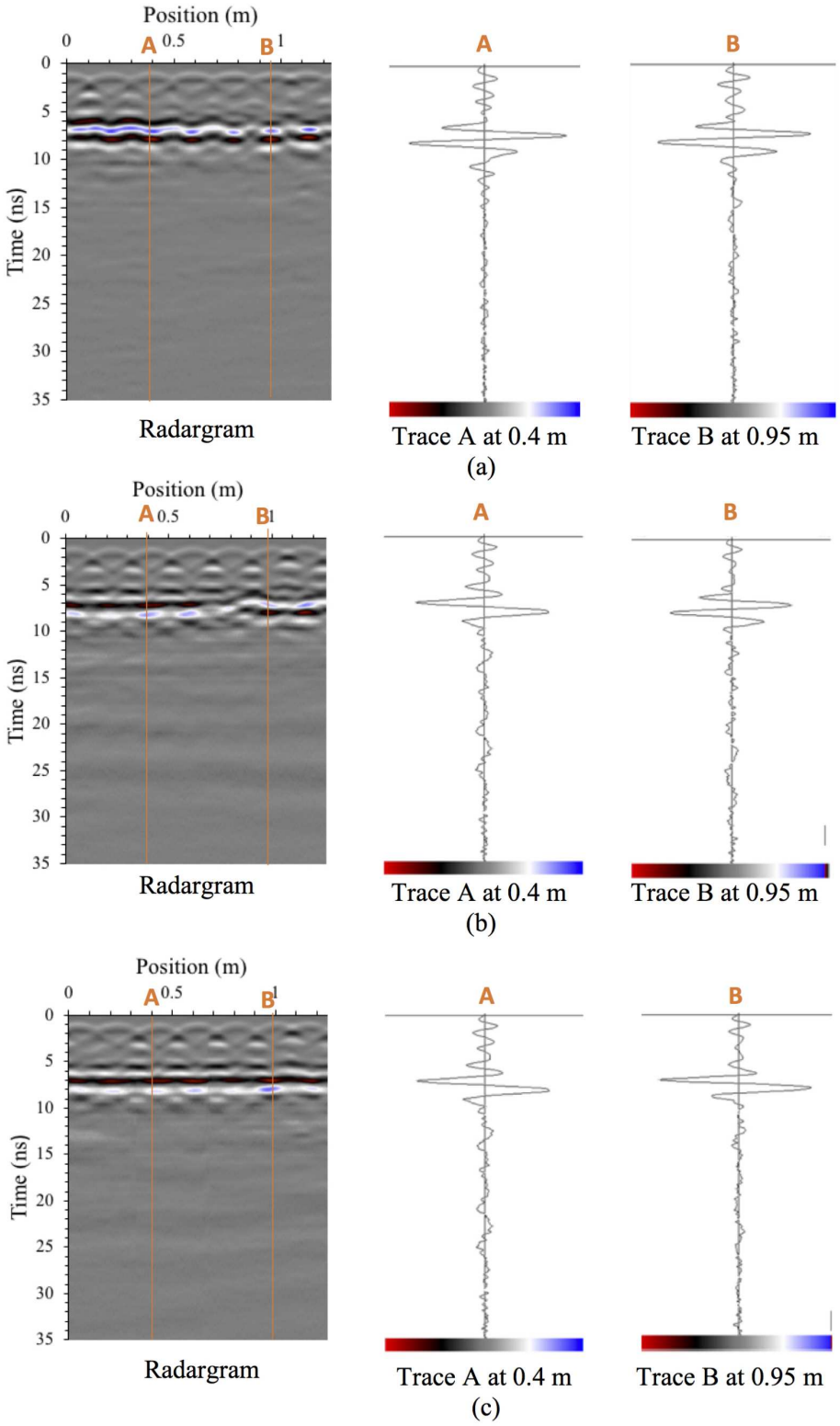

Figure 6.4 Radargrams and wavelet traces for scans conducted immediately behind the ring-erection. (a) Before grout filling leaving complete air behind ring; (b) during grout filling with assumed partially grouted annulus; (c) after fully grouting the annulus

The air reflection in Figure 6.4a is illustrated on the radar gram as a wavy pattern centered at 7 ns. The central positive peak, color coded white with a high-amplitude blue threshold to demonstrate reflection intensity, is indicative of an in-phase returned wave which would be expected from an EM signal traveling from concrete into air. The wavy pattern of this reflection band is caused by shadowing effects of the rebar cage within the segment. To assess all the radargrams uniformly, single EM wave traces are analyzed at positions at the top of the rebar parabolic reflections. This provides the best means of observing the phase-shift when comparing air to grout. At radar positions A and B, single wavelets traces are shown next to the radargram. For both traces, the central peak is observed to be positive at approximately 7 ns.

Figure 6.4b contains a grout reflection band on the left side of the radargram, from 0 to 0.8 m, and air reflection on the right side of the radargram, from 0.8 to 1.2 m. The grout reflection pattern has a negative (black/red) central peak, centered at 7 ns. The phase shift between the air and grout reflection can be seen in the wavelet traces when comparing the amplitude sign of the largest central peak at 7 ns. Furthermore, the grout reflection pattern displays a less wavy signature when compared to air. This may be caused by a smaller EM spreading wave-front in grout compared to air in addition to the high conductivity of grout compared to air.

Figure 6.4c is representative of a fully grouted annulus space. The uniform horizontal reflection band at 7 ns in the radargram is displayed with no interruptions. The wavelet traces demonstrate the same phase-shift of the reflection at points A and B.

Due to the relatively low recorded water flow rates during mining, no water voids were able to be imaged within the tunnel at the time of testing.

6.1.5 Complete Grouting Scan

Scans conducted on the same segment location at different grout set times were performed to observe any potential changes in the radargrams. The greatest ability for the GPR to penetrate through the grout would be after several days of set time. However, previous testing has demonstrated the inability for the GPR to penetrate more than 2.5 cm of the grout even after weeks of set time. Figure 6.5a and b demonstrate a radargram of a fully grouted annulus space. Both images revealed the same characteristics with no observable changes after 5 days. The

grout images can be compared to Figure 6.4c for a known fully grouted annulus space. These images were representative of the majority of scans taken within the tunnel.

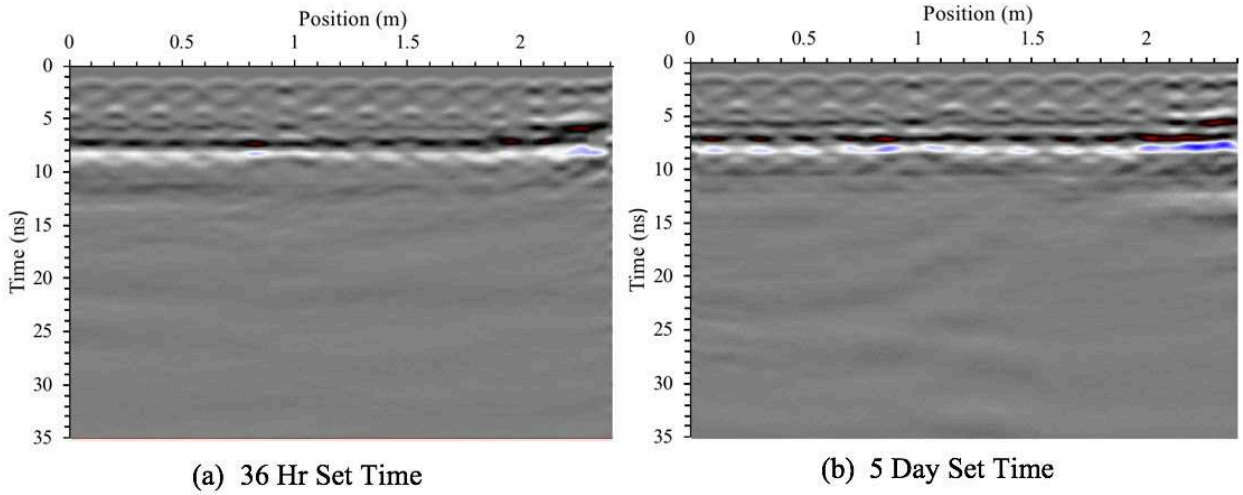

Figure 6.5 Complete grout scans conducted on Segment CD Ring 36 at different grout set times

6.1.6 Air Void Detected

An air void was identified while scanning the segments. The void was determined to be approximately 1 m in width and not found to have extended beyond the segment it was detected behind. Figure 6.6 displays the radargram from the void which was detected in real-time.

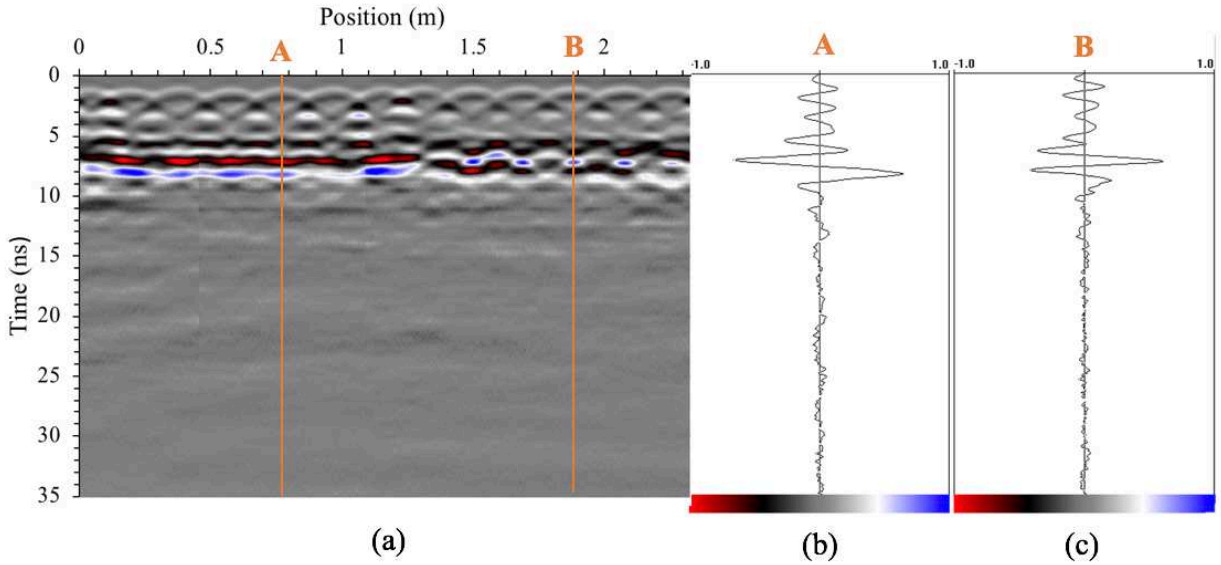

Figure 6.6 (a) Radargram; (b) wavelet trace at 0.75m; (c) wavelet trace at 1.9 m for detected air void on Ring 41 segment EF

The air void demonstrated in this radargram resembles the partially grouted annulus image from Figure 6.4b. The left side of the radargram displays a linear grout reflection band with a central negative peak at 7 ns. At approximately 1.3 m, a phase-shift can be seen as the reflected wave had reflected off a lower dielectric medium. Wavelet traces at locations A and B on the radargram help to demonstrate the phase-shift of the reflected wave. The wavy signature of the air reflection compared to grout can also be seen in the two reflection bands at 7 ns before and after 1.3 m.

6.1.7 Discussion

Field data collected by the GPR supports that complete washout of the grout leaving an air void is easily detected. Use of the delayed grouting time to fill the annulus space provided clear evidence of air versus complete grouting on the same segment scan line. The use of the phase shift for the air voids is the best line of evidence for field detection. This can be done by using the radargram images combined with single wavelet traces which can be analyzed in live-time. The lateral delineation of the void is easily determined by use of GPR for both air voids shown in the field. Since water was not present at the time of scanning, no evidence of water voids was directly gathered in the field. However, the mock liner tests demonstrated that water would be detected by the reflection between the water-rock boundary occurring at a later time. With grout present at the back of the water void, the secondary reflection strength would be diminished compared to the strength of a water-rock boundary, but may still be detectable. As discussed in section 5.2.5 of this thesis, any grout at the immediate boundary of the segment would appear the same as a fully grouted annulus, and therefore these two cases are not possible to distinguish with GPR alone.

6.2 Impact Echo Assessment

Impact echo was tested in the tunnel at locations along GPR scan lines. Conditions with known-segment backfill were available on the false rings in the starter tunnel. Since IE base-line conditions were not established on the mock-liner experiments, the false-rings provided the baseline conditions necessary to determine the viability for IE to differentiate complete grouting from complete washout with air. No known areas of water washout were available to establish base-line conditions for water voids.

6.2.1 IE Equipment

A CTG-2 impact echo device manufactured by Olsen Engineering was used to collect data. This device comes with a built-in trigger that can generate a uniform pulse of magnitude and frequency spectrum. A 3.5 oz hammer which was also used as an alternative to the trigger to determine which impact method provides the best means of void detection. The device uses a sampling frequency of 4550 Hz and a time window of 22.5 ms.

6.2.2 Data Collection

IE assessment was conducted on the same scanned regions that the GPR was used, in addition to the false-rings installed in the starter tunnel. The false rings are segments installed at the launch of the TBM before the machine was fully buried into the virgin-rock. These rings were initially supported by wooden blocks and later backfilled to the spring-line with concrete. Figure 6.7 displays pictures of the IE equipment being applied to a segment as well as a cross section of the false rings.

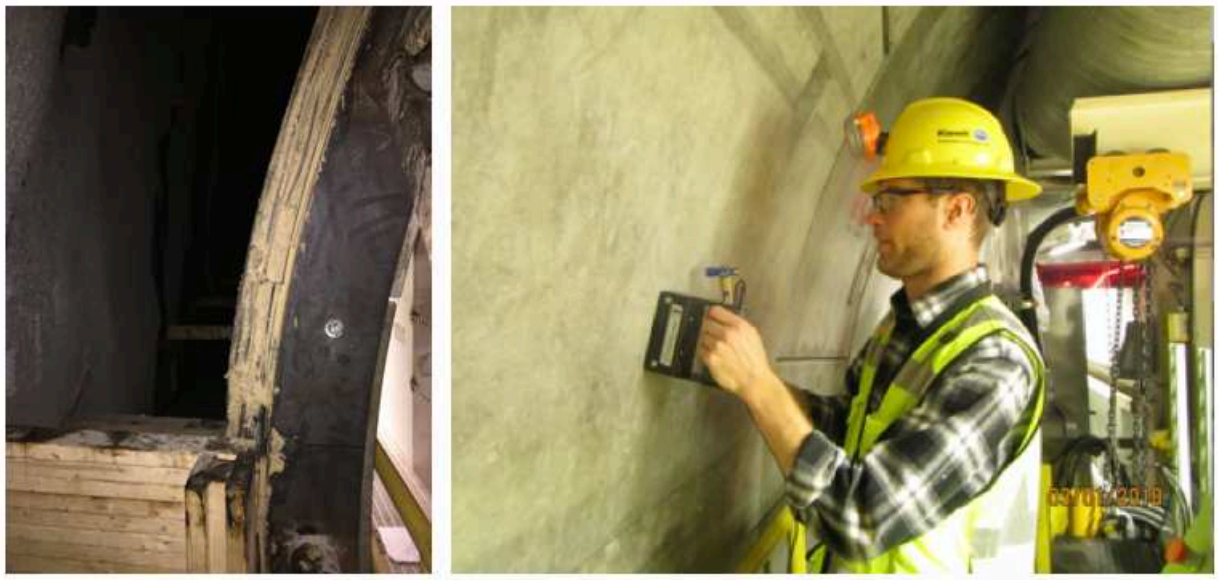

Figure 6.7 Photos of IE data collection on the false ring above the spring-line with air behind the ring

IE was tested on 11 different rings within the tunnel with differing backfill conditions. Backfill conditions varied between known air, known concrete, assumed grout backfill with different set times, and one discovered air void. For each point measured, three IE shots were

taken to eliminate obvious false readings. False readings show up in the data with no distinct waveform and may result from outside noise interference, such as extraneous vibrations in the tunnel or unintended disturbance to the device.

6.2.3 IE Data Processing

Impact echo data was processed according to steps outlined by Ryden et al. (2013). Waveform data was first cut using a boxcar method to eliminate the time delay at early time and the late arriving waves which can be assumed to be background noise. A Fourier transform was then applied to the waveforms and the Q analysis was performed, as described in section 2.3.3 . An automated Q analysis was performed on the data where a search function would find the peak frequency between 5,000 and 10,000 Hz. The narrow search was implemented to eliminate peaks associated with early and late arrival times. The amplitudes were then normalized to the peak amplitude to create uniformity amongst the Q selection of all samples.

Several filtering options were explored to enhance the Q-value analysis. First, the use of a moving average smoothing function was applied to the FFT data set. Figure 6.8 shows the difference in FFT data for a single sounding location with different smoothing functions applied. The smoothing function was found to lower the Q value with the increase of moving average smoothing points. Figure 6.8 demonstrates that as the FFT curve is smoothed, the relative peak becomes less prominent. The material type behind the segment was also found to influence the amount of Q value decrease with the number of moving-average smoothing points applied, with air soundings disproportionately decreasing the Q-value more than grout or concrete. Figure 6.9 demonstrates that the smoothing function has a greater impact on the known void compared to the effect on concrete or assumed complete grouting. For this reason, it was decided not to apply a smoothing function since the goal of the Q analysis is to obtain a large quantitative difference between material types behind the segment.

The range of the boxcar filter applied to the data was found to have a similar effect as the smoothing function. With a tighter boxcar filter, the FFT data became smoother, but the Q values decreased disproportionately for the air void. A boxcar filter between 750 and 5000 μs was selected that allowed for proper Q selection but did not significantly influence the Q analysis.

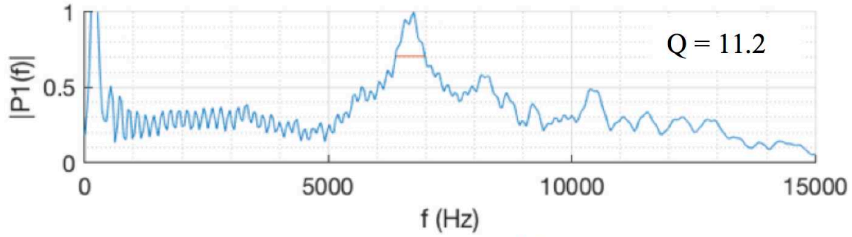

(a) No Smoothing

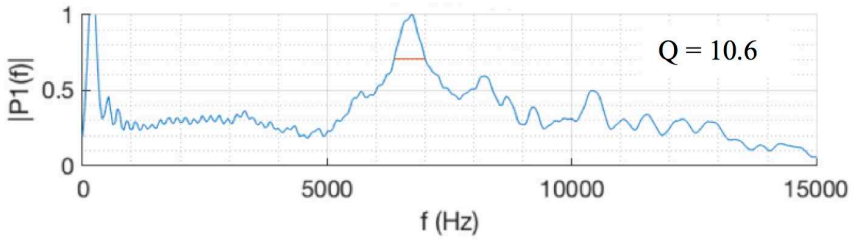

(b) Smoothing (3)

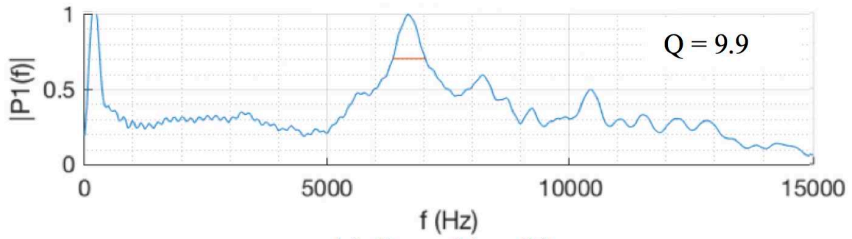

(c) Smoothing (5)

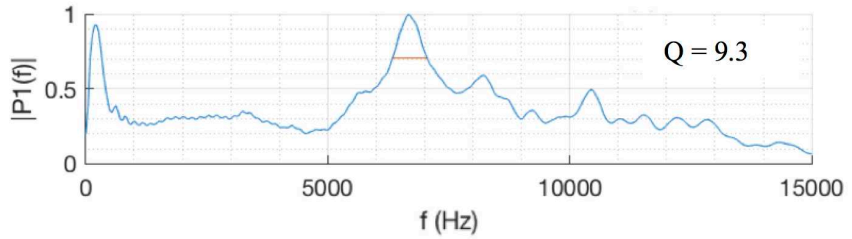

(d) Smoothing (7)

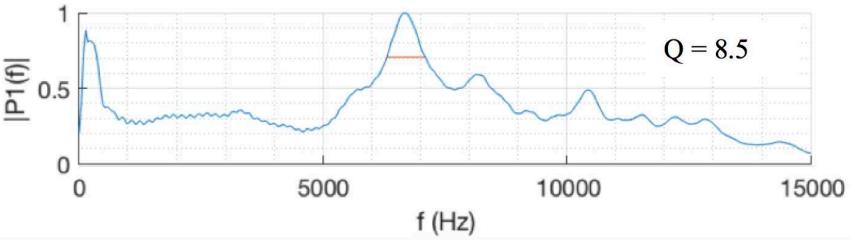

(e) Smoothing (9)

Figure 6.8 Single sounding FFT data for assumed grout behind the segment (Rondout 38) with various number of moving average smoothing points applied

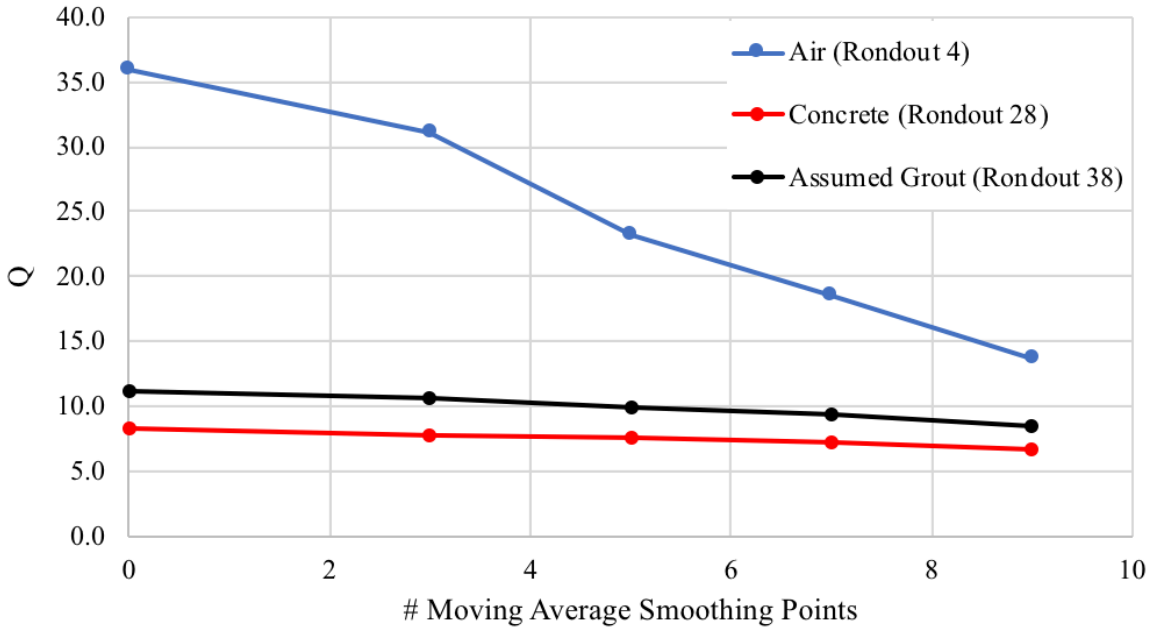

Figure 6.9 Q values for different annulus materials as a function of the number of moving average smoothing points applied to the FFT data

6.2.4 IE Field Data Results

Data collected from inside the Rondout tunnel fell into several categories based on what was behind the segment, including known air, known concrete, suspected good grout, and suspected air void. Due to low water inflow rates, no suspected water voids were identified at the time of the investigation. Figure 6.10 shows the cut waveform and FFT data for three representative locations in the tunnel.

Figure 6.10a demonstrates the response from known air behind the false ring segments. This data matches the expected response for an air void when a prominent peak at the resonant frequency of the segment occurs. The velocity of the segment was inferred from this data as the air voids all created prominent peaks at roughly the same amplitude of 6620 Hz which corresponds to a segment velocity of 4554 m/s.

The Q assessment for the air void provided a value of 35.8, significantly higher than the Q values estimated by Ryden et al. (2013). However, a high Q value is logical for a complete air void behind the segment. Furthermore, the peak frequency is larger for this segment studied compared to the slab described by Ryden et al. (2013). The long response in the time domain of the impact signal is another depiction of the ringing effect created from an air boundary, where the acoustic signal is trapped in the segment and the time response is elongated.

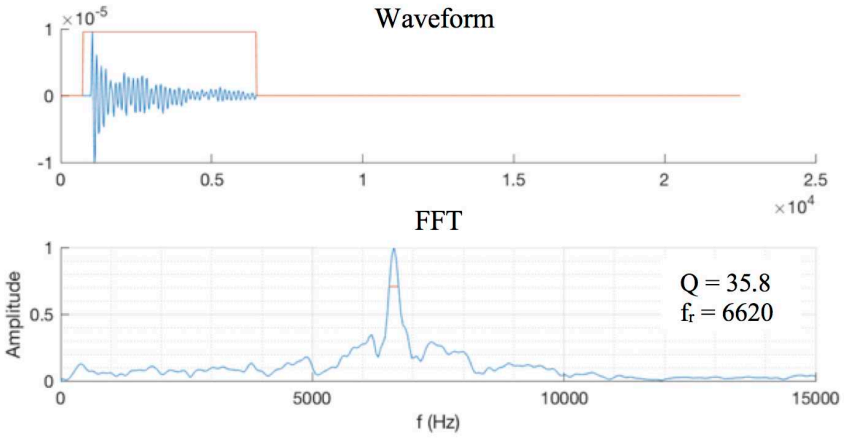

(a) Air behind segment

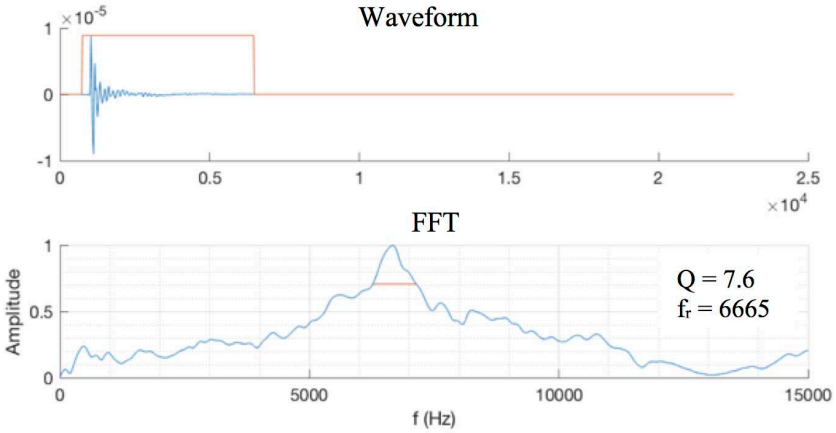

(b) Assumed Grout behind segment

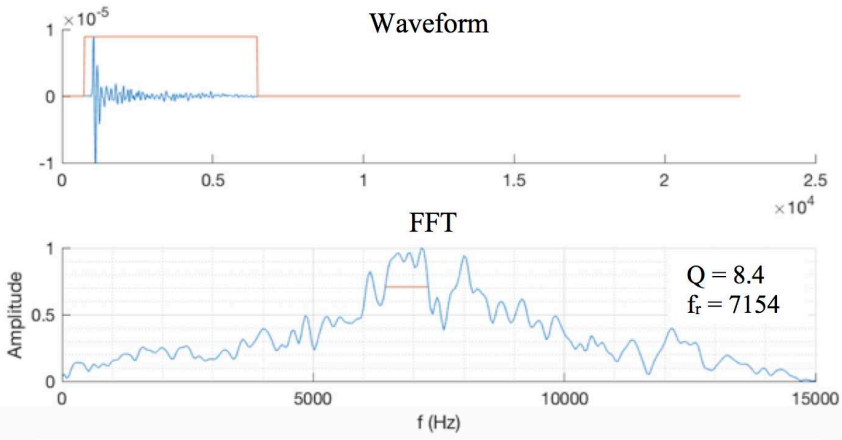

(c) Concrete behind segment

Figure 6.10 IE waveform and FFT data for 3-different annulus backfill conditions

Figure 6.10b represents the IE response for assumed complete grouting. The data shown represents grout with a set time of 9 days, which based on the laboratory P-wave velocity measurements, would reflect approximately 40% of the seismic wave energy at the segment interface. Due to the large contrast between this reflection and an air boundary, which reflects ~100% of the energy (not including energy loss through the segment), a distinct change in the FFT data is apparent. The frequency peak occurring at 6665 Hz is less prominent and more dampened than the peak for the air void reflection. The dampening effect, caused by the loss of energy through the grout, is quantified by the decrease in Q value to 7.7. This value is consistent with the description of the Q analysis by Ryden et al. (2013) in which a weak backfill material was shown to exhibit a noticeable peak at the resonant frequency, but with diminished prominence. Additionally, the waveform in the time domain can be observed to have a shorter tail as less ringing occurs in the segment.

Figure 6.10 c represents the IE response for concrete below the spring-line behind one of the false-ring segments. Since concrete has a smaller impedance contrast with the segment compared to grout, it would be expected to have a less prominent frequency peak than the grout. There was no clear single resonant frequency peak, and the highest amplitude response was at 7153 Hz. The Q value did quantify the resonance to be more dampened than a void, but did not fully capture the decrease in peak prominence compared to grout, as the value of 8.4 was higher than the Q of the grout. This was due to the Q method selecting a localized peak rather than describing the entire response. Visual inspection of the FFT data does reveal a stark contrast when compared to the weaker grout material. The time domain signal response was similar to the grout upon visual inspection.

Q-values for data collected in the field are shown in Figure 6.11, where each bar represents an individual data point. Data collected with the trigger are shown as hollow bars and data collected with the hammer are shown as solid bars. This data set is delineated by the known or expected material behind the segment when the data was collected, which includes grout with various hardening times. A distinction can be made between Q values of the known air and known concrete, as well as with the expected grout. The single concrete outlier demonstrated an FFT response that matched that of other concrete soundings, but the automated Q-method evaluation was conducted on a small localized peak instead of characterizing the overall response.

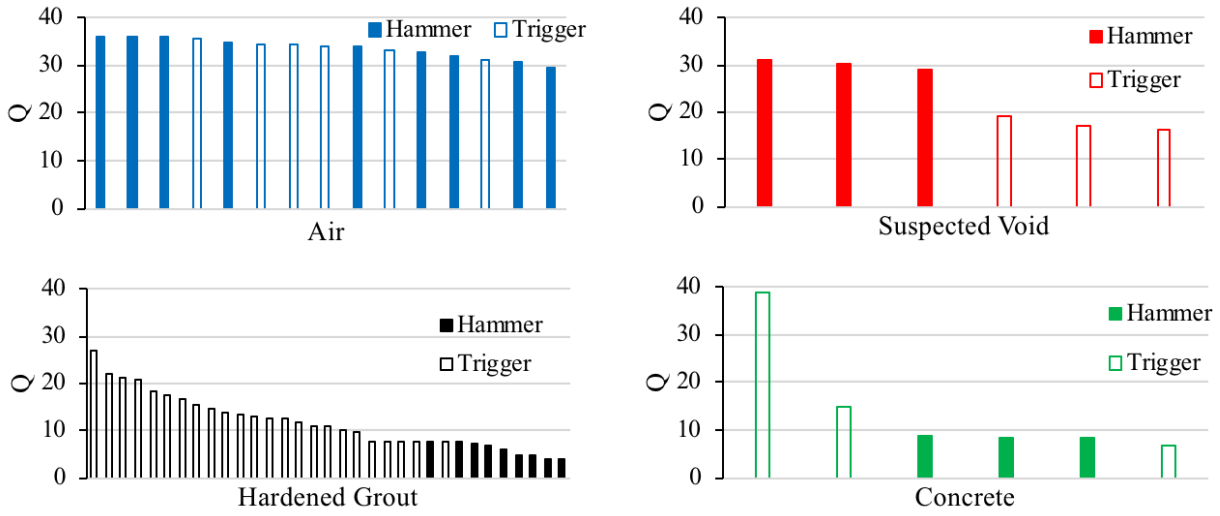

Figure 6.11 Q-values for numerous measurements in the field for different materials behind the segments. Measurements collected by trigger method are hollow and measurements collected by hammer are solid

The suspected void Q values displayed on Figure 6.11 were collected on the same scan line that the GPR device detected an air void. Six soundings were taken on the same spot, three with the trigger which demonstrated lower Q-values, and three with the hammer with higher Q values. Further inspection of the method used to collect data and the hardening time of the grout revealed greater contrast for Q values could be determined across the entire data set when only analyzing hammer collected data.

Figure 6.12 demonstrates various Q values of assumed full-grouting conditions at various grout curing times. Differentiation can also be made between data collected with the IE device trigger and by using a hammer impact. No data was collected on the early cure-time grout by using the hammer. When looking at just the trigger data, it can be seen that the early cured-grout did demonstrate on average higher Q values, as would be expected. With the later cure-time grout, the Q values were lower and more uniform.

The hammer data demonstrated more precision in the Q analysis and contained fewer outliers. This result is likely due to greater energy created from the impact hammer which would allow for stronger reflections at the segment-annulus interface, thereby creating more distinguishable FFT data characteristics. Additionally, the hammer creates a different impact frequency than the trigger, which may influence the response.

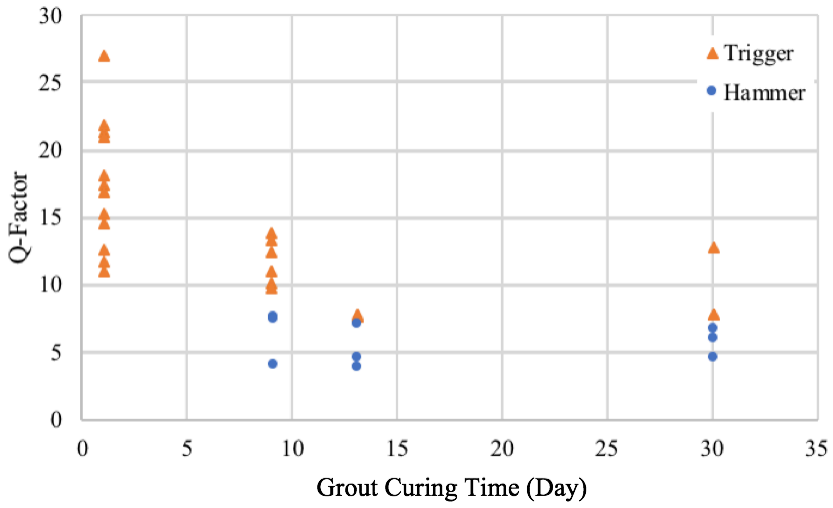

Figure 6.12 Q-values at locations with various known grout-curing time

Figure 6.13 displays the full data set with soundings induced only by the hammer. The earliest set time grout in this data was 7 days. This creates a much more distinguishable Q contrast when differentiating between grout, concrete, and air void. No outliers in this data set existed to undermine the Q value assessment. A lower bound of 29 was found for the air interface behind the segment, and an upper bound of 9 was found for the concrete interface. This created a delta of 20 between the air and concrete. Assumed complete grouting Q values all fell within the upper bound dictated by the concrete.

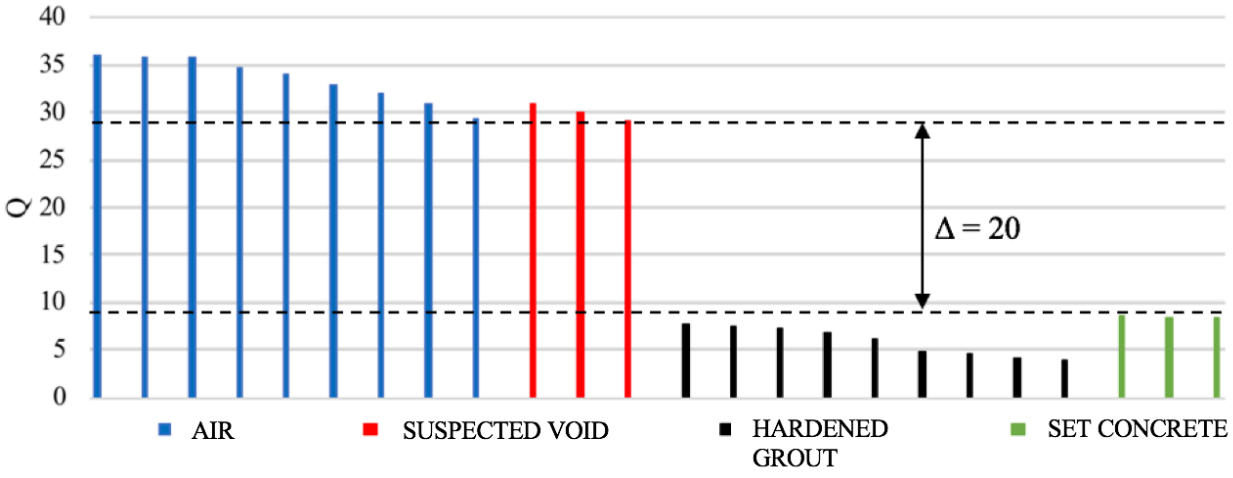

Figure 6.13 Q-values for various annulus-backfill conditions with only Hammer created impacts

Q-value interpretation did not clearly demonstrate ability to identify complete grouting up to the rock interface. In theory, a secondary peak would be present at a secondary interface beyond the segment-grout boundary. This secondary peak would be more pronounced for greater contrast materials with the grout. As limestone or shale would have similar P-wave velocity to concrete, it is not known whether this peak would create enough of a reflection to be identified in the FFT data. A water or air void may create a strong enough reflection if enough energy was initially impacted. However, without direct evidence of what lies beneath the segment-annulus interface, this distinction could not be identified.

6.2.5 Discussion

Impact echo Q-analysis demonstrated clear ability to determine the material type at the segment-annulus boundary by using a hammer for the impact source at grout set time greater than one day. This provides good evidence to support the GPR data where an air void was detected. Since water was not present behind the liner during the time of testing, no immediate evidence was gathered to determine the Q-response of a segment-water boundary. It can be inferred that the Q response would fall in between the grout and air values. However, small void-like features in the grout, such as cracks, can create discontinuities that may be detected by the IE as a void and would be indistinguishable from a full grout washout condition (Schoefs and Abraham, 2012). Therefore, the IE method should be used with caution if a void is suspected.

While, the impact echo provides a geophysical response with the capability of penetrating the grout layer, not enough evidence demonstrated clear ability to detect the boundary of the grout-rock boundary. More testing would be required to effectively demonstrate whether or not this method is capable of detecting a secondary peak that would represent complete grout backfill. Additionally, a greater energy impact would potentially enhance the results and allow for better assessment. The low P-wave velocity of the grout creates greater signal attenuation which could be a factor in preventing a secondary boundary reflection.

6.3 NDT Method Comparison

Both the GPR and IE methods demonstrated the ability to differentiate between grout and air at the segment extrados boundary. While no water was present in the tunnel at the time of testing, it is inferred that both methods have the ability to also differentiate between water and

grout based on results from the mock-liner experiment and the physics. Partial washout scenarios with grout at the immediate boundary of the segment has not been shown in this study to be detected with either method. The GPR method has been shown to not have the ability to penetrate more than 2.5 cm of grout even after sufficient set time. While seismic waves can penetrate the grout, it is unclear whether the Q-analysis can clearly detect a secondary peak at the grout-rock boundary.

A summary of the capabilities for GPR and IE on different annulus material cases is presented in Figure 6.14. The abilities of the methods are categorized by confirmed, likely, unlikely, plausible, and not plausible. Confirmed represents cases that have been directly demonstrated to work by either field testing or the mock-liner testing. Likely and unlikely were designated hypothetical likeliness of the method to work or not on situations in which the underlying physics is plausible but no firm evidence was collected. Plausible indicates the method has the potential to work, but no guess can be made on the statistical likeliness of the method to detect this case. Not-plausible indicates that based on the understanding of the physics and demonstrations by experiments, the method is certain to be ineffective.

Based on Figure 6.14 each method has both capabilities and limitations for different grouting scenarios. Advantages of the GPR are the larger scan areas that can be collected, that void lateral extent can delineated, and the certainty for complete washout detection without the likelihood of false-positives. The IE benefits are a quantitative assessment to differentiate full grout versus air or water and the potential ability to detect the rock boundary with more data. However, the IE also has disadvantages of detecting inconsequential microscopic structures that can create false-positives of voids and being a point measurement where void dimensionality cannot be delineated.

Due to the inability for GPR scans to accurately image through the lifting portal due to the ringing effect, as well as the inability to use the impact echo at the lifting portal location, ground truth physical evidence at the geophysical testing locations was not obtained. Furthermore, small water flows encountered during the drilled holes were not strong enough evidence to indicate the complete state of grout backfill to compare to the geophysical evidence.

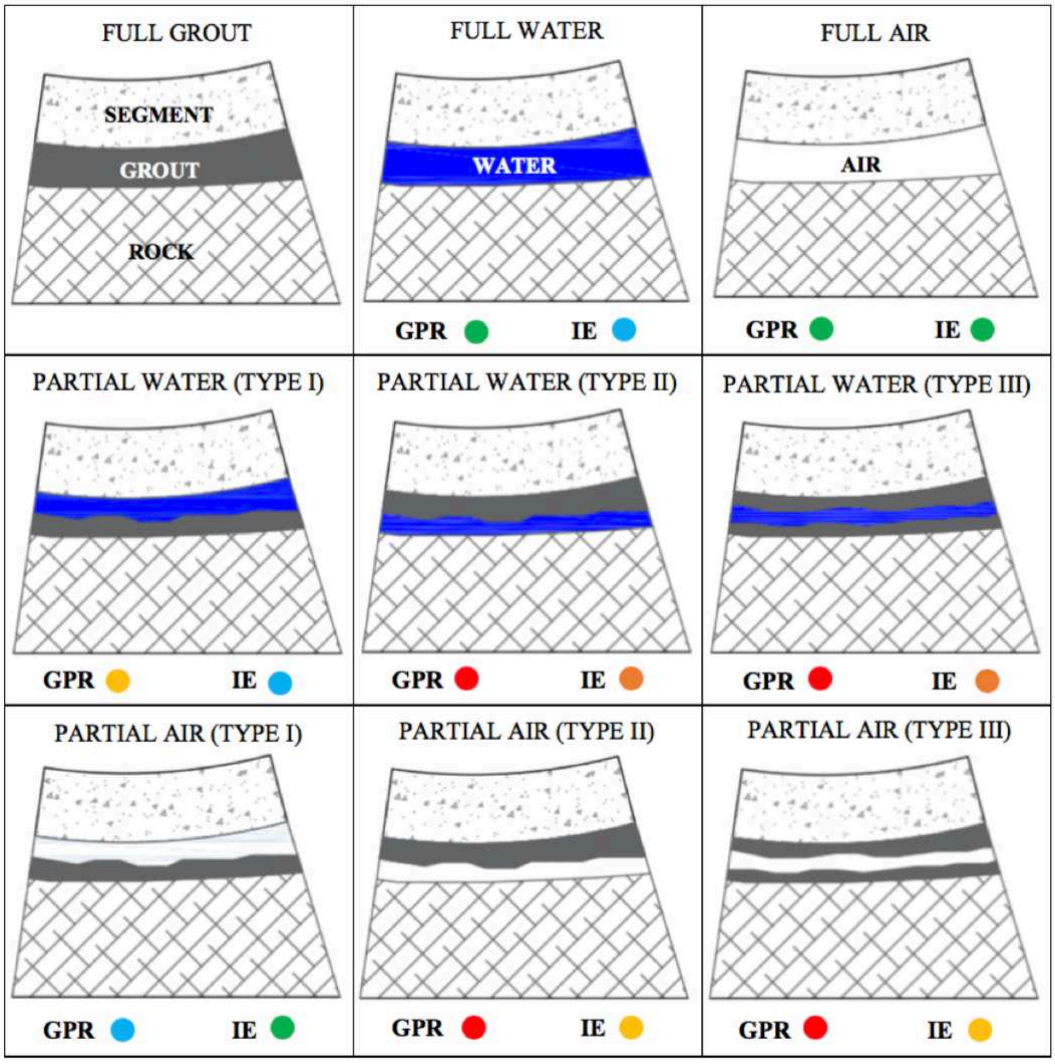

Figure 6.14 Summary of GPR and IE capabilities to differentiate different void-type scenarios compared to complete annulus grouting

CHAPTER 7
CONCLUSIONS AND RECOMMENDATIONS

This research project aimed at evaluating the capabilities of non-destructive testing methods to provide quality assurance on the annulus backfill grout for the Rondout Bypass tunnel. High water pressures expected along the tunnel alignment creates the potential for grout washout which is detrimental to the tunnel's long-term integrity. Current testing methods for the quality assurance of backfill grout are both destructive to the tunnel liner integrity, expensive, and time consuming. While this research was specifically calibrated to the Rondout Tunnel Project, the results and analysis can be applied to any future project with similar specifications.

GPR and IE were chosen for a comprehensive evaluation into their efficacy. Testing was completed to provide physical properties of the materials encountered within the tunnel and to establish anticipated baseline conditions for the NDT responses of each technique. Baseline conditions were established by a combination of mock-tunnel experiments composed of actual tunnel liner segments, numerical modeling, and the use of portions of the constructed tunnel with known conditions behind the liner. Both methods were then implemented in the field setting and compared to physical data to provide proof of the methods reliability.

Laboratory testing for electrical conductivity and dielectric permittivity was performed on the two-component grout to provide physical understanding for the GPR. Results established relatively high electrical conductivity of the two-component grout at both early and late set-times. The high electrical conductivity relative to other cementitious materials described in literature was attributed to the sodium silicate accelerant at early times in the gelling phase, and to the high water-to-cement ratio of component A after sufficient hydration of the cement. Results indicated high attenuation would be expected in the grout with no more than two inches of GPR signal penetration likely to be achieved. Dielectric permittivity testing was unable to provide accurate results due to trouble with the testing equipment available, but was deemed of secondary importance relative to the electrical conductivity. Both dielectric permittivity and electrical conductivity were determined through indirect methods by application of GPR directly on the segmental liner. Penetration tests demonstrated the highest frequency signal able to penetrate the segment to be 900 MHz. For this reason, a 900 MHz antenna was used for the remainder of the testing which provides the greatest resolution available.

P-wave velocity laboratory testing of the grout was conducted to establish the expected IE response on the annulus grout at different set times. This testing revealed a velocity and density that can be differentiated from a water or air void after several hours of curing. P-wave velocity testing on the segment was also conducted through indirect methods by using an IE device directly on a segment inside the tunnel with known air behind it. The segment P-wave velocity was found to be relatively high for concrete due to its high-strength properties and controlled curing conditions.

Baseline conditions established for the GPR response of voids beneath the segment were first determined by two mock-liner experiments. Two-component grout was injected into fabricated compartments beneath elevated segments with a central compartment left empty for water or air. The results from these experiments demonstrated clear ability of the GPR to differentiate complete air or water pockets within regions of grouted areas. Results were compared to numerical models which provided a secondary means of validating the GPR response and helped differentiate true reflections of the GPR off of material boundaries versus noise caused by ringing effects. Metal reflectors buried within the grout provided evidence that the GPR is unable to penetrate through one to two inches of grout regardless of the grout set time, which is supported by the laboratory testing of the grout's electrical conductivity. This leads to difficulties with the GPR in detecting voids buried beneath a layer of grout at the segment extrados and disables its ability to image the rock interface behind the annulus grout. A location with known air and grout in the tunnel allowed for validation of the observations from the mock-liner experiments in a field condition.

Baseline conditions established for the IE response of voids beneath the segment were determined from regions within the constructed tunnel with known segment backfill conditions. The starter tunnel contains ten rings supported by wooden blocks which were back-filled up to the spring line with concrete. This enabled IE to be tested on regions with known air and known concrete behind the segment. Results demonstrated ability of the IE Q-method to clearly differentiate areas of air versus concrete. Based on known velocity measurements from the laboratory testing of the grout, the Q measurements of regions with grout are anticipated to fall between air and concrete.

With baseline conditions for the NDT responses established, both GPR and IE measurements were performed within the tunnel at locations of assumed complete grout-backfill.

GPR detected mostly fully grouted scan lines with one scan line demonstrating a likely air void behind the segment. At the time of testing, there was not significant water flow behind the segment, and therefore no water voids were able to be clearly demonstrated with the GPR in a field setting. The IE also provided evidence of mostly fully-grouted annulus space, while also providing supporting evidence of an air void at the same location the GPR detected an air void. Destructive testing methods of the grout by drilling holes through the center lifting portal of the segments did not establish clear physical proof of the NDT methods due to non-overlap of the NDT/drilled hole locations as well as the minimal information provided by water-flow rates.

Based on the work completed, we have recommended GPR as a primary method for void detection in the tunnel, with IE and drilled holes as secondary means. The GPR has demonstrated ability to determine whether grout has been fully washed out of the annulus space or not. While small features buried within grout may not be detectable, these features can be considered inconsequential to the tunnel structural integrity. Furthermore, destructive methods would be similarly unlikely to detect these types of flaws. The ability to gather large data sets to correlate to known baseline conditions makes the GPR a valuable tool. Additional data collection with IE can provide a supplementary means to validate voids found by the GPR. These non-destructive methods can reduce costs and tunnel construction time in the future and ensure the structural integrity of our infrastructure.

7.1 Recommendations for Future Research

While this research provided a good basis for the use of NDT methods on void detection, further research in this area remains a necessity to advance the industry's application of NDT methods for annulus grout void detection. Some areas of further research include:

1. Numerical modelling to determine the relative effects of void sizes within the annulus grout on the forces and moments of the tunnel liner. As shown in this research, certain void sizes, such as very thin seams, or voids buried behind grout, may not be detected with some of the NDT methods. However, if these types of voids do not pose concern to the mechanical integrity of the tunnel, this may not undermine the effectiveness of the NDT methods from detecting voids of real-concern. Three-dimensional numerical models should be implemented to approach the full three-dimensional reality that voids pose in mechanical studies of a tunnel liner. Sensitivity

analyses can be performed by adjusting the void dimensions and analyzing the relative effect on the tunnel liner forces.

2. Laboratory testing on different two-component grout mixtures to design a mix with low values of effective conductivity. As the high electrical conductivity of the grout was determined to limit the applicability of GPR, new grout mixtures should be explored to manipulate the long-term electrical conductivity of the two-component grout. Use of a VNA method with embedded OE probes should be used to test the total effective conductivity of any new mixture. Additives to the grout mixtures may be identified to neutralize undesirable mobile ions in the grout solution. Additionally, means of lowering the water-to-cement ratio in the mixture may help long-term conductivity with the use of super-plasticizers to maintain the desired flowability of the component A.

3. IE testing to determine edge effects, hammer strength, and grout set time impact on the Q-values. Detailed testing of the IE device on different locations on the segments were not performed due to time constraints and the unavailability of locations in the tunnel at the time of testing. All IE testing should be performed on fully constructed tunnel rings to prevent ringing effects induced on floating concrete slabs. The edge effects describe how the position of the IE source and receiver relative to different segment edges effect the Q results. Hammer strength has been shown in previous literature to have an impact on the final results (Schoefs and Abraham, 2012). Hammer strength may be tested with a specialized machine that can provide uniform impact strength. Grout set time is known to affect the Q-values supported by the laboratory studies on the grout P-wave velocity during set time. However, field studies demonstrating the Q-value impact during grout set times were not performed in this research.

4. IE study on the effects of void structure size on Q analysis. Small mechanical discontinuities are known to impact the seismic response for rocks and concrete (Shirole et al., 2017). Detailed studies should therefore be performed to evaluate how the size of discontinuities impacts the IE response and ultimately the Q values. A deeper level of understanding is necessary to help differentiate between real voids and false-positive readings in the tunnel.

5. Additional physical data directly overlapping with both GPR and IE data points for the different void types. Physical data was not collected directly overlapping locations of NDT data due to the inability at the time of testing to puncture the segments in locations other than the center lifting portal. Since the GPR typically creates high ringing effects on top of the center lifting portal, and the IE cannot be used directly on top of the lifting portal, this created a location offset in physical versus NDT data. The preferred method for physical evidence to compare with NDT data would be cores through the segment. Providing physical evidence by use of cores in areas with the different voids outlined in Figure 6.14 would help with statistical analysis on the likelihood of the NDT methods in detecting those types of voids.

6. Performing similar evaluations as described here with other NDT methods, such as ultrasonic linear arrays or pulse-echo ultrasonic techniques. Ultrasonic linear arrays and pulse-echo ultrasonic techniques describe similar methods not explored in this work but may provide some of the benefits of both the IE and GPR. These arrays can be conducted with equipment similar to a GPR device in which elastic waves are transmitted and received along a scan line and then post processed into a 2-dimensional plot, similar to the GPR radargrams (Cassidy et al., 2011). These 2-D arrays provide the benefits of GPR, such as being able to detect the dimensionality of a void, while bypassing the EM wave attenuation caused by the high electrical conductivity of the grout. Furthermore, this method may have the ability to simultaneously provide Q values at different points along to the scan line, combining the two methods described in this work. The limitations of these methods include the high potential for background noise interference during tunnel construction, the necessity for near-perfect coupling of the transmitter and receiver with the segment, and the inability to propagate elastic waves through an air void if encountered.

REFERENCES

Aggelis DG, Shiotani T, Kasai K. 2008. Evaluation of grouting in tunnel lining using impact-echo. *Tunn Undergr Sp Technol* 23(6): 629–637. doi: 10.1016/j.tust.2007.12.001

Alani AM, Tosti F. 2018. GPR applications in structural detailing of a major tunnel using different frequency antenna systems. *Constr Build Mater* 158: 1111–1122. Elsevier Ltd. doi: 10.1016/j.conbuildmat.2017.09.100

Annan AP. 2005. Ground Penetrating Radar. In: *Near-Surface Geophysics*. Society of Exploration Geophysicists. p. 357–438.

Azadi MR, Taghichian A, Taheri A. 2017. Optimization of cement-based grouts using chemical additives. *J Rock Mech Geotech Eng* 9(4): 623–637. Elsevier Ltd.

Bernat S, Cambou B. 1998. Soil-structure interaction in shield tunnelling in soft soil. *Comput Geotech* 22(3–4): 221–242.

Bessaies-Bey H, Baumann R, Schmitz M, Radler M, Roussel N. 2015. Effect of polyacrylamide on rheology of fresh cement pastes. *Cem Concr Res* 76: 98–106. Elsevier Ltd. doi: 10.1016/j.cemconres.2015.05.012

Bezuijen a., Zon WH Van Der, Talmon a. M. 2005. Laboratory testing of grout properties and their influence on backfill grouting. *Tunnelling A Decad Progress GeoDelft 1995-2005*: 115–121. doi: doi:10.1201/9781439834268.ch17

Blackham DV, Pollard RD. 1997. An improved technique for permittivity measurements using a coaxial probe. *IEEE Trans Instrum Meas* 46(5): 1093–1099. doi: 10.1109/19.676718

de Blasio B, Sapienza V. 2016. New York City 2009 Drinking Water Supply and Quality Report Catskill / Delaware Watersheds. NYC Environmental Protection.

Bourbie T, Coussy O, Zinszner B. 1987. *Acoustics of Porous Media*. Institut Francais su Petrole Publications.

Brantberger M, Stille H, Eriksson M. 2000. Controlling grout spreading in tunnel grouting-analyses and developments of the GIN-method. *Tunn Undergr Sp Technol* 15(4): 343–352. doi: 10.1016/S0886-7798(01)00003-7

Cai J, Wei W, Hu X, Wood DA. 2017. Electrical conductivity models in saturated porous media: A review. *Earth-Science Rev* 171(March): 419–433. Elsevier. doi: 10.1016/j.earscirev.2017.06.013

Cassidy NJ, Eddies R, Dods S. 2011. Void detection beneath reinforced concrete sections: The practical application of ground-penetrating radar and ultrasonic techniques. *J Appl Geophys* 74(4): 263–276. doi: 10.1016/j.jappgeo.2011.06.003

Chen DH, Scullion T. 2008. Detecting subsurface voids using Ground-coupled Penetrating Radar. *Geotech Test J* 31(3): 217–224.

Chen Z, Schwing M, Karlovšek J, Wagner N, Scheuermann A. 2014. Broadband Dielectric Measurement Methods for Soft Geomaterials: Coaxial Transmission Line Cell and Open-Ended Coaxial Probe. *Int J Eng Technol* 6(5): 373–380. doi: 10.7763/IJET.2014.V6.728

Cui W, Huang J, Song H, Xiao M. 2017. Development of two new anti-washout grouting materials using multi-way ANOVA in conjunction with grey relational analysis. *Constr Build Mater* 156: 184–198. Elsevier Ltd. doi: 10.1016/j.conbuildmat.2017.08.126

Daniels DJ. 2004. Ground Penetrating Radar (2nd Edition). *Gr Penetrating Radar (2nd Ed*, in press.

Everett ME. 2013. *Near-Surface Applied Geophysics*. Combridge University Press.

Flores AQ. 2015. Physical and mechanical behavior of a two component cement-based grout for mechanized tunneling application. instituto alberto luiz coimbra de pós graduação.

Fowler M, Palermo R, Pintabona R, Smithson Jr M. 2012. No Title. North American Tunneling: 869. Englewood, CO: Society for Mining Metallurgy and Exploration, Inc.

Geophysical Survey Systems Inc. 2017. Concrete Handbook.

Gheibi A, Hedayat A. 2018. Ultrasonic investigation of granular materials subjected to compression and crushing. *Ultrasonics* 87: 112–125. Elsevier B.V. doi: 10.1016/j.ultras.2018.02.006

Gucunski N, Imani A, Romero F, Nazarian S, Yuan D, Wiggenhauser H, Shokouhi P, Taffe A, Kutrubes D. 2013. Nondestructive Testing to Identify Concrete Bridge Deck Deterioration. doi: 10.17226/22771

Guéguen Y, Palciauskas V. 1994. No Title. In: *Introduction to the Physcis of Rocks*. Princeton University Press.

Han B, Guan X, Ou J. 2007. Electrode design, measuring method and data acquisition system of carbon fiber cement paste piezoresistive sensors. *Sensors Actuators, A Phys* 135(2): 360–369. Elsevier B.V. doi: 10.1016/j.sna.2006.08.003

Harbec D, Tagnit-Hamou A, Gitzhofer F. 2016. Waste-glass fume synthesized using plasma spheroidization technology: Reactivity in cement pastes and mortars. *Constr Build Mater* 107: 272–286. Elsevier Ltd. doi: 10.1016/j.conbuildmat.2016.01.011

Hashimoto T, Konda T, Brinkman J, Feddema A, Kano Y. 2004. Simultaneous Backfill Grouting, Pressure Development in Construction Phase and in the Long Term. 30th Ita-Aites World Tunnel Congress Singapore: 22–27.

Hashin Zv, Shtrikman S. 1962. A Variational Approach to the Theory of the Effective Magnetic

Permeability of Multiphase Materials. *J Appl Phys* 33.10: 3125–3131.

Hedayat A, Bobet A, Pyrak-Nolte LJ. 2012. Monitoring slip initiation and propagation along frictional interfaces with seismic wave transmission. 46th US Rock Mechanics Symposium. Chicago.

Hedayat A, Pyrak-Nolte L, Bobet A. 2013. Multi-modal monitoring of slip along frictional discontinuities. 47th US Rock Mechanics Symposium. San Francisco.

Hedayat A, Pyrak-Nolte LJ, Bobet A. 2014a. Precursors to the shear failure of rock discontinuities. *Geophys Res Lett* 41: 5467–5475. doi: 10.1002/2014GL060285

Hedayat A, Pyrak-Nolte LJ, Bobet A. 2014b. Detection and quantification of slip along non-uniform frictional discontinuities using digital image correlation. *Geotech Test J* 37(5). doi: 10.1520/GTJ20130141

Hedayat A, Pyrak-Nolte LJ, Bobet A. 2014c. Multi-modal monitoring of slip along frictional discontinuities. *Rock Mech Rock Eng* 47(5): 1575–1587. doi: 10.1007/s00603-014-0588-7

Hedayat A, Pyrak-Nolte LJ, Bobet A. 2014. Geophysical Investigation of Shear Failure along Cohesive-Frictional Rock Discontinuities. *Arma 14*, in press.

Hedayat A, Walton G. 2017. Laboratory determination of rock fracture shear stiffness using seismic wave propagation and digital image correlation. *Geotech Test J* 40(1): 92–106. doi: 10.1520/GTJ20160035

Hee IA. 2012. Use of Ground Penetrating Radar to Verify Segmental Lining Backfill Grouting. Politecnico di Torino.

Henzinger MR, Radončić N, Moritz BA, Schubert W. 2016. Backfill of segmental lining – State of the art, redistribution behaviour of pea gravel, possible improvements / Tübbingbettung – Stand der Technik, Umlagerungsverhalten von Perlkies, Verbesserungspotenzial. *Geomech und Tunnelbau* 9(3): 188–199. doi: 10.1002/geot.201600013

Instruments L& R. 2010. MiniRes Manual.

Josh M, Clennell B. 2015. Broadband electrical properties of clays and shales: Comparative investigations of remolded and preserved samples. *Geophysics* 80(2): D129–D143. doi: 10.1190/geo2013-0458.1

Kaatze U. 2010. Techniques for measuring the microwave dielectric properties of materials. *Metrologia* 47(2). doi: 10.1088/0026-1394/47/2/S10

Kang JM, Song S, Park D, Choi C. 2017. Detection of cavities around concrete sewage pipelines using impact-echo method. *Tunn Undergr Sp Technol* 65: 1–11. Elsevier Ltd. doi: 10.1016/j.tust.2017.02.002

Karlovšek J, Schuermann A, Willimas DJ. 2012. Investigation of voids and cavities in Bored

Tunnels using GPR. *Proc 14th Int Conf Gr Penetrating Radar*: 496–501. doi: 10.1109/ICGPR.2012.6254916

Karlovšek J, Schwing M, Chen Z, Wagner N, Williams DJ, Scheuermann A. 2016. Dielectric measurement method for real-time monitoring of initial hardening of backfill materials used for underground construction. *J Geophys Eng* 13(2): S19–S27. doi: 10.1088/1742-2132/13/2/S19

Khayat KH. 1998. Viscosity-enhancing admixtures for cement-based materials — An overview. *Cem Concr Compos* 20(2–3): 171–188. doi: 10.1016/S0958-9465(98)80006-1

Knight RJ, Endres AL. 2005. An Introduction to Rock Physics Principles for Near-Surface Geophysics. In: *Near-Surface Geophysics*. p. 31–70.

Lalagüe A, Lebens MA, Hoff I, Grøv E. 2016. Detection of Rockfall on a Tunnel Concrete Lining with Ground-Penetrating Radar (GPR). *Rock Mech Rock Eng* 49(7): 2811–2823. doi: 10.1007/s00603-016-0943-y

Layssi H, Ghods P, Alizadeh AR, Salehi M. 2015. Electrical Resistivity of Concrete: Concepts, applications, and measurement techniques. *Concr Int*(May): 1–36.

Levita G, Marchetti A, Gallone G, Princigallo A, Guerrini GL. 2000. Electrical properties of fluidified Portland cement mixes in the early stage of hydration. *Cem Concr Res* 30(6): 923–930. doi: 10.1016/S0008-8846(00)00282-9

Li Z, Xiao L, Wei X. 2007. Determination of Concrete Setting Time Using Electrical Resistivity Measurement. *J Mater Civ Eng* 19(5): 423–427. doi: 10.1061/(ASCE)0899-1561(2007)19:5(423)

Madhavi TC, Annamalai S. 2016. Electrical conductivity of concrete. *ARPN J Eng Appl Sci* 11(9): 5979–5982.

New York City Department of Environmental Protection. 2017. Water for the Future Program: Upstate Water Supply Resisliency. New York City.

Nobes DC. 2016. Ground Penetrating Radar Response from Voids: A Demonstration Using a Simple Model. 16th International Conference of Ground Penetrating Radar (GPR).

Oldenburg D, Jones F, Heagy L, Cockett R, Astic T, Devriese S. 2017. Ground Penetrating Radar: Basic Principles.

Olhoeft GR. 1998. Electrical, Magnetic, and Geometric Properties that Determine Ground Penetrating Radar Performance. *Seventh Int'l Conf Gr Penetrating Radar*(September): 177–182.

Parkinson G, Ékes C. 2008. Ground penetrating radar evaluation of concrete tunnel linings. *12th Int Conf Gr Penetrating Radar*(June): 11. Available at http://sewervue.com/wp-content/uploads/Parkinson_Ekes_Kapoor_Tunnel-GPR2008-compressed.pdf.

Peila D, Borio L, Pelizza S. 2011. The behaviour of a two-component backfilling grout used in a tunnel-boring machine. *Acta Geotech Slov* 8(1): 5–15.

Pelizza S, Peila D, Borio L, Dal Negro E, Schulkins R, Boscaro A. 2010. Analysis of the performance of two component back-filling grout in tunnel boring machines operating under face pressure. ITA-AITES World Tunnel Congress.

Pellegrini L, Perruzza P. 2009. Sao Paulo Metro project - Control of settlements in variable soil conditions through EPB pressure and bicomponent backfill grout. *Proc - Rapid Excav Tunneling Conf* 2(Line 2): 1137–1153.

Powers MH. 1997. Modeling frequency-dependent GPR. *Lead Edge* 16(11): 1657–1662.

Rajabipour F, Weiss J. 2007. Electrical conductivity of drying cement paste. *Mater Struct Constr* 40(10): 1143–1160. doi: 10.1617/s11527-006-9211-z

Razak NA, Senin SF, Hamid R. 2015. Detection of sizes and locations air voids in reinforced concrete slab using ground penetrating radar and Impact-Echo methods. *J Teknol* 74(3): 63–67.

Revil A, Coperey A, Shao Z, Florsch N, Fabricius IL, Deng Y, Delsman JR, Pauw PS, Karaoulis M, de Louw PGB, et al. 2017. Complex conductivity of soils. *Water Resour Res*: 1–18. doi: 10.1002/2016WR019804.Received

De Rosa J, Pontolillo DM, Di Maio C, Vassallo R. 2016. Chemical Clay Soil Improvement: From Laboratory to Field Test. *Procedia Eng* 158: 284–289. doi: 10.1016/j.proeng.2016.08.443

Ryden N, Aurell O, Nilsson P, Hartlen J. 2013. Impact Echo Q-Factor Measurements Towards Non-Destructive Quality Control of the Backfill in Segmental Lined Tunnels. In: *Nondestructive Testing of Materials and Structures*. Springer. p. 915–919.

Schoefs F, Abraham O. 2012. Probabilistic evaluation to improve design of impact-echo sources. *Transp Res Rec*(2313). doi: 10.3141/2313-12

Sharghi M, Chakeri H, Ozcelik Y. 2017. Investigation into the effects of two component grout properties on surface settlements. *Tunn Undergr Sp Technol* 63: 205–216. Elsevier Ltd. doi: 10.1016/j.tust.2017.01.004

Sharma S, Kothiyal NC. 2016. Comparative effects of pristine and ball-milled graphene oxide on physico-chemical characteristics of cement mortar nanocomposites. *Constr Build Mater* 115: 256–268. Elsevier Ltd. doi: 10.1016/j.conbuildmat.2016.04.019

Sheriff RE. 2002. Encyclopedic Dictionary of Exploration Geophysics, 4th Edition. Society of Exploration Geophysicists.

Shirlaw JN, Richards DP, Ramond P, Longchamp P. 2004. Recent experience in automatic tail void grouting with soft ground tunnel boring machines. *Tunn Undergr Sp Technol* 19(4–5):

446. doi: 10.1016/j.tust.2004.02.056

Shirole D, Hedayat A, Walton G. 2017. Active Ultrasonic Monitoring of Rocks Under Uniaxial Compression. (June). Available at https://www.onepetro.org/conference-paper/ARMA-2017-0820?sort=&start=0&q=Shirole+ARMA&from_year=&peer_reviewed=&published_between=&fromSearchResults=true&to_year=&rows=10#.

Shirole D, Walton G, Ostrovsky LA, Masoumi H, Hedayat A. 2018. A Non-Linear Ultrasonic Method for Damage Characterization in a Shaly Sandstone. 52nd US Rock Mechanics / Geomechanics Symposium. Seattle.

Soutsos MN, Bungey JH, Millard SG, Shaw MR, Patterson A. 2001. Dielectric properties of concrete and their influence on radar testing. *NDT E Int* 34(6): 419–425. doi: 10.1016/S0963-8695(01)00009-3

Susanto A, Koleva DA, Copuroglu O, van Beek K, van Breugel K. 2013. Mechanical, Electrical and Microstructural Properties of Cement-Based Materials in Conditions of Stray Current Flow. *J Adv Concr Technol* 11(3): 119–134. doi: 10.3151/jact.11.119

Takahashi K, Igel J, Preetz H, Kuro S. 2012. Basics and Application of Ground-Penetrating Radar as a Tool for Monitoring Irrigation Process. *Probl Perspect Challenges Agric Water Manag*, in press. doi: 10.5772/29324

Tang SW, Cai XH, He Z, Zhou W, Shao HY, Li ZJ, Wu T, Chen E. 2017. The review of early hydration of cement-based materials by electrical methods. *Constr Build Mater* 146: 15–29. doi: 10.1016/j.conbuildmat.2017.04.073

Tereshchenko O V., Buesink FJK, Leferink FBJ. 2011. An overview of the techniques for measuring the dielectric properties of materials. *Ieee*: 1–4. doi: 10.1109/URSIGASS.2011.6050287

Topcu IB, Uygunolu T, Hocaolu I. 2012. Electrical conductivity of setting cement paste with different mineral admixtures. *Constr Build Mater* 28(1): 414–420. doi: 10.1016/j.conbuildmat.2011.08.068

Tumidajski PJ. 1996. Electrical conductivity of Portland cement mortars. *Cem Concr Res* 26(4): 529–534. doi: 10.1016/0008-8846(96)00027-0

Venkatesh MS, Raghavan GSV. 2005. An Overview of Dielectric Properties Measuring Techniques An overview of dielectric properties measuring techniques. *Can Biosyst Eng* 47(January 2005): 7.16-7.30. doi: 10.1109/URSIGASS.2011.6050287

Waff HS. 1974. Waff, Harve S. "Theoretical considerations of electrical conductivity in a partially molten mantle and implications for geothermometry. *J Geophys Res* 79.26: 4003–4010.

Wagner N, Schwing M, Scheuermann A. 2014. Numerical 3-D FEM and experimental analysis

of the open-ended coaxial line technique for microwave dielectric spectroscopy on soil. *IEEE Trans Geosci Remote Sens* 52(2): 880–893. doi: 10.1109/TGRS.2013.2245138

Warren C, Giannopoulos A, Giannakis I. 2016. gprMax: Open source software to simulate electromagnetic wave propagation for Ground Penetrating Radar. *Comput Phys Commun* 209: 163–170. Elsevier B.V. doi: 10.1016/j.cpc.2016.08.020

Weiss J, Snyder K, Bullard J, Bentz D. 2013. Using a Saturation Function to Interpret the Electrical Properties of Partially Saturated Concrete. *J Mater Civ Eng* 25(8): 1097–1106. doi: 10.1061/(ASCE)MT.1943-5533.0000549

Wu M, Yao X, Zhang L. 2000. Improved coaxial probe technique for measuring microwave permittivity of thin dielectric materials. *Meas Sci Technol* 11(11): 1617–1622. doi: 10.1088/0957-0233/11/11/311

Xiao L, Li Z. 2008. Early-age hydration of fresh concrete monitored by non-contact electrical resistivity measurement. *Cem Concr Res* 38(3): 312–319. doi: 10.1016/j.cemconres.2007.09.027

Xie X, Liu Y, Huang H, Du J, Zhang F, Liu L. 2007. Evaluation of grout behind the lining of shield tunnels using ground-penetrating radar in the Shanghai Metro Line, China. *J Geophys Eng* 4(3): 253–261. doi: 10.1088/1742-2132/4/3/S03

Yang K-H, Song J-K. 2009. Workability Loss and Compressive Strength Development of Cementless Mortars Activated by Combination of Sodium Silicate and Sodium Hydroxide. *J Mater Civ Eng* 21(3): 119–127. doi: 10.1061/(ASCE)0899-1561(2009)21:3(119)

Yousuf F, Wei X, Tao J. 2017. Evaluation of the influence of a superplasticizer on the hydration of varying composition cements by the electrical resistivity measurement method. *Constr Build Mater* 144: 25–34. doi: 10.1016/j.conbuildmat.2017.03.138

Yu QM, Zhou HL, Wang YH, Duan RX. 2016. Quality monitoring of metro grouting behind segment using ground penetrating radar. *Constr Build Mater* 110: 189–200. Elsevier Ltd. doi: 10.1016/j.conbuildmat.2015.12.109

Zhang F, Xie X, Huang H. 2010. Application of ground penetrating radar in grouting evaluation for shield tunnel construction. *Tunn Undergr Sp Technol* 25(2): 99–107. Elsevier Ltd. doi: 10.1016/j.tust.2009.09.006

APPENDIX A

SEGMENT REBAR LAYOUT

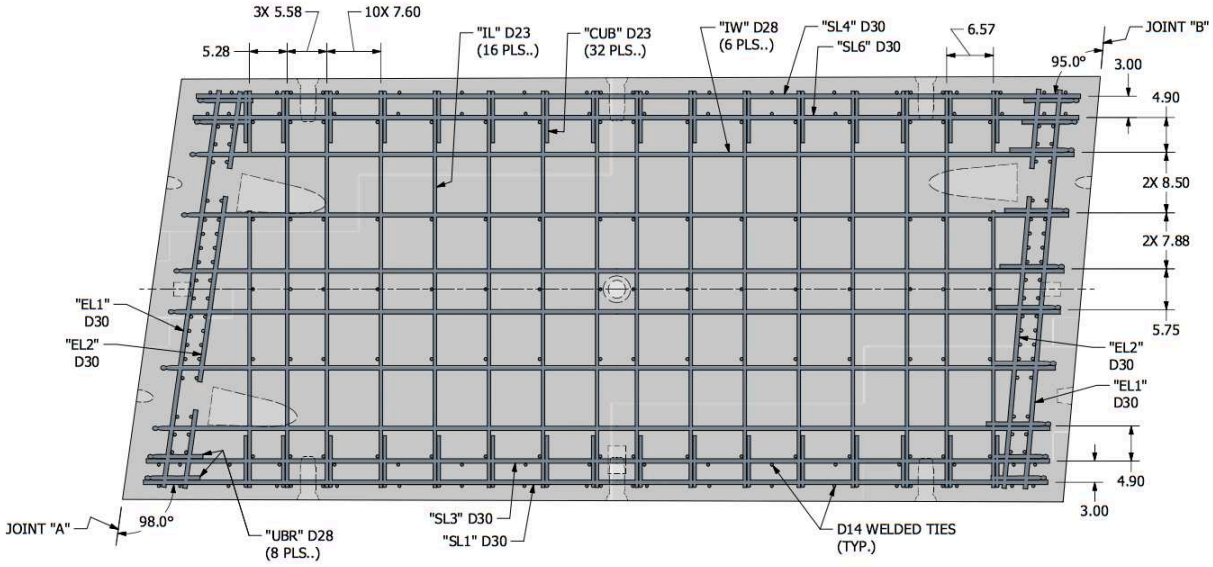

Figure A.1 Rondout segment steel reinforcement layout plan view

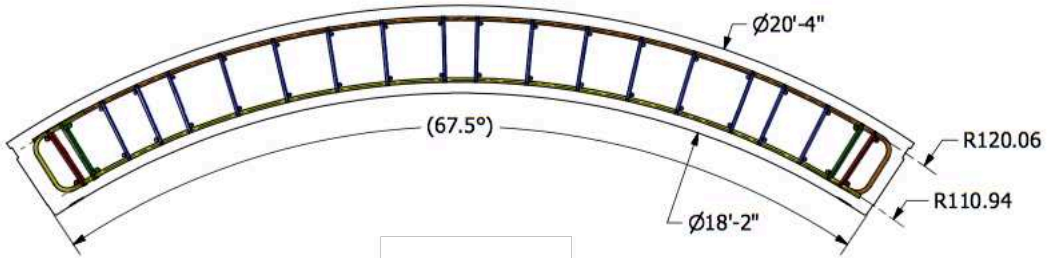

Figure A.2 Rondout segment steel reinforcement cross section

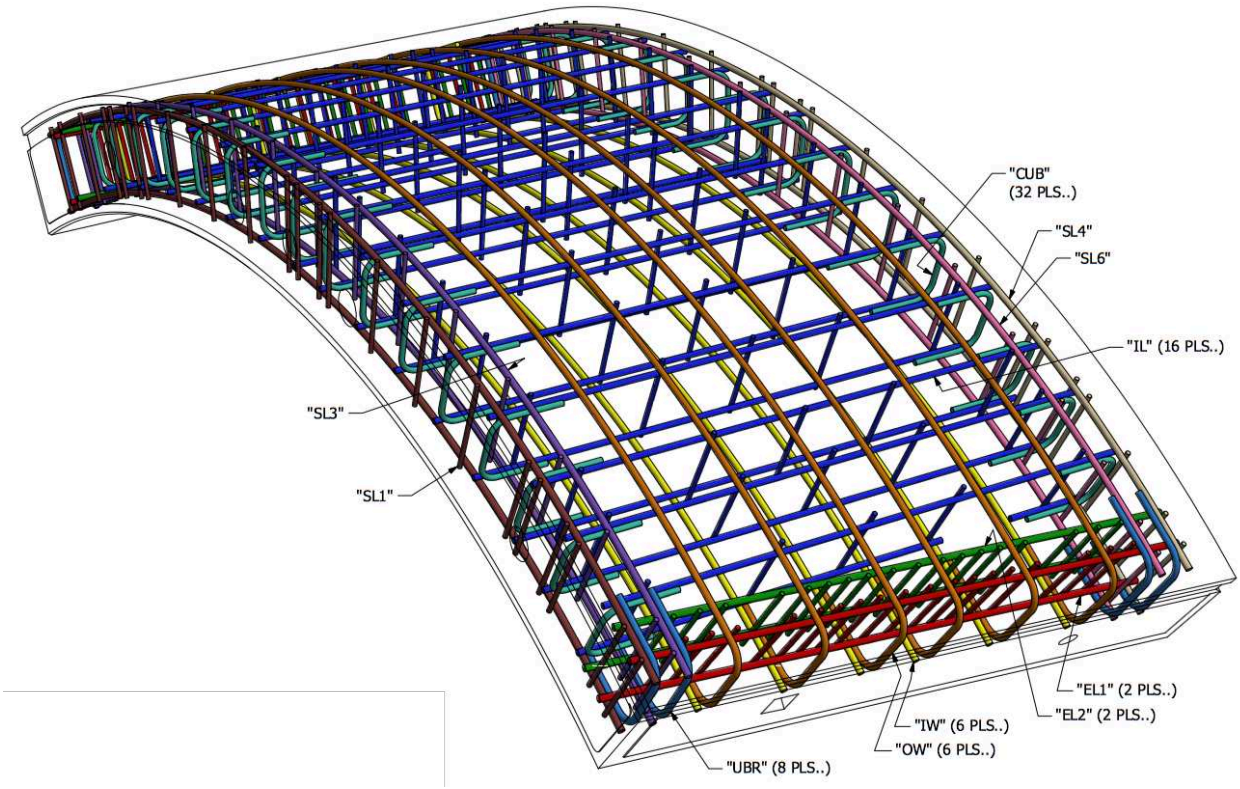

Figure A.3 Rondout project segment steel reinforcement isometric view

APPENDIX B

LABORATORY TEST RESULTS

Electrical conductivity test results displayed in Figure B.1 are from four tests conducted on tubes with various dimensions, shown in Table B.1. Three aspects of the tube were varied to ensure the tube aspect ratio did not affect the observed conductivity on the same material after calibrating the tubes. Two-component grout with 10% sodium silicate accelerant were used in each of the tubes. The results demonstrated a maximum of 7% deviation at early set times when the conductivity is rapidly changing, and less than 1% deviation after two hours. The higher deviation at early set time can be attributed to the independently mixed tubes which could contain a small error in accelerant percentage, as well as manually collecting the data points at given time intervals.

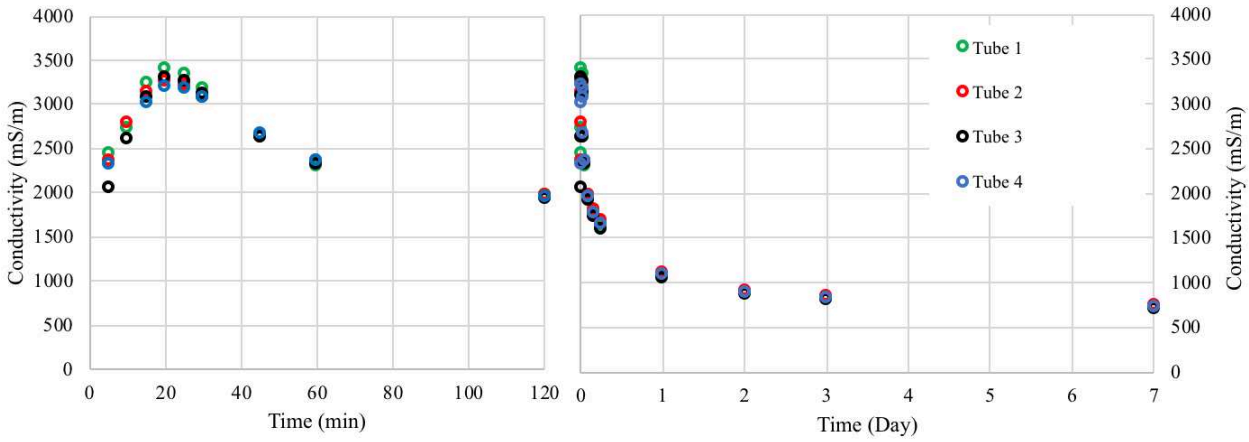

Figure B.1 Electrical conductivity test results testing different tube dimensions, all with 10% accelerant

Table B.1 Tube dimensions for electrical conductivity test

Tube ID	Tube Length (cm)	V Electrode Spacing (cm)	Tube Diameter (cm)
Tube 1	30.48	20.32	3.81
Tube 2	30.48	20.32	5.08
Tube 3	30.48	10.16	5.08
Tube 4	40.64	20.32	5.08

Dielectric permittivity test results conducted on hardening grout specimens formed in cubes are shown in Figure B.2a. The corresponding effective conductivity of the same samples are shown in Figure B.2b, which were converted from the measured imaginary part of the total permittivity. A picture of the cubic grout specimen placed up against the OC probe is shown in Figure B.3.

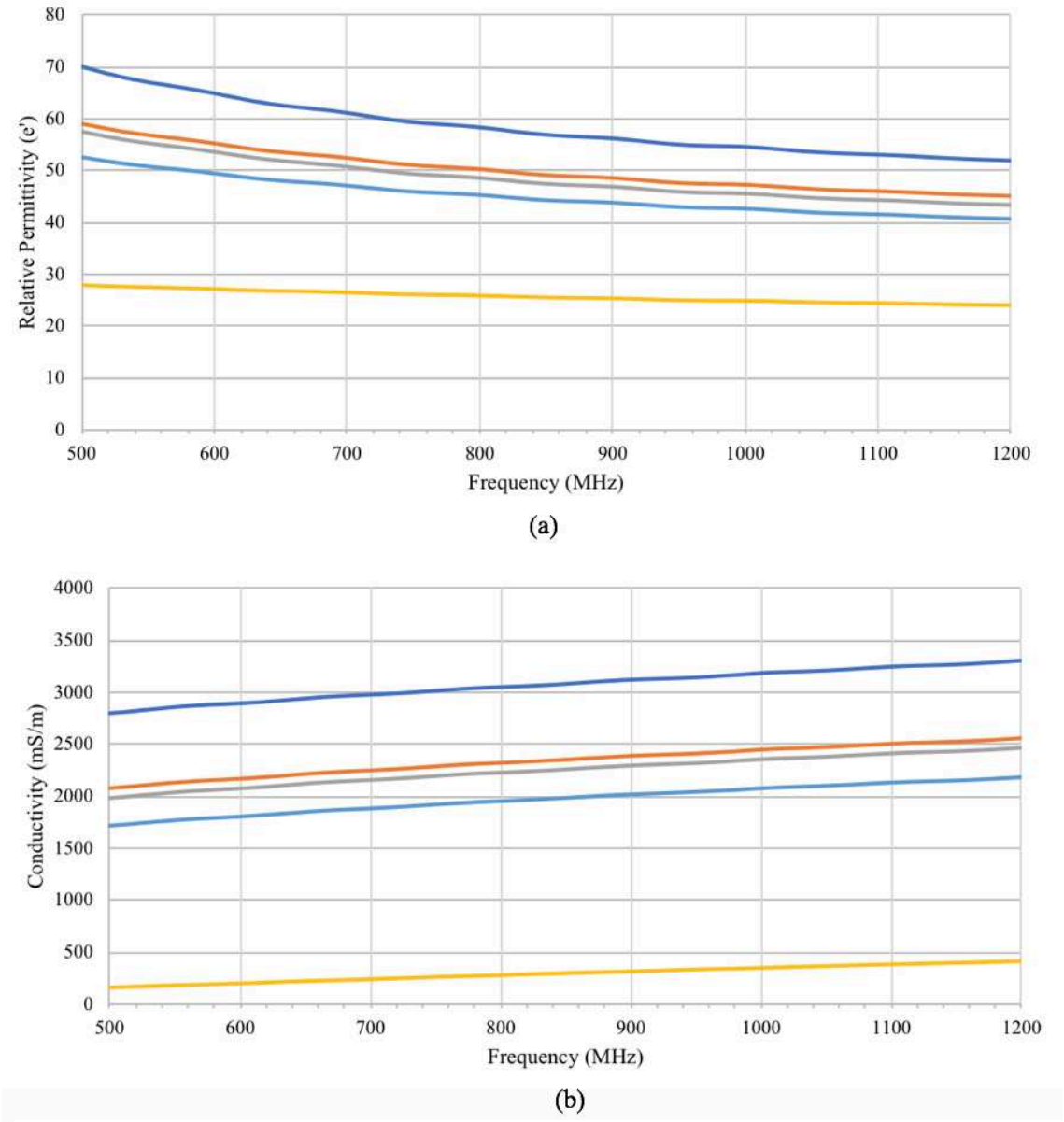

Figure B.2 Dielectric permittivity results measured on accelerated cubic grout specimens with a VNA. Each line represents a single measurement taken on the same grout specimen, revealing the unrepeatability of the tests (a) real part of the permittivity (b) imaginary part of the permittivity converted to effective conductivity

Multiple measurements conducted on the same cubic specimen, at the same time and location are shown in Figure B.2a and b to convey the non-repeatability of the results. Relative permittivity was demonstrated to have a range between 25 to 58 at the 900MHz frequency. This variability is not representative of the true nature of the material and is likely due to an inherent contact issue between the probe and the specimen surface. Any slight gap between the probe and specimen surface would create a falsely low reading, since air has a permittivity of 1 (Wu, Yao, and Zhang 2000). Attempts at increasing the application pressure of the probe onto the surface were attempted but this did not alleviate the variability issue. The highest recorded permittivity values recorded are believed to be the closest measurements to the real permittivity of the material, but these values cannot be confidently validated.

Permittivity and conductivity values at the high end of the measurements align with results recorded by Karlovšek et al. 2016 in their VNA studies on a similar grout material. Effective conductivity measured at 500 MHz was found to be slightly above the recorded conductivity from the DC studies. This aligns with theory that the DC conductivity is the effective conductivity at zero frequency, and therefore frequency effects would add to the total observed effective conductivity recorded with the VNA.

Figure B.3 Cubic grout specimen placed in contact with the OC probe by use of a laboratory lift and foam block to maintain firm pressure

APPENDIX C
SUPPLEMENTAL ELECTRONIC FILE

Included as a supplemental electronic file is the GPR user guide created for Kiewit to operate the purchased GSSI-GPR equipment. This manual was intended to provide Kiewit field engineers instruction on equipment storage, equipment setup, performing a scan, analyzing data, transferring data, and trouble shooting. Settings used on the GPR and calibrated void detection results are also provided in this manual.

Kiewit_GPRUserGuide.pdf	User guide created for Kiewit to operate the purchased GSSI-GPR equipment